

UPCommons

Portal del coneixement obert de la UPC

<http://upcommons.upc.edu/e-prints>

© 2018. Aquesta versió està disponible sota la llicència CC-BY-NC-ND 4.0 <http://creativecommons.org/licenses/by-nc-nd/4.0/>

© 2018. This version is made available under the CC-BY-NC-ND 4.0 license <http://creativecommons.org/licenses/by-nc-nd/4.0/>

Manuscript Number: GEOMOR-6524R3

Title: Near surface geophysical analysis of the Navamuño depression (Sierra de Béjar, Iberian Central System): Geometry, sedimentary infill and genetic implications of tectonic and glacial footprint

Article Type: Research Paper

Keywords: Near Surface Geophysics, intermountain basin, Late Glacial Period, Iberian Central System

Corresponding Author: Dr. Rosa M. Carrasco, Ph.D

Corresponding Author's Institution: Castilla-La Mancha University

First Author: Rosa M. Carrasco, Ph.D

Order of Authors: Rosa M. Carrasco, Ph.D; Valenti Turu; Javier Pedraza, Ph.D.; Alfonso Muñoz-Martín, Ph.D.; Xavier Ros; Jesús Sánchez, Ph.D.; Blanca Ruiz-Zapata, Ph.D.; Antonio J Olaiz; Ramón Herrero-Simón, Ph.D.

Abstract: The geometric and genetic characterization of the Navamuño depression peatland system (Iberian Central System) is presented here using results from a geophysical survey. This depression is a ~30 ha pseudo-endorheic flat basin over granitic bedrock. Three geophysical techniques were used to map the subsurface geology, and identify and describe the infill sequence: shallow seismic refraction (SR), magnetic resonance sounding (MRS) and electrical resistivity measurements (VES and ERT).

The three main geoelectrical layers (G1, G2, G3) identified in previous research, have also been identified in the present work. Using the data obtained in this new research we have been able to analyse these three geological layers in detail and reinterpret them. They can be grouped genetically into two sedimentary units: an ancient sedimentary body (G3), of unknown age and type, beneath an Upper Pleistocene (G2) and Holocene (G1) sedimentary infill. The facies distribution and geometry of the Upper Pleistocene was examined using the Sequence Stratigraphy method, revealing that the Navamuño depression was an ice-dammed in the last glacial cycle, resulting a glaciolacustrine sedimentation. A highly permeable sedimentary layer or regolith exists beneath the glaciolacustrine deposits. Below 40 m depth, water content falls dramatically down to a depth of 80 m where unweathered bedrock may be present.

The information obtained from geophysical, geological and geomorphological studies carried out in this research, enabled us to consider various hypotheses as to the origin of this depression. According to these data, the Navamuño depression may be explained as the result of a transtensional process from the Puerto de Navamuño strike-slip fault during the reactivation of the Iberian Central System (Paleogene-Lower Miocene, Alpine orogeny), and can be correlated with the pull-apart type basins described in these areas. The neotectonic activity of this fault and the ice-dammed processes in these areas during the Last

Glacial Cycle (MIS2) were the main causes of recent sedimentary infill in this depression.

The responses to Editorial comments of edited/revisee manuscript GEOMOR-6524-R2 have been included in the Cover Letter.

Highlights

- The surficial and subsurficial geology of Navamuño depression was established
- Using geophysical methods, the infill deposits have been interpreted
- The genetic implications of subsidence and ice-dammed processes have been analysed

Abstract

1
2 The geometric and genetic characterization of the Navamuño depression peatland system
3 (Iberian Central System) is presented here using results from a geophysical survey. This depression
4 is a ~30 ha pseudo-endorheic flat basin over granitic bedrock. Three geophysical techniques were
5 used to map the subsurface geology, and identify and describe the infill sequence: shallow seismic
6 refraction (SR), magnetic resonance sounding (MRS) and electrical resistivity measurements (VES
7 and ERT).
8

9
10 The three main geoelectrical layers (G1, G2, G3) identified in previous research, have also
11 been identified in the present work. Using the data obtained in this new research we have been able
12 to analyse these three geological layers in detail and reinterpret them. They can be grouped
13 genetically into two sedimentary units: an ancient sedimentary body (G3), of unknown age and type,
14 beneath an Upper Pleistocene (G2) and Holocene (G1) sedimentary infill. The facies distribution
15 and geometry of the Upper Pleistocene was examined using the Sequence Stratigraphy method,
16 revealing that the Navamuño depression was an ice-dammed in the last glacial cycle, resulting a
17 glaciolacustrine sedimentation.
18

19
20 A highly permeable sedimentary layer or regolith exists beneath the glaciolacustrine
21 deposits. Below 40 m depth, water content falls dramatically down to a depth of 80 m where
22 unweathered bedrock may be present.
23

24
25 The information obtained from geophysical, geological and geomorphological studies carried
26 out in this research, enabled us to consider various hypotheses as to the origin of this depression.
27 According to these data, the Navamuño depression may be explained as the result of a
28 transtensional process from the Puerto de Navamuño strike-slip fault during the reactivation of the
29 Iberian Central System (Paleogene-Lower Miocene, Alpine orogeny), and can be correlated with the
30 pull-apart type basins described in these areas. The neotectonic activity of this fault and the ice-
31 dammed processes in these areas during the Last Glacial Cycle (MIS2) were the main causes of
32 recent sedimentary infill in this depression.
33
34
35
36
37
38
39
40
41
42
43
44
45
46
47
48
49
50
51
52
53
54
55
56
57
58
59
60
61
62
63
64
65

1 **Near surface geophysical analysis of the Navamuño depression (Sierra de**
2 **Béjar, Iberian Central System): Geometry, sedimentary infill and genetic**
3 **implications of tectonic and glacial footprint**

4

5 Rosa M. Carrasco^a, Valentí Turu^b, Javier Pedraza^c, Alfonso Muñoz-Martín^{c,g}, Xavier
6 Ros^b, Jesús Sánchez^a, Blanca Ruiz-Zapata^d, Antonio J. Olaiz^e, Ramón Herrero-Simón^f,
7

8 ^a Dpt. of Geological and Mining Engineering, Univ. of Castilla-La Mancha, Avda. Carlos
9 III, s/n, 45071 Toledo, Spain.

10 ^b Fundacio Marcel Chevallier, Edifici Socio-Cultural de La LLacuna, AD500 Andorra la
11 Vella, Principality of Andorra.

12 ^c Dpt. of Geodynamic, Complutense University, C/ José Antonio Novais, 12, 28040
13 Madrid, Spain.

14 ^d Dpt. of Geology, Alcalá University, Ctra. A-II km 33,600, 28871 Alcalá de Henares,
15 Madrid.

16 ^e Non Seismic Methods. Repsol Exploration, c/ Méndez Álvaro, 44, 28045, Madrid,
17 Spain.

18 ^f Dpt. de Física i Enginyeria Nuclear, Polytechnic University of Catalonia (UPC). Física
19 Ed. TR1 (EET) C/Colom, 1, 08222 Terrassa.

20 ^g Instituto de Geociencias – IGEO (UCM, CSIC), C/ José Antonio Novais, 12, 28040
21 Madrid, Spain.

22 *Corresponding author. Tel.: +34 925268800

23 E-mail address: Rosa.Carrasco@uclm.es (R.M. Carrasco)

24

25 **Abstract**

26

27 The geometric and genetic characterization of the Navamuño depression
28 | peatland system (Iberian Central System) is presented here using [results from a](#)
29 geophysical survey. This depression is a ~30 ha pseudo-endorheic flat basin over
30 granitic bedrock. Three geophysical techniques were used to map the subsurface
31 geology, and identify and describe the infill sequence: shallow seismic refraction (SR),
32 magnetic resonance sounding (MRS) and electrical resistivity measurements (VES and
33 | ERT).

34 The three main geoelectrical layers (G1, G2, G3) identified in previous
35 research, have also been identified in the present work. Using the data obtained in this
36 new research we have been able to analyse these three geological layers in detail and
37 reinterpret them. They can be grouped genetically into two sedimentary units: an
38 ancient sedimentary body (G3), of unknown age and type, beneath an Upper
39 Pleistocene (G2) and Holocene (G1) sedimentary infill. The facies distribution and
40 geometry of the Upper Pleistocene was examined using the Sequence Stratigraphy
41 method, revealing that the Navamuño depression was an ice-dammed in the last
42 | glacial cycle, resulting a glaciolacustrine sedimentation.

43 A highly permeable sedimentary layer or regolith exists beneath the
44 glaciolacustrine deposits. Below 40 m depth, water content falls dramatically down to a
45 | depth of 80 m where unweathered bedrock may be present.

46 The information obtained from geophysical, geological and geomorphological
47 studies carried out in this research, enabled us to consider various hypotheses as to
48 | the origin of this depression. According to the [eseis](#) data, the Navamuño depression may
49 be explained as the result of a transtensional process from the Puerto de Navamuño
50 strike-slip fault during the reactivation of the Iberian Central System (Paleogene-Lower
51 Miocene, Alpine orogeny), and can be correlated with the pull-apart type basins
52 described in these areas. The neotectonic activity of this fault and the ice-dammed

53 processes in these areas during the Last Glacial Cycle (MIS2) were the main causes of
54 recent sedimentary infill in this depression.

55

56 **Keywords:** Near Surface Geophysics, Nuclear Magnetic Resonance, intermountain
57 basin, distensive faulting, Late Glacial Period, Iberian Central System.

58

59 1. Introduction

60

61 The small endorheic depressions known as *navas* are flat, treeless areas,
62 usually intermountain and sometimes marshy, common throughout the Iberian Central
63 System (ICS). The recent sedimentary evolution of these depressions involves slope,
64 fluvial and nival processes, and in some cases glacial and fluvioglacial processes
65 (Pedraza, 1994). As a result, these depressions have traditionally been studied to
66 reconstruct the environmental conditions pertaining in the ICS during the Quaternary
67 (see Ruiz-Zapata et al., 2011; López-Sáez et al., 2014). However, only very limited
68 data have been obtained to date relating to our understanding of the glacial record in
69 these areas (Ruiz-Zapata et al., 2011; López-Sáez et al., 2016). In previous studies,
70 the sedimentary infill analysed was of limited thickness (3 - 6 m), mainly homogeneous
71 (often only two sedimentary sequences appear) and not pre-Holocene in age (e.g.
72 Franco-Múgica, 1995; Rubiales et al., 2007; López-Sáez et al., 2014; Abel-Schaad et
73 al., 2014; Génova et al., 2016).

74 Taking these precedents into account, one of the aims of the research which
75 commenced several years ago into the ICS Pleistocene glaciation (Carrasco et al.,
76 2009), was to carry out a geological and geophysical prospective of these *nava*-type
77 depressions located in the former glacial areas. In the Navamuño depression (ND), one
78 of the *navas* analysed, a series of indicators was detected enabling the working
79 hypothesis that the ND is a unique case in the ICS. This interpretation was based on

80 the thickness of the sediments hosted by the depression and their possible genetic
81 relationship with the neotectonic activity and glacial dynamics of the Cuerpo de
82 Hombre, one of the reference paleoglaciers used for glacier evolution research in the
83 ICS (Carrasco et al., 2015a, 2015b).

84 With this approach, the main aim of this study is to establish in detail the
85 geometry of the ND, and interpret the thickness and sequence of its sedimentary infill
86 and its genetic context. ~~Previous works~~~~The essential basis for this approach was the~~
87 ~~available data obtained from earlier research~~ (Ruiz-Zapata et al., 2011; Carrasco et al.,
88 2015a, 2015b; Turu et al., 2018a) ~~provided the essential data to support the present~~
89 ~~study of the~~~~into the glacier chronology and sedimentary characteristics of part of the~~
90 ~~infill materials in the~~ ND trough.

91 The methods chosen with this aim in mind were based on those applied in other
92 mountain systems in the Iberian Peninsula using geophysical techniques supported by
93 detailed geological surveys (Vilaplana and Casas, 1983; Bordonau, 1992; Turu 1999;
94 Turu et al., 2007, 2011; Pélachs et al., 2011; Pellicer et al., 2012; Salazar-Rincón et al.,
95 2013). Taking as a base the three resistivity levels identified in a previous study (G1,
96 G2, G3; Carrasco et al., 2015a), ~~in ND~~ Electrical Resistivity Tomography (ERT),
97 Vertical Electrical Sounding (VES), Magnetic Resonance Sounding (MRS) and Seismic
98 Refraction (SR) have been applied in the ND for detecting and defining the presence of
99 sharp geological contacts (ERT and SR) such as faults or buried paleo-relief, sub-
100 horizontal stratigraphy (VES) and aquifers (MRS).

101

102 **2. Geological and geomorphological setting**

103

104 *2.1. Regional context*

105

106 The ND is located at 1500 m above sea level (asl) on the western versant of the
107 Sierra de Béjar (ICS, Fig. 1) with a surface area of ~30.76 ha. This depression is

108 confined between scarped slopes on the granitic basement and one of the moraines of
109 the Cuerpo de Hombre paleoglacier (Fig. 2). The bottom of the depression is a
110 seasonal flood-plain with peatland development, currently dissected by fluvial
111 channels.

112 ND forms part of the fracture corridor associated with the Puerto de Navamuño
113 fault (PN fault) and has been classified as a Variscan strike-slip fault (Bellido-Mulas,
114 2006) associated with the NE-trending strike-slip faults of Alentejo-Plasencia (AP;
115 a.k.a. Plasencia, Odemira-Plasencia, or Messejana-Plasencia; > 500 km) and Hervás-
116 Candelario (HC; around 40 km) (Fig. 1). Together these faults are responsible for the
117 Jerte-Aravalle and Hervás-Candelario corridor-type valleys which limit the Sierra de
118 Béjar pop-up (Sanz-Donaire, 1979; Moreno, 1991; Carrasco, 1997).

119 All these reliefs were formed during the Alpine Orogeny as the result of the
120 transmission to the interior of the Iberian Plate of the compressive stress generated at
121 its edges due to collision with Eurasia during the lower Oligocene-Miocene
122 (Cantabrian-Pyrenean) and with Africa since 9 Ma (De Vicente and Vegas, 2009). De
123 Vicente et al. (2007) and De Vicente (2009) propose partitioning of deformation in the
124 ICS with a generalized NNW-SSE shortening in a transpressive regime. This regime
125 has not varied substantially from the Oligocene to the present, although its maximum
126 intensity was concentrated during the Lower Eocene-Miocene (Continental Iberia-
127 Eurasia collision). Fission track dating (De Bruijne and Andriessen, 2002), seismicity
128 (Olaiz et al., 2009; Muñoz-Martín et al., 2012), and GPS (Garate et al., 2015) data
129 confirm this model.

130 Minor depressions such as the ND are common throughout the ICS and the
131 Iberian Massif and have been analysed in depth along the AP fault (Brum da Silveira,
132 1990; Carrasco and Pedraza, 1991; Cabral, 1995, 2012; Capote et al., 1996; Brum da
133 Silveira et al., 2009; De Vicente et al., 2011; Villamor et al., 2012). According to these
134 data, these depressions originated in the Paleogene-Lower Miocene as pull-apart type
135 sedimentary basins and some of them continued active throughout the Miocene.

136 Others, however, halted at the start of the Upper Miocene and their function changed to
137 shallow sedimentary basins regulated by neotectonic readjustments during the recent
138 times (Upper Pliocene and Quaternary). In other ICS depressions developed on a rock
139 substratum (El Burguillo and Alto Tormes valleys; Fig. 1), some anomalies detected in
140 the layout of the current drainage network have also been interpreted as indicators of
141 neotectonic activity (Vazquez et al., 1987; Pol et al., 1989).

142 | Although this area of the ND is presently characterized by moderate to very low
143 seismic activity, according to instrumental and historical records (IGN, 2016), the 1755
144 Lisbon earthquake (Mendes-Victor et al., 2009) originated small-scale slope
145 movements in the Valle del Jerte (11.83 km SE of ND) and resulted in cracks in the
146 walls and partial roof collapse in some monumental buildings in the city of Plasencia
147 (40.53 km SW of ND) (Carrasco, 1997; Udías and López-Arroyo, 2009). On the other
148 hand, and this is one of the fundamental points under debate, the neotectonic activity
149 of these faults during the Quaternary is framed within the context of low deformation
150 rates, reflected in the presence of slow faults with much longer return periods than the
151 time period covered by the historical or instrumented seismic data (Cabral, 2012;
152 Foroutan et al., 2016).

153 | The lithological context of the ND substratum is that of the Sierra de Béjar,
154 which forms part of one of the most important granitic batholiths of the Iberian Massif
155 | (Villaseca et al., 1999; Villaseca, 2003). The most abundantfrequent rocks in the area
156 are monzogranites and Variscan granodiorites, with associated migmatites, schists,
157 quartzites and other pre-Variscan metasediments. In the ICS, and the Iberian Massif in
158 general, various supergenic weathering sequences have been identified in these
159 granitic substrata. The oldest (pre-Tertiary), thick weathering mantles correspond to
160 laterite profiles (Molina-Ballesteros et al., 1991, 1997). The most recent weathering
161 mantles (Tertiary and in some cases Quaternary) are less thick, sometimes sub-
162 surficial, and are associated with wash-exposure rock weathering stages and therefore
163 their transformation levels vary, ranging from simple bisialitization (predominance of

164 | montmorillonite) to monosialitization (predominance of kaolinite) (Centeno and Brell,
165 | 1987; Molina-Ballesteros et al., 1994).

166

167 | 2.2. Study area and hypothesis

168

169 | In earlier studies of the ND (Carrasco et al., 2015a), a sedimentary trough was
170 | detected, occupying part of the depression and hosting sediments calculated to be
171 | approx. 60 m thick. The sedimentary sequence, established from lithologicaldirect data
172 | (16 m test bore) and from data obtained using geophysics, consists of three
173 | geoelectrical layers (Carrasco et al., 2015a; Turu et al., 20187a): G1 (10-18 m thick),
174 | nearest the surface, interpreted as coarse sand with intercalated clays and silts,
175 | sometimes presenting zones with organic material indicating the presence of
176 | paleochannels and/or peatbog zones; G2 (7-10 m thick in some zones, 40-50 m thick
177 | in others), interpreted either as a sedimentary debris-flow deposit, highly porous,
178 | coarse-grained, and saturated with water (arkosic), or as arenized granite; and G3
179 | substratum of the trough on non-weathered granitic rock. The nomenclature of these
180 | layers has been maintained in this research, although the layers may be redefined with
181 | the new data obtained. ¹⁴C dating establishes approximate ages of 5700 BP for a
182 | sample located at 485 cm and 10000 BP at a level one meter lower (565-570 cm) and
183 | 13720 BP for a level located at depth 16 m (Ruiz-Zapata et al., 2011; Carrasco et al.,
184 | 2015a; Turu et al., 20187a).

185 | These earlier studies mentioned the possibility that the evolution of the
186 | sedimentary trough in ND was related to an obstruction process generated by the left-
187 | lateral moraine of the Cuerpo de Hombre paleoglacier, which defines the eastern
188 | margin of the depression. The abrupt change of direction presented by this left lateral
189 | moraine of the Cuerpo de Hombre, aligned along NW-SE and NNE-SSW structures,
190 | has also been highlighted in various studies (Rubio, 1990; Carrasco et al., 2013,
191 | 2015b). This left-lateral moraine forms part of the morphostratigraphic formation called

192 'principal moraine' (PM), and has been used as reference to establish the evolutive
193 sequence of the ICS paleoglaciers (Pedraza, 2012; Pedraza et al., 2013; Carrasco et
194 al., 2013).

195 The evolutive sequence in the Cuerpo de Hombre paleoglacier was dated using
196 ^{10}Be -TCN technique on scattered erratic blocks or moraine boulders. As a result of this
197 work, the following ages have been established (Carrasco et al., 2015b) (Fig. 2A, 2C):
198 (1) glacial maximum (~25.0 ka; MIS2); (2) some retreat and stabilization stages formed
199 after ~24.3 ka and before ~20.6 ka; (3) some readvance and stabilization phases
200 shown by the PM formation, dated later than ~20.6 ka and earlier than ~17.8 ka; and
201 (4) a deglaciation process showing three stadials in the late glacial sequence dated to
202 (minimum ages) ~17.5 ka, ~13.9 ka and ~11.1 ka.

203 All these earlier data as well as those corresponding to the regional geological
204 context described in the previous section, were used as the basis for the central
205 hypothesis on which ~~the~~ new research described herein was planned and carried out.
206 This hypothesis considers that the primary origin of the ND converged with the pull-
207 apart type basins described in these areas, and its recent evolution was associated
208 with some tectonic readjustments and with the Cuerpo de Hombre paleoglacier. Thus,
209 the chronoevolutive sequence of this paleoglacier has been used as reference to
210 establish the sequence and chronology of the infill stages of the ND depression during
211 the obstruction period.

212 This is a topic of general interest in the study of paleoglaciers, since it related to
213 the impact of non-climatic factors on glacier dynamics and therefore on the typology
214 and arrangement of geomorphological indicators used as reference to establish
215 chronologies, evolutive sequences and global paleoclimatic deductions (Olvmo and
216 Johansson, 2002; Ber, 2009; Glasser and Ghiglione, 2009; Cotton et al., 2014; Yanites
217 and Ehlers, 2012; Prasicek et al., 2015; Bathrellos et al., 2017).

218

219 **3. Methods**

220

221 *3.1. Surficial geology and fracture network*

222

223 Geological mapping was produced using vertical aerial photographs (Scale 1:
224 10000 and 1:18000) and PNOA-2014 orthophotos (Instituto Geográfico Nacional, IGN).
225 This procedure and field surveys were used to define the geological and
226 geomorphological units presented in this study.

227 There was abundant information previously available on the bedrock lithology
228 (Bellido-Mulas, 2006) and the glacial morphology of the Sierra de Béjar and its
229 immediate surroundings as a whole, including the ND (Sanz-Donaire, 1979; Rubio
230 1990; Carrasco, 1997; Carrasco et al., 2013, 2015a, 2015b). Nevertheless, the
231 boundaries of the depression and contacts between the different lithological formations
232 have had to be mapped with new, complementary data. A detailed morphotectonic
233 information has also been produced which includes scarps, alignments, fractures and
234 fracture corridors. The main aim of this information is to contribute a complementary
235 data series to the geophysical research into the deposits hosted in the depression, as
236 this is where the search has been focused for indicators to interpret the genesis and
237 evolution of this depression and the possible existence of neotectonic activity. This
238 methodological approach takes into account the precedents described above in
239 | Section 2.0 (~~Geological and geomorphological setting~~), to interpret neotectonic activity
240 in these areas. In all cases, indicators of this activity have been obtained in the
241 sedimentary fill in the depressions (fractured or folded sediments, abrupt or anomalous
242 contacts, etc.). This is because the data provided by the rock substrate formations are
243 limited to some faceted surfaces and anomalies in the drainage network which are
244 often difficult to interpret and must be obtained by studying wider areas than the
245 intermountain depressions. On the other hand, this information is a basis for correlation

246 with morphostructures established at a regional level in other depressions similar to the
247 ND, such as the Amblés, Jerte and Garganta del Villar valleys (Fig. 1).

248 The aim of the field work was to carry out a detailed review of the geological
249 formations obtained from photointerpretation and to characterize the typology of some
250 surficial formations not analysed in previous studies. In this review special attention
251 was paid to the location and typology of weathered bedrock materials (*grus*), as in
252 some cases these formations present hydrogeological, geotechnical and geophysical
253 characteristics similar to the arkose formations which appear in some ICS intermountain
254 depressions.

255

256 3.2. Geophysical methods

257

258 3.2.1. Vertical electrical soundings (VES) and Electrical resistivity tomography (ERT)

259

260 Electrical resistivity methods (VES and ERT) consist ~~of~~ⁱⁿ obtaining the apparent
261 resistivity (ρ_{ap}) of rocks and soils from the voltages observed in potential electrodes, in
262 response to the introduced DC intensity ~~in~~^{of} the ~~continuous electric current injected into~~
263 current electrodes. If the distance between the current electrodes is gradually
264 increased in relation to a central point, the vertical resistivity distribution can be
265 examined, i.e. in 1D (VES). In ERT an electrode array is deployed laterally along a
266 profile, obtaining a 2D resistivity model of a subsoil section (Reynolds, 2011). The ERT
267 results obtained enable an understanding of the bedrock geometry and differentiate
268 infill types from their contrasting electrical resistivity (Descloitres et al., 2008;
269 Hausmann et al., 2013).

270 VES data acquisition was completed in 3 survey campaigns: the first two
271 provided a preliminary estimation of the depression geometry (Carrasco et al., 2015a)
272 and the third completed the data required to define the geometry and produce the final
273 infill model. All VES were carried out with a Schlumberger-type configuration and the

274 maximum array length is 266 m (Fig. 3). For a correct interpretation, the 'apparent'
275 resistivity values (i.e. the mean value of the rock volume affected by the current flow)
276 must be converted to 'real' resistivity of the different subsoil units using an inversion
277 process, in either 1D (VES, Zohdy, 1989; Barker, 1992) or 2D (ERT, Loke and Barker,
278 1996; Loke et al., 2010). In the case of VES, due to the principle of electrical
279 equivalence (Maillet, 1947; Bhattacharya and Patra, 1968; Reynolds, 2011), there is
280 inherent uncertainty in the method, in that the electrical behaviour of a layer is defined
281 by the combination of its thickness and its resistivity, which may generate important
282 uncertainty. This uncertainty is limited or resolved by: (1) an equivalence analysis and
283 (2) inclusion of other subsoil survey techniques. In the ND the VES inversion and
284 equivalence analysis were performed using Moscow State University IPI2Win free
285 software (Bobachev et al., 2003), obtaining a 1D resistivity model and corresponding
286 equivalence analysis (see supplementary material).

287 ERT data were collected in field work using a RESECS DMT 64 channel
288 resistivity meter with 5 m spacing between electrodes. Nine profiles were measured
289 with lengths from 205 - 275 m (Fig. 3). Wenner and Dipole-Dipole electrode
290 configurations were used and the maximum depth reached was 70 m.

291 RES2DINV software (Loke and Barker, 1996; Loke et al., 2010) was used for
292 field data inversion. A normal inversion algorithm using 4-node finite element modelling
293 has been used. The size of the elements was the same as the distance between
294 electrodes (5 m). The resistivity data were of very good quality with high S/N ratio, and
295 repeat measurement errors below 1%. The ND data inversion models gave
296 consistently low error statistics with RMS <3%. The result of all this information,
297 combined with VES, enabled a better understanding of the 2D distribution of the
298 different geo-resistive bodies and how they relate to surface geomorphological and
299 geological data.

300

301 | 3.2.2. Magnetic ~~r~~Resonance ~~s~~Sounding (MRS)

302

303 The MRS technique is applied in different geological contexts (Behroozmand et
304 al., 2015), and allows quantification of porosity, permeability and thickness of aquifer
305 levels to a depth of the first 150 m (Yaramanci, 2000; Vouillamoz et al., 2007; Lange et
306 al., 2007; Mejías and Plata, 2007; Plata and Rubio, 2008; Hertrich, 2008).

307 | MRS is based on the properties of ~~n~~Nuclear ~~m~~Magnetic ~~r~~Resonance (NMR)
308 which uses the resonance produced in protons subjected to a magnetic field with a
309 specific frequency. The method consists in energising the terrain with an increasing
310 electromagnetic pulse moment (q , in A·ms) generated in a loop, with the aim of
311 penetrating deeper into the subsoil (Table 1). When the pulse terminates, the terrain
312 response is logged as initial amplitude, (E_0 in nV), decay time (ms) and phase
313 (degrees). The initial amplitude value (E_0) is directly related to the amount of water
314 contained in the soil to the slice depth affected by the pulse, while the decay time ($T2^*$)
315 depends on the hydraulic permeability. To suppress random noise and improve the
316 signal/noise ratio, each pulse is repeated several times for signal-stacking purposes.
317 Greater depth is reached in the research by increasing the value of q , with a maximum
318 depending on the loop dimensions. The test sounding consists of various
319 measurements of increasing values of q , to establish functions E_0 and $T2^*$ as a function
320 of q .

321 These parameters depend on the electrical conductivity of the subsoil, magnetic
322 field (inclination and magnitude), loop size, electromagnetic noise and possible
323 presence of magnetic rocks (Weichman et al., 2000; Hertrich, 2008).

324 | Two MRS soundings were carried out in the ND₇ at the same point₇ but using
325 different sized loop (30x30 m and 60x60 m) (Fig. 3). This survey method has been
326 | successfully tested in other geological contexts (Turu, 2012; [Behroozmand et al., 2015](#))
327 | with a twofold aim: to achieve sounding to the maximum depth possible with the
328 | apparatus used but without resolution loss in the first tens of meters of the subsoil.

329 NMR data were collected in the field using Iris-Instruments NUMIS LITE equipment
330 which can penetrate to maximum depth 90 m. The field data inversion was performed
331 using Shushakov and Legchenko (1994) and Legchenko and Shushakov (1998)
332 methods, and the results obtained enabled 1D quantification of the hydrogeological
333 parameters mentioned above.

334

335 3.2.3. Seismic refraction (RS)

336

337 Seismic techniques are often used to study Quaternary deposits and research
338 the subsoil layers, paleorelief geometry and geomechanical properties of surficial
339 deposits (Turu, 1999; Turu et al., 2007; Schrott et al., 2003; Yamakawa et al., 2012).
340 This technique is based on measuring the travel time of P waves which travel directly
341 or critically refracted to a geophone array deployed along a seismic line (Sheriff and
342 Geldart, 1991; Reynolds, 2011). Analysis of the travel times picks from each source to
343 the geophone array are plotted as time/distance curves on a time-distance graph. The
344 qualitative analysis of these travel times using the general reciprocal method (GRM)
345 (Palmer, 1980), or tomographic techniques (Watanabe et al., 1999; Sheehan et al.,
346 2005), enables reconstruction of the contacts between different media (refractors) and
347 the depth distribution of the P wave velocities. The seismic source used varies
348 depending on the test depth, and a sledge hammer is usually used in superficial
349 studies to reach depths of up to 25 m.

350 The results obtained by seismic refraction are a 2D vertical section of the P
351 wave velocity distribution (V_p), with lateral resolution defined by the distance between
352 the geophones (normally 1 - 5 m).

353 The seismic survey in the ND centred on the axial zone and on its northern
354 margins. Five 48 m-long seismic refraction profiles were generated, with geophones
355 regularly spaced at 6 m intervals (Fig. 3). The seismic waves were generated by
356 percussion with a 6 kg hammer on a metal plate placed on the ground, with shooting

357 points at each end and in the centre of the profile. As the ND is included in a Special
358 Protection Area for birds, more efficient seismic wave generation methods were ruled
359 out.

360 The seismograph used was a 16-channel prototype designed by the
361 Universidad Politécnica de Cataluña (UPC). Signal processing and inversion was
362 performed using specific software (Anasim 6.0; Herrero-Simón, 2003) which allows
363 detection of refracted and reflected waves and subsequent subsoil characterization
364 using models of inclined layers (velocity, depth and inclination). This was particularly
365 useful in the peat bog profiles, as the low ground compaction muffled the signal
366 generated with the hammer. The results obtained were verified using Simusism2
367 software (Herrero-Simón, 2007), also produced by the UPC, which simulates seismic
368 wave propagation in subsoils with random velocity distribution.

369 The aim of the seismic refraction ~~aim here~~ was to define the contact between
370 low-velocity to higher-velocity layers, such as from overburden to bedrock and/or highly
371 weathered rocks, and from peat to clastic sediments. Also the presence of
372 discontinuities in the upper surface of the basement, produced by faults and/or erosive
373 surfaces. In these cases, sharp contacts such as occur in a gully or in faults, delay the
374 wave arrival time and disturb the dromochronic representation. Where this occurs, the
375 throw can be calculated as the delay is exponentially related to the seismic velocity of
376 the layers involved.

377

378 **4. Results and interpretation**

379

380 Although the ND is generally rectangular in shape, bounded by mainly
381 rectilinear scarp slopes, when analysed in detail the boundaries are found to be
382 more complex. The slopes forming the northern and western sides are formed on
383 granitic rocks (monzogranites and porphyritic biotite granodiorite; Bellido-Mulas, 2006)
384 and associated with NE-SW and NNE-SSW fractures (Fig. 4). The mainly rectilinear

385 northern boundary is due to a minor ENE-WSW fault. The western boundary is less
386 regular, with directional changes originating in a series of minor faults, which displace
387 the two main NNE-SSW and NNW-SSE faults. These morphostructural differences are
388 also clearly seen in the fluvial plain forming the floor of the depression and in the
389 granitic materials. The northern area of this fluvial plain is directly linked to the scarp
390 slope with a clear knickpoint slope break and the granitic rock appears fairly fresh. In
391 the western part, however, between the scarp slope and the fluvial plain,
392 intermediate minor *glacis* reliefs are seen, formed on the weathered rock substratum
393 *grus* and surficial deposits (lithosoils and slope deposits; Figs. 2B, 5).

394 The granitic materials are in general unweathered and very heavily fractured.
395 The weathered rock is found in bands associated with fractures, and on the surface
396 forms a regolith composed of *grus*, scree and soil. ~~In At the~~ places where the weathered
397 rock can be observed in situ, and in line with standard field classifications (Anon, 1977;
398 Dearman, 1978), two degrees of transformation can be identified: Grade III (moderate),
399 in which the rock shows general discolouration and is easily broken by hand, although
400 ~~most of the~~ majority of minerals are recognizable most of the original textures have
401 been lost; and Grade II (slight), in which the original minerals, textures and structures
402 of the rock are recognizable (although the rock is difficult to break up by hand and there
403 are abundant fragments of fresh rock) ~~but,~~ shows discolouration due to migration of
404 iron oxides resulting from the transformation of certain minerals, particularly biotite.

405 The southern boundary is more complex and is defined by a system of steps
406 and shoulders due to two fault sets, one parallel to and the other conjugate with the PN
407 fault. These steps have been fossilized and smoothed by the outermost surficial
408 deposits of the Cuerpo de Hombre paleoglacier and by a torrential fan system. All
409 these geomorphical features penetrate into the interior of the depression and mark the
410 southern limit of the base fluvial plain. Finally, the eastern boundary, defined by the
411 slope corresponding to the left lateral moraine of the Cuerpo de Hombre paleoglacier,

412 is fairly rectilinear and is parallel to the western side, with a clearly defined contact with
413 the depression base fluvial plain (Figs. 2, 5).

414 The base of the depression is a fluvial plain where a channel system forms a
415 general network pattern, with occasional meanders or anastomosis and some flood
416 zones where small peatland and marshy formations accumulate.

417

418 4.1. Vertical Electrical Soundings (VES)

419

420 Three geoelectrical layers have been detected in the ND, confirming and
421 complementing previously obtained data (Carrasco et al., 2015a). These layers are
422 called G1, G2 and G3 from highest to lowest (Table 2, Fig. 5).

423 The first resistive layer (G1) is found immediately under the ground surface and
424 has variable resistivity, due to its heterogeneous lithological composition. In general
425 terms, it is 3-4 m thick, although in the southernmost part of the depression centre, a
426 thickness of up to 20 m has been detected (VES 8).

427 The second resistive layer (G2) obtains resistivity values ranging from 500 - 800
428 Ωm , except in the distal zone of the depression (between VES 5 and 9) ~~which~~
429 exhibits contrasting resistivity values of 250-300 Ωm . Where geoelectrical layer G2 has
430 been identified, the thickness varies, oscillating between 20 and 50 m.

431 The third resistive layer (G3) corresponds to the deepest sediment levels
432 deposited in the depression and overall this layer displays resistivity values between
433 600 and 1600 Ωm .

434 In general, stacking of the three geoelectrical layers is observed but exceptions
435 are found at the edges of the depression. Close to the moraine (Fig. 5) the three
436 geoelectrical levels described are detected in VES 1 position, and also resistive
437 deposits which form the lateral moraine of the Cuerpo de Hombre paleoglacier (Fig. 6,
438 ERT 1 and ERT 2). In contrast, the geoelectrical layers are not present above the
439 moraine sediments (VES 3). The absence of contrasting electric resistivity between

440 levels G3 and G2 in the central sector of the depression (VES 6) makes them difficult
441 to separate with this survey method. In the northern sector (VES 4) the existence of the
442 nearby crystalline basement did not facilitate sedimentation of all the geoelectrical
443 layers. The granitoid basement with characteristic relatively high resistivity (around
444 2000 Ωm) was identified in the central area of the depression (VES 7 and VES 8) from
445 the abrupt slope change shown by the resistivity curve, otherwise it is difficult to detect,
446 as for example in VES 4 and 6. VES 5 is the only one with an H-type curve, which
447 means that the second layer has a lower resistivity than the one above and the one
448 below. For this reason, VES 9 was carried out nearby. The final VES has 4 layers and
449 any significant continuity in the intermediate layer is ruled out. For this reason, a
450 dashed line is drawn between VES 9 and VES 5 on the map in Fig. 5.

451

452 4.2. *Electrical Resistivity Tomography (ERT)*

453

454 The depth reached in the ERT sections ranged between 40 and 60 m and the
455 three geoelectrical layers defined above (and previously, Carrasco et al., 2015a) are
456 identified, i.e. G1, G2 and G3 (Fig. 6).

457 Geoelectrical layer G1 exhibits the greatest resistivity (1600 - 16000 Ωm). This
458 implies genetically that G1 has a larger overall grain size and a lower silt and clay
459 content (cf. Waxman and Smits, 1968). In geometric terms, there are notable thickness
460 variations of this layer (ERT 3, Fig. 6). Sedimentary accretion (ERT 3 and ERT 7, Fig.
461 6), denotes greater accommodation northwards, at the depression centre.

462 The contact between layer G1 and the other two layers displays paraconformity in
463 ERT 3, and overall concordance in ERT 1 and ERT 7, above all towards the
464 depression centre (ERT 2 and ERT 8, Fig. 6). In G1, the onlap contact of the resistive
465 materials in ERT 7 and ERT 1 is observed with sedimentary aggradation towards the
466 depression centre. Less marked onlap contact can also be deduced from the
467 synsedimentary tilting of the base of layer G2 in the central part of the depression (ERT

468 2). These onlap contacts are interpreted as tilting (as in ERT 2) or fossilization of fault
469 scarps (as in ERT 7 and ERT 1) which affect the basement rock (layer G3). The
470 subsidence activity would then be responsible for the synsedimentary accretion
471 towards the north in layers G1 and G2 (ERT 1 and ERT 7). Finally, the granitic
472 substratum which forms the depression boundary is identified by the sharp lateral
473 resistivity contrasts with layers G2 and G3 (ERT 2 and ERT 8, Fig. 6). This sharp
474 contact is interpreted as the confinement of sedimentary infill by sinking of the rock
475 basement. Subsidence activity would then be responsible for the synsedimentary
476 accretion towards the north in layers G1 and G2 (ERT 1 and ERT 7). Finally, the
477 granitic substratum which forms the depression boundary is identified by the sharp
478 lateral resistivity contrasts with layers G2 and G3 (ERT 2 and ERT 8, Fig. 6). This
479 sharp contact indicated in Fig. 6 is interpreted as the confinement of sedimentary infill
480 by sinking of the granite basement.

481 Geoelectrical layer G2 is more heterogeneous than G1 and with lower resistivity
482 | (20 - 2000 Ω m). This layer ~~exhibits~~presents greater geometrical development towards
483 | the centre of the basin and marked lateral variations in resistivity, especially in the
484 | central zone of the depression (ERT 2, ERT 8, Fig. 6). Thus, the fine-graineded
485 | sedimentary facies (silts and clays) are interpreted in the conductive nuclei in ERT 2
486 | and ERT 8 and should be attributed to lacustrine environment deposits. On the
487 | contrary, the most resistive bodies correspond to coarse-graineded sedimentary facies
488 | (sands and gravels), attributable to fluvial environment deposits (ERT 2, Fig 6).

489 Geoelectrical layer G3 corresponds to the lower level of the ND infill, with low
490 resistivity (200 - 2000 Ω m) contrasting with the rock substratum resistivity (2000 -
491 20000 Ω m). This geoelectrical layer rests directly on the resistive rock substratum in
492 the centre of the depression (ERT 2 and ERT 8, Fig. 6). In the southern sector of the
493 depression, G3 presents an important vertical variation in resistivity and also horizontal
494 variation, although to a lesser degree. In e.g. ERT 7, vertical values range from 3 k Ω m

495 to up to ten times lower. In contrast, the horizontal resistivity ratio is half of that
496 detected on the left margin of ERT 1 and ERT 3 and that of the opposite edge (Fig. 6).
497 These resistivity variations can be interpreted as variations in the sedimentary infill
498 grain size, just as in geoelectrical layer G2. However, the nature of the geoelectrical
499 layer G3 is unknown, in contrast to that of G1 and G2 which have been identified by
500 [Carrasco et al. \(2015a\) in a 8 m depth borehole performed mechanical sounding](#) in the
501 centre of the depression ~~for Carrasco et al. (2015a)~~.

502 Three test bores were performed in ND, with one reaching a maximum depth 16
503 m, and used for paleoenvironmental studies (Ruiz-Zapata et al., 2011; Carrasco et al.,
504 2015a; Turu et al., 20187a). In this sounding, 3 layers can be distinguished from top to
505 bottom: the top layer (0-300 cm) is composed of clayey silt interspersed with gravel
506 (geoelectric unit G1); the second layer (300-800 cm) comprises sands with beds of
507 finely-laminated clay to 500 cm, and then sands and gravels interspersed with beds of
508 clays and silts to the bottom of the sounding (geoelectric unit G2). Carbon-14 dating
509 [presented](#) in Carrasco et al. (2015a) and Turu et al. (20187a) shows approximate ages
510 of 5700 BP for a sample located at 485 cm and 13720 BP for a level located at depth
511 16 m. This indicates that in the central part of the depression, the bottomset is Late
512 Glacial [in age](#).

513

514 4.3. Magnetic Resonance Sounding (MRS)

515

516 Two double pulse MRS were performed in ND. Quantitative results show that
517 contact with the impermeable substratum is located at a depth of approximately 80 m,
518 while at 50 - 70 m there is a zone with gradually decreasing porosity and permeability
519 (Figs. 7C, 7D). Interpretation of the field-curve data from the two surveys undertaken
520 suggests that water is present in all geoelectrical layers in the first 30 m (Fig. 7C),
521 decreasing the water content from 30 to 60 m depth. The main aquifer is found in the
522 first 40 m from the subsurface, although it reflects the inherent heterogeneity of the

523 depression infill sedimentary deposits (Fig. 7C). The infill layer down to 40 m,
524 containing the main aquifer, corresponds to electrical units G1 and G2, while the zone
525 with gradually decreasing permeability (40 - 80 m) corresponds to unit G3. This unit
526 exhibits relatively high values of resistivity with lateral changes, and a progressive
527 decrease in water content and permeability. The most likely interpretation of its nature
528 are the following: (1) that it is a sedimentary infilling with a lower porosity towards its
529 base; and (2) that it is a zone of altered basement rock, with a maximum alteration at
530 its top, and a reduction with depth.

531 Water is not detected in the main aquifer at depths of 13 - 17 m. Given that only
532 free water is detected by MRS, this apparently small quantity of water can only be
533 justified by the presence of low porosity in clay deposits. In addition, the free water
534 presence in the clay displays a very short relaxation time (Fig. 7D) in the MRS signal
535 and may not be detected due to instrumental limitations (Turu, 2012). The relaxation
536 time of the water signal is a permeability-related parameter (Mejías and Plata, 2007)
537 and both $T2^*$ and $T1$ show a wide range of values (Figs. 7E, 7F). This is interpreted as
538 significant infill grain-size variability, ranging from clay and silt (100 ms; Fig. 7E) to
539 sand and gravel (values higher than 300 ms; Fig. 7F). However, $T2^*$ and $T1$ relaxation
540 times do not converge at all depths. Usually $T1 > T2^*$ but in the case that they are not,
541 $T1$ measurements are more approximate and pseudo-saturation recovery
542 complications would not produce a 90° pulse and distribution of tip angles, reducing the
543 estimation of $T1$ (Grunewald and Knight, 2011). This is the case for Fig. 7E at a 22 m
544 depth; here $T2^* > T1$ (Fig. 3F), just at the bottom of the inferred fine grained deposits or
545 low resistive (ERT 8, Fig. 6). If $T2^* \ll T1$ then paramagnetic geology produces
546 inhomogeneous field dephasing, due to magnetic grains or field-scale magnetic
547 anomalies reducing $T2^*$ relaxation time (Walsh, 2008). This seems to be the case
548 below a depth of 36 m, where $T2^*$ is systematically lower than $T1$.

549

550 4.3. Seismic Refraction (RS)

551

552 The seismic refraction sections performed along the northern edge of the
553 depression allowed the reconstruction of an NW-SE transect to 15-20 m in depth (Fig.
554 8). In this section the contact can be observed between the sedimentary infill (V_p
555 between 350 and 1350 m/s, Table 3) and the rock substratum ($V_p > 1800$ m/s). Minor
556 variations in sedimentary fill velocity were observed, interpreted as erosive surfaces,
557 but in general terms the refractions fit a stratified model.

558 In profile RS1 delays can be observed in the refracted wave reception time (Fig
559 8), which is linked to sharp contacts attributable to filled gullies, as ~~those ones that~~
560 ~~have been~~ described by Turu et al. (20187a). In the sector of this profile near the slope
561 and in RS5, the presence ~~was identified~~ of rock substratum is characterized by high
562 seismic velocity. In profile RS4, beneath the moraine and at a shallow depth, the rock
563 substratum has also been detected from its seismic velocity (ERT 8, Fig. 6 and Table
564 3).- The geological units detected in RS3 and RS4 are different at the edge of the
565 lateral moraine which is the boundary of the ND, interpreted as an onlap contact
566 between the moraine and the depression infill (Fig. 8). The absence of refracted waves
567 in this part of the profile is due to an inversion of the seismic velocity ($V_1 > V_2$), implying
568 that the underlying deposits are less dense than those nearer the surface. The
569 explanation for this anomaly may be related to the presence of a pressurized aquifer.

570 A refractor located at a depth of 9 m was identified in the overlap of the two
571 seismic profiles RS3 and RS2 (Fig. 8). Because of its continuity and increasing depth
572 towards the centre of the depression, this layer can be catalogued as a first order
573 reflector equivalent to the division of the sedimentary fill between the geoelectric layers
574 G2 and G3 in the electrical tomography profiles (ERT 8).

575

576 4.4. Stratigraphic architecture inferred from geophysical data

577

578 The architecture of the infill examined can be subdivided into depositional
579 sequences and system tracts, as has already been carried out in other glacial
580 obstruction depressions (Jalut et al., 2010; Turu et al., 2017b). The limits between
581 depositional sequences are the result of stratigraphic discontinuities and their
582 correlative surfaces throughout the basin under analysis (Vail et al., 1987). It is
583 therefore important to identify them from the layer geometry or sharp changes in their
584 properties (Turu et al., 2017b). Based on this, unconformity surfaces (US) are
585 highlighted on the electrical tomography profiles (Fig. 6).

586 The sedimentary fill of geoelectrical layer G1 was identified by Carrasco et al.
587 (2015a), allowing the depositional system of G1 to be described as fluvial type. Proof of
588 this is the contacts located in the seismic refraction profile (Fig. 8) that are associated
589 with paleochannels.

590 Geoelectrical layer G2 is interpreted as genetically related to an alluvial fan
591 supplied by marginal fluvioglacial flows from the Cuerpo de Hombre glacier. This delta
592 fan is centred on the kame terrace where fluvioglacial flows originated (Fig. 5). Thus,
593 there must have been a lacustrine paleoenvironment-sedimentation in the ND, T-and in
594 this kind-type of environment's-sedimentation progresses from the margin to the bottom
595 of lake-shore-margin-(in the ND located between ERT1 and ERT 2) as a Gilbert delta
596 type, in which the sediments are packing like sigmoids identified as -following
597 isochronic sigmoids (cliniforms) in the ERT survey. As occurs in other similar contexts
598 (Jalut et al., 2010; Turu et al., 2017b), in the ND drainage was obstructed by the ice
599 and/or the lateral moraine of the glacier. The low resistivity materials present in ERT 8
600 are therefore interpreted as fine-grained-size-material sediment at the bottom of this
601 ice-dammed lake.

602 As also observed in other areas (Turu et al., 2017b), the local base-level falls
603 and the sedimentary facies change when the ice-damming comes to an end, producing
604 diastems (unconformity surfaces-, US). These erosive surfaces (ERT 8) mark the start
605 of a new depositional sequence, initiating a Low System Tract (LST; Catuneanu, 2006).

606 When the obstruction ceases, lacustrine sedimentation also stops, and an alluvial fan is
607 initiated on the ND plain. The sigmoidal arrangement of clinofolds above the US in
608 ERT 8 is an example of this sequence. These clinofolds are formed from a lateral
609 accretion in the erosive entrenched channel, where migration of the sedimentary facies
610 proceeds according to Walther's law (Vera, 1994).

611 The sedimentary evolution on this fluvial plain varies depending on changes in
612 the local base level, which may be related to climatic factors (higher or lower moisture
613 contribution), glacial dynamics (retreat) or tectonics (greater subsidence or formation of
614 erosive scarps).

615 In ND clinofolds display offlap evolution (ERT 8, Fig. 6.) This type of evolution
616 is related to retrograde parasequences (Catuneanu, 2006). When maximum flooding is
617 reached the finest grain-size sediments are deposited (Catuneanu, 2006), and promote
618 low resistivities (Waxman and Smits, 1968) in ERT 8 (Fig. 6). This maximum flooding
619 surface (msf) is known as a transgressive surface (TS, Catuneanu, 2006), and its
620 identification is a key issue in sequence stratigraphy. Above this surface an
621 aggradational sequence starts, present here on the left-hand side of unit G2 in ERT 8
622 (Fig. 6), and progressing to the end of unit G1 in ERT 8 (Fig. 6).

623 In the southernmost sector of the depression, a clear paraconformity is
624 identified bringing resistive layers G1 and G2 into contact (ERT 1 and ERT 2). Here,
625 layer G2 displays an onlap contact with layer G3 (ERT 1 and ERT 2). A possible
626 explanation for this phenomenon is that tectonic subsidence facilitated the formation of
627 this angular discontinuity between G2 and G3, and at the same time preserved the
628 resistive layer G2 from erosion by G1. This interpretation is also supported by the fact
629 that the sedimentary fill in ERT 2 would have been conditioned by greater subsidence
630 on the western edge of the depression, forcing lateral accretion of the sigmoidal
631 clinofolds in this direction. The lateral accretion and correlative vertical onlap surfaces,
632 have no available space in ERT 8 and ERT 2, interpreted as a shallowing upward
633 sequence. This sequence occurs at the start of the ERT 8 erosive surface (US, Fig. 6)

634 which marks the end of the glacial obstruction in the ND. At that point alluvial fans
635 progress over the ND plain (Fig. 5). A shallowing-upward sequence may indicate an
636 accommodation lowering (Catuneanu, 2006), and thus a slight subsidence in the ND.

637

638 *4.5. Navamuño basin geometry and tectonic controls*

639

640 Taking into account the depth of the basement rock surface obtained in the
641 VES, ERT sections and MRS, the Navamuño basin infill thickness was calculated and
642 mapped (Fig. 9). These can be considered as minimum thickness values as the upper
643 limit of the basement was not reached in some zones and so they were assigned the
644 maximum penetration reached with the corresponding geophysical technique used.

645 The calculated sediment volume for the basin is approx. $3.8 \cdot 10^6$ m³, with a surface
646 area 129,694 m².

647 The isopach map shows a depocentre over 60 m deep in the south and centre
648 of the basin with a longitudinal NNE-SSW axis, parallel to the fractures defining the
649 western edge of the basin. The maximum thickness variation gradients are the W and
650 S borders, running NNE and ENE, respectively. These gradients, together with the
651 morphostructural map (Fig. 4) suggest a clear structural control of ND basin at both
652 edges by the NNE (PN Fault) and ENE (La Jara Fault) fracture families described in
653 Section 2.0, above. To the N the infill thickness decreases more gradually, while the
654 eastern boundary of the ND is more sharp (see onlap contacts in the right-hand side of
655 ERT 1 and ERT 8, Fig. 6), limited by the lateral moraine.

656 Considering the morphology of the sedimentary infill provided by the ERT
657 sections (Fig. 6, section 4.3), it was observed that unit G2 presents tilt in the centre of
658 the depression (ERT 2), while G1 presents sedimentary accommodation towards the
659 southern edge of the depression (ERT 7 and ERT 1). Geoelectrical layer G3 exhibits
660 clearly defined limits (in ERT 7 and ERT 1) and is clearly confined by the rock
661 substratum with structural limits in ERT 2 and ERT 8. All the above indicates a strong

662 tectonic component which configures the limits of the depression and affects its
663 sedimentary fill.

664

665 **5. Discussion**

666

667 The ND is one of the intermountain depressions forming the relief associated
668 with the Hervás-Candelario corridor-type valleys, one of the main morphostructures of
669 the W sector of the ICS. The evolution of these depressions is more complex than that
670 of the great sedimentary transpressional basins (De Vicente et al., 2011) and is
671 generally associated with NE-trending (NE-SW, NNE-SSW and N-S) strike-slip faults
672 (Santanach et al., 1988, 2005; Carrasco and Pedraza, 1991; Santanach, 1994;
673 Cabrera et al., 1996; Villamor et al., 1996; Alonso-Gavilán et al., 2004; Brum da
674 Silveira, et al., 2009). Two examples of this morphotectonic configuration are the Valle
675 del Jerte, 10 km to the east of the ND and linked to the AP fault (Carrasco and Pedraza
676 1991; Carrasco, 1997), and the series of depressions and platforms originating in the
677 NE trend of the HC and Galisteo strike-slip faults and their associated faults (Moreno,
678 1991), including the PN fault which is mainly responsible for the ND morphostructure
679 (Fig. 1).

680 Most of these ICS depressions occurring during the Paleogene /Lower Miocene,
681 correlative with the early stages of tectonic reactivation of present relief. In general, are
682 considered pull-apart type basins and in many cases aborted. Some of these were
683 reactivated during the Plio-Pleistocene and Quaternary, hosting new deposits which
684 present deformation structures catalogued as indicators of neotectonic activity (Brum
685 da Silveira, 1990; Carrasco et al., 1991; Capote et al., 1996; Villamor et al., 1996,
686 2012; De Vicente, 2009; De Vicente et al., 2011).

687 Geophysical data obtained from the ND show a relatively deep depression, with
688 sedimentary infill over 60 m thick. In the most surficial part of this fill (to depth 35 m) a
689 coarsening-upward sedimentary sequence is found corresponding to geoelectrical

690 layers G1 and G2, which from the available chronological data (Ruiz-Zapata et al.,
691 | 2011; Carrasco et al., 2015a; Turu et al., 20187a) corresponds to Upper Pleistocene
692 and Holocene deposits. At depths of 35-45 m, the permeability and water content
693 increase considerably, but lower down both decrease rapidly to low permeability and
694 low water content by depth 90 m.

695 From a genetic viewpoint, the deepest aquifer (below 45 m depth) should be
696 associated with characteristic joints in rock with a weathering front above a depth of 60
697 m. The intermediate aquifer (at depths of 35-45 m) is the most productive and
698 coincides with geoelectrical layer G3. This layer must be coarse grained to be so
699 permeable and may correspond to arkosic deposits similar to described in depressions
700 associated with the AP fault (Brum da Silveira, 1990; Capote et al., 1996; Villamor et
701 al., 1996, 2012). In agreement with this data, the ND is similar to other small ICS
702 depressions, which in genetic and evolutionary terms are associated with strike-slip
703 faults and which, in some cases, have been interpreted as pull-apart type basins (Brum
704 da Silveira, 1990; Carrasco and Pedraza, 1991; Capote et al., 1996; Villamor et al.,
705 1996, 2012; De Vicente, 2009; De Vicente et al., 2011). The difference between the ND
706 depression and these others is that the recent (Quaternary) sediments here are 30-35
707 m thick, compared with the 10-15 m obtained in other ICS intermountain depressions.
708 Another distinctive characteristic of the ND, is that its evolution was linked to that of the
709 Cuerpo de Hombre glacier during the Glacial Period in this area (Upper Pleistocene;
710 ~MIS2), and the depression remained obstructed by moraines (and possibly by ice
711 during the Maximum Ice Extent, MIE) during the stages of glaciación.

712 In this context, both the subsidence dynamics and glacial-damming should be
713 considered determining factors in the recent infill process of the ND. Although the data
714 available from direct soundings is limited to the first 16 m of sediments (Carrasco et al.,
715 | 2015a, Turu et al., 20187a), the chrono-evolutionary data obtained from the study of
716 the Cuerpo de Hombre paleoglacier (Carrasco et al., 2015b; Fig. 2) enable a
717 chronological succession to be established for how this depression evolved throughout

718 the Upper Pleistocene. The basin hydrologic regime was initially exorheic (drained by
719 the Cuerpo de Hombre river) and was later obstructed by the glacier. The obstruction
720 process started as ice-damming during the expansion stage of the glacier towards its
721 MIE (dated to 25.0 ± 1.3 ka; Carrasco et al., 2015b). Later, between 20.6 ± 2.5 ka and
722 17.8 ± 1.0 ka, the glacier built a wall-shaped lateral moraine (morainic Peripheral
723 Deposits and Principal Moraine from Carrasco et al., 2015b; PD-M and PM,
724 respectively, Figs. 2A, 2C) and blocked the eastern boundary of ND. This
725 interpretation is based on an existing layer of alluvial fan deposits observed by
726 Carrasco et al. (2015a) and Turu et al. (20187a). The age obtained for the bottom of
727 the peatland above the alluvial fan deposits is mid-Holocene (5160 ± 40 cal. yr BP,
728 sample from 4.5 m depth, Ruiz-Zapata et al., 2011).

729 The path of the Cuerpo de Hombre glacier was carefully considered to explain
730 the obstruction process. The current morphology of the Cuerpo de Hombre
731 paleoglacier displays a confined valley between the two major lateral moraines (PM
732 formations; Carrasco et al., 2015b). The right lateral moraine is attached to the bedrock
733 slopes and displays a constant NW-SE direction throughout its upper and middle
734 sector. The left lateral moraine also presents those same characteristics in its upper
735 sector. However, its middle sector changes markedly. From the area where the
736 moraine connects with the southern end of the ND, it is no longer confined in the
737 bedrock relief, and runs in a NNW-SSE direction turning after to NNE-SSW parallel to
738 PN fault (Figs. 2A, 4). These changes are maintained to the northern edge of the ND,
739 giving rise to the wall-shaped lateral moraine relief which forms the boundary between
740 the paleoglacier valley and the ND (Figs. 2A, 2C).

741 To explain the causes of this process, and most importantly, why the ice did not
742 expand on to the ND plain during the advance stage towards its glacial maximum,
743 three hypotheses can be established: (1) that the glacier in this zone was already in a
744 reach with non-expansive stagnant flow; (2) that there was an ice flow process adapted
745 to the morphological directives of a pre-glacial entrenched valley; and (3) that the ice

746 flow was conditioned by the tectonic structure of the depression and its neotectonic
747 evolution.

748 For the first hypothesis (1), from the data of this paleoglacier reconstruction
749 during its Maximum Ice Extent (MIE) provided by Carrasco et al. (2015b) and revised
750 and completed in this new research, the following can be established: (i) that the zone
751 connecting the glacier and the ND plain starts at altitude 1600 m asl, at a distance of
752 1.7 km from the Equilibrium-Line Altitude (ELA, estimated at altitude 1966 m asl), and
753 at 1.9 km from the glacier terminus which then was located at altitude 1260 m asl; and
754 (ii) that the thickness of the glacial tongue ice in this reach was 50 m, much thicker than
755 the ice in the stagnation zones close to glacier terminus or snout (with thickness 10-15
756 m). According to this data, the glacier tongue in this confluence zone was advancing in
757 its middle-upper reach, and could have expanded on to the ND plain.

758 For the second hypothesis (2) and according to surface geomorphological data,
759 there are no indicators of an existing pre-glacial entrenched valley which would have
760 channelled the ice. The valley of the Cuerpo de Hombre paleoglacier and the ND are
761 separated by the left lateral moraine of the PM formation, which originated a wall-
762 shaped lateral moraine accumulating directly on both plains (Figs. 2A, 2C). In the reach
763 where the paleoglacial valley and the ND appear connected, the plain of the ancient
764 glacier bed (defined on the bedrock or with a thin layer of subglacial sediments of less
765 than 2 m) and the ND plain are located at similar altitudes, presenting a gentle slope
766 from the former to the latter (1585-1520 m asl and 1520-1480 m asl; maximum and
767 minimum altitudes of the glacial valley bottom and the depression plain, respectively).
768 A possible interpretation is therefore that in the pre-glacial stage both plains formed a
769 single unit, later divided by the lateral moraine. Given the gradient between the two
770 plains, in the glacier advance stages towards its maximum (MIE), previous to the
771 development of the moraine (established from a first post-MIE retreat of the glacier,
772 Carrasco et al., 2015b), the ice would have expanded towards the ND.

773 | For the third hypothesis (3) and given that ND is associated with multiple faults,
774 | there is a solidly based argument for the existence of a tectonic structure in the relief
775 | (hypothesis 3) which conditioned the path of the glacial tongue.

776 | Many studies have highlighted the impact of tectonic activity on the shape,
777 | location and path of glaciers, but also their capacity for adapting to tectonic structures
778 | (Clark, 1967, 1972; Clark et al., 2003; Gillespie and Clark, 2011; Glasser and Ghiglione
779 | 2009; Cotton et al., 2014; Bathrellos et al., 2017). In studies of ICS glacial morphology
780 | carried out to date (see here Pedraza and Carrasco, 2006), the general theory is that
781 | the glacial basins occupied structurally controlled pre-glacial river valleys, but indicators
782 | of the impact of tectonic structures or neotectonic activity on glacier dynamics have not
783 | been detected. By interpreting the data obtained from near surface geophysical
784 | research in ND, it can be deduced that the left lateral moraine of the Cuerpo de
785 | Hombre paleoglacier fossilized a small raised block which may initially have acted as
786 | the boundary between the glacier and the ND (Fig 8). In addition, and as previously
787 | described, in the sedimentary infill a series of structures is also detected which may be
788 | associated with neotectonic readjustment fault processes. According to these data,
789 | the evolutive sequence of ND, and the effect of these processes on the path of the
790 | Cuerpo de Hombre glacier, can be established as detailed below.

791 | The depression obstruction process may have already been initiated by the
792 | glacier tongue during its expansion phase towards the maximum extent (MIE) and was
793 | later consolidated by the moraines. In this context, still supposing that the
794 | sedimentation rate in the obstructed cuvette was very low or nil during the glacial
795 | phase and the majority of the sediments detected by geophysics were all pre-glacial,
796 | the 16 m of sediments of post-glacier fill detected with direct test bores (Carrasco et al.,
797 | 2015a; Turu et al., 20187a) imply the elevation of the depression plain which: (1) must
798 | have fossilized almost completely the formation of dispersed erratic boulders (PD-B;
799 | Carrasco et al., 2015b, Fig. 2C); and (2) reveals that the base of the depression at the
800 | onset of the glacial stage was some 15-30 m (extreme north and south, respectively)

801 lower than the floor of the glacial valley. Therefore, there was evidently a sufficient
802 longitudinal gradient of the terrain for the glacier to maintain its trajectory according to
803 the line of minimum slope. However, and as has been shown, after a slight advance
804 towards the depression, the glacier made an abrupt turn and came to a standstill at its
805 margin.

806 According to these data, it can be established that: (1) at that point the
807 configuration of the relief on the bottom of the depression must have been very
808 different and acted as a threshold controlling the direction of the ice flow; and (2) given
809 that the present base of the depression is at lower elevations than the floor of the
810 glacial valley and hosts the sediments corresponding to the obstruction process, the
811 only possible explanation for this process is the sinking of the depression during these
812 infill phases.

813 In relation to this sinking of the sedimentary depression, the suggestions are
814 that it was caused by gravitational movements (rotation platform) or by differential
815 movements between blocks limited by faults (tectonic readjustments). Both the data
816 provided by geophysics and the regional context data are sufficient arguments to
817 consider that the most probable process was the latter. The onlap contact shown in
818 geoelectrical layer G2 in ERT 1, and geoelectrical layer G1 in ERT 7, are indicators of
819 syntectonic sedimentation in ND (Fig. 6). The same occurs with geoelectrical layer G3
820 (ERT 1, ERT 3 and ERT 7) which is limited by high dip faults in ERT 2 and ERT 8 (Fig.
821 6). This rock threshold where the lateral moraine of the Cuerpo de Hombre
822 paleoglacier is found, corresponds to a raised block, and would have acted as a limit to
823 the path of the ice.

824 On the other hand, although the ICS and the centre of the Iberian Peninsula are
825 classified as zones of very low to moderate seismicity, (IGN, 2016), from analysing the
826 current river network of the ICS and other related areas in the central Iberian Meseta,
827 multiple indicators emerge of structural control, and of recent and current impact of
828 neotectonics with paleoseismic structures originating throughout the Pleistocene

829 (Pedraza, 1976; Carrasco et al., 1991; Silva et al., 1988; Pol et al., 1989; De Vicente et
830 al., 2007, 2011; Garzón et al., 2014). In this context, the proposed model for the route
831 followed by the paleoglacier can be considered coherent.

832

833 **6. Conclusions**

834

835 | The ND is a ~30 ha pseudo-endorheic flat basin over granitic bedrock with
836 | water ponding associated with the PN fault, a NNE-SSW trending Variscan strike-slip
837 | fault –correlated with the series of strike-slip faults described along the ICS. In the
838 | geomorphological and geophysical studies carried out in this research, ~~has been~~
839 | ~~detected~~ a sedimentary infill over 60 m thick has been proven. This agrees with ~~to that~~
840 | established in recent previous investigations and allows us to catalog the ND as the
841 | largest and deepest ~~str~~ sedimentary basin of the ICS associated with glacial processes
842 | (glacier obstruction or overdeepening).

843 | Geophysical surveys have been ~~critical determinant~~ in identifying the infill depth
844 | in the depression and the geometrical relationships existing in the rock substrata. This
845 | information, together with that provided by the surficial geology and geomorphology,
846 | supports the hypothesis that: (1) ND can be correlated with the small sedimentary
847 | basins located along the Variscan strike-faults described in the Iberian Massif and
848 | classified as an intermountain tectonic basin with primary origin due to a transtensional
849 | process in the PN strike-slip fault during the stages of reactivation of the ICS
850 | (Oligocene-lower Miocene); (2) part of the sedimentary infill is related to the
851 | contribution made at the time by the Cuerpo de Hombre glacier meltwater through a
852 | system of marginal flows; and (3) both in the path of the glacier and in the sedimentary
853 | infill of the ND correlative to the glacial and postglacial stages, we have detected
854 | indicators of neotectonic activity.

855 | The Cuerpo de Hombre paleoglacier had a marked influence on sedimentary
856 | evolution in the ND, as it was responsible for the shift from an exorheic hydrologic

857 regime to a semi-endorheic regime with ponding. From the available data, this process
858 took place during the maximum glacial advance stage (approx. 25.0 ± 1.3 ka BP) and
859 continued at least until silting-up occurred during the Holocene. Neotectonic
860 readjustment has continued from the last glacial cycle to the present day. However, the
861 post-glacial sedimentary infill in the depression presents a shallowing-upward
862 sequence, which is considered an indicator of decreasing subsidence.

863

864 **Acknowledgements**

865

866 This work was supported by the Spanish Ministry of Economy and Competitiveness
867 (Projects CGL2013-44076-P and CGL2016-78380-P). The authors also wish to
868 acknowledge the help and assistance of the Regional Environment Department (JCyL)
869 and the Local Authority in the village of Candelario. We also thank to the Editor and the
870 reviewers, for their helpful comments and constructive suggestions that greatly
871 improved this manuscript.

872

873 **References**

874

- 875 Abel-Schaad, D., Pulido, F., López-Sáez, J.A., Alba Sánchez, F., Nieto Lugilde, D.,
876 Franco Múgica, F., Pérez-Díaz, S., Ruiz Zapata, M.B., Gil García, M.J., Dorado
877 Valiño, M., 2014. Persistence of tree relicts in the Spanish Central System
878 through the Holocene. *Lazaroa* 35, 107-131.
- 879 Alonso-Gavilán, G., Armenteros, I., Carballeira, J., Corrochano, A., Huerta, P.,
880 Rodríguez, J. M., 2004. Cuencas cenozoicas del Macizo Ibérico. In: Vera, J.A.
881 (Ed.), *Geología de España*. SGE-IGME. Madrid, Spain, pp. 581-584.
- 882 Anon, 1977. The description of rock masses for engineering purposes: Report by the
883 Geological Society Engineering Group Working Party. *Q. J. Eng. Geol.*
884 *Hydrogeol.* 10, 355-388.

885 Barker, R., 1992. A simple algorithm for electrical imaging of the subsurface. First
886 Break 10, 53 – 62.

887 Bathrellos, G., Skilodimou, H., Maroukian, H., 2017. The significance of tectonism in
888 the glaciations of Greece. Geological Society, London, Special Publications
889 433, 237-250.

890 Behroozmand, A.A., Keating, K., Auken, E., 2015. A Review of the Principles and
891 Applications of the NMR Technique for Near-Surface Characterization. Surv.
892 Geophys. 36, 27-85.

893 Bellido-Mulas, F. (Ed.), 2006. Mapa Geológico de Cabezuela del Valle, 1:50 000. Map
894 576. Instituto Geológico y Minero de España. Madrid, Spain. <http://www.igme.es>

895 Ber, A., 2009. Vertical stress of the pleistocene continental glaciers and its hypothetical
896 evidence in present relief of Northern Europe. Polish Geol. Inst. Spec. Pap. 25,
897 7–12.

898 Bhattacharya, P.K., Patra, H.P. (Eds.), 1968. Direct current geoelectric sounding,
899 principles and interpretation. Elsevier, Amsterdam, Netherlands.

900 Bobachev, A.A, Shevnin, V.A., Modin, I.N., 2003. IPI2WIN version 3.0.1e. <http://geophys.geol.msu.ru/ipi2win.htm>.

901

902 Bordonau, J., 1992. Els Complexos glàcio-lacustres relacionats amb el darrer cicle
903 glacial als Pirineus. Ph.D. Thesis, Barcelona Univ., Spain.

904 Brum da Silveira, A., 1990. Neotectónica e Sismotectónica da Região Vidigueira–
905 Moura. Ph.D. Thesis, Univ. Lisboa, Portugal.

906 Brum da Silveira, A., Cabral, J., Perea, H., Ribeiro, A., 2009. Evidence for coupled
907 reverse and normal active faulting in W Iberia. The Vidigueira-Moura and
908 Alqueva faults (SE Portugal). Tectonophysics 474, 184–199.

909 Cabral, J., 1995. Neotectónica em Portugal Continental. Memórias do Instituto
910 Geológico e Mineiro 31, Lisboa, Portugal.

911 Cabral, J., 2012. Neotectonics of mainland Portugal: state of the art and future
912 perspectives. J. Iber. Geol. 38, 71–84.

913 Cabrera, L., Ferrús, B., Sáez, A., Santanach P., Bacelar J., 1996. Onshore Cenozoic
914 strike-slip basins in NW Spain. In: Friend, P. F., Dabrio, C.J. (Eds), Tertiary
915 Basins of Spain. Cambridge Univ. Press, New York, USA, pp. 247-254.

916 Capote, R., Villamor, P., Tsige, M., 1996. La tectónica alpina de la Falla de Alentejo-
917 Plasencia (Macizo Hespérico). *Geogaceta* 20, 921–924.

918 Carrasco, R.M., 1997. Estudio Geomorfológico del Valle del Jerte (Sistema Central
919 Español): secuencia de procesos y dinámica morfogenética actual. Ph.D.
920 Thesis, Complutense Univ. Madrid, Spain.

921 Carrasco, R.M., Pedraza, J., 1991. Historia morfodinámica de la Falla de Plasencia en
922 el Valle del Jerte. In: Actas de Gredos, V Jornadas de Verano de La Sierra de
923 Gredos, Boletín Universitario 11, UNED, Ávila, Spain, pp. 17–30.

924 Carrasco, R.M., Pedraza, J., Rubio, J.C., 1991. Actividad neotectónica cuaternaria en
925 el Valle del Jerte. *Cuaternario y Geomorfología* 5, 15–25.

926 Carrasco, R.M., Pedraza, J., Domínguez-Villar, D., Willebring, J., Razola, L.,
927 Edwards, L., Wang, Y., Fairchild, I.J., Baker, A., Ruiz-Zapata, M.B., Centeno, J.,
928 2009. Chronology and causes of the Last Glacial Maximum in Spanish Central
929 System: the project methodology. 7th International Conference on
930 Geomorphology (ANZIAG). Conference Abstracts, Melbourne, Australia.

931 Carrasco, R.M., Pedraza, J., Domínguez-Villar, D., Villa, J., Willenbring, J.K., 2013.
932 The plateau glacier in the Sierra de Béjar (Iberian Central System) during its
933 maximum extent. Reconstruction and chronology. *Geomorphology* 196, 83–93.

934 Carrasco, R.M., Sánchez, J., Muñoz-Martín, A., Pedraza, J., Olaiz, A.J., Ruiz-Zapata,
935 B., Abel-Schaad, D., Merlo, O., Domínguez-Villar, D., 2015a. Caracterización
936 de la geometría de la depresión de Navamuño (Sistema Central Español)
937 aplicando técnicas geofísicas. *Geogaceta* 57, 39–42.

938 Carrasco, R.M., Pedraza, J., Domínguez-Villar, D., Willenbring, J.K., Villa, J., 2015b.
939 Sequence and chronology of the Cuerpo de Hombre paleoglacier (Iberian
940 Central System) during the last glacial cycle. *Quat. Sci. Rev.* 129, 163–177.

941 Catuneanu, O., 2006. Principles of Sequence Stratigraphy. Elsevier Science,
942 Amsterdam, Netherlands.

943 Centeno, J.D., Brell, J.M., 1987. Características de las alteraciones de las Sierras de
944 Guadarrama y Malagon (Sistema Central Español). Cuaderno Lab. Xeológico
945 de Laxe 12, 79-87.

946 Clark, M.M., 1967. Pleistocene glaciation of the drainage of the West Walker River,
947 Sierra Nevada, California. Ph.D. Dissertation, Stanford, Stanford University,
948 USA.

949 Clark, M.M., 1972. Range-front faulting: cause of anomalous relationships among
950 moraines of the eastern slope of the Sierra Nevada, California. Geol. Soc. Am.
951 Abstr. Programs 4, 137.

952 Clark, D., Gillespie, A.R., Clark, M.M., Burke, R.M., 2003. Mountain glaciations of the
953 Sierra Nevada. In: Easterbrook, D.J. (Ed.), Quaternary Geology of the United
954 States. International Quaternary Association: INQUA 2003. Field Guide Volume.
955 XVI INQUA Congress. Desert Research Institute, Reno, USA, pp. 287–312.

956 Cotton, M.M., Bruhn, R.L., Sauber, J., Burgess, E., Forster, R.R., 2014. Ice surface
957 morphology and flow on Malaspina Glacier, Alaska: Implications for regional
958 tectonics in the Saint Elias orogen. Tectonics 33, 558–595.

959 Dearman, W.R., 1978. Weathering classification in the characterization of rock: a
960 revision. Bull. Int. Assoc. Eng. Geol. 18, 123–128.

961 De Brujne, C.H., Andriessen, P.A.M., 2002. Far field effects of Alpine plate tectonism in
962 the Iberian microplate recorded by faultrelated denudation in the Spanish
963 central system. Tectonophysics 349,161-184.

964 Descloitres, M., Ruiz, L., Sekhar, M., Legchenko, A., Braun, J.J., Mohan Kumar, M.S.,
965 Subramanian, S., 2008. Characterization of seasonal local recharge using
966 electrical resistivity tomography and magnetic resonance sounding. Hydrol.
967 Process. 22, 384–394.

968 De Vicente, G., 2009. Partición de la deformación cenozoica intraplaca en el Sistema
969 Central. *Geogaceta* 46, 23-26.

970 De Vicente, G., Vegas, R., 2009. Large-scale distributed deformation controlled
971 topography along the western Africa–Eurasia limit: tectonic constraints.
972 *Tectonophysics* 474, 124-143.

973 De Vicente, G., Vegas, R., Muñoz Martín, A., Silva, P.G., Andriessen, P., Cloetingh, S.,
974 González Casado, J.M., Van Wees, J.D., Álvarez, J., Carbó, A., Olaiz, A., 2007.
975 Cenozoic thick-skinned deformation and topography evolution of the Spanish
976 Central System. *Glob. Planet. Change* 58, 335–381.

977 De Vicente, G., Cloetingh, S., Van Wees, J.D., Cunha, P.P., 2011. Tectonic
978 classification of Cenozoic Iberian foreland basins. *Tectonophysics* 502, 38–61.

979 Foroutan, M., Vilanova, S., Heleno, S., Pinto, L., Far, A.S., Falcao-Flor, A., Canora, C.,
980 Pina, P., Vieira, G., Fonseca, J., 2016. New evidence for large earthquakes in
981 mainland Portugal: paleoseismology of the Lower Tagus Valley fault. 35th
982 General Assembly of the European Seismological Commission. ESC2016-489-
983 1.

984 Franco-Múgica, F., 1995. Estudio palinológico de turberas holocenas en el Sistema
985 Central: reconstrucción paisajística y acción antrópica. Ph.D. Thesis, Univ.
986 Autónoma. Madrid, Spain.

987 Garate, J., Martin-Davila, J., Khazaradze, G., Echeverria, A., Asensio, E., Gil, A.J., de
988 Lacy, M.C., Armenteros, J.A., Ruiz, A.M., Gallastegui, J., Alvarez-Lobato, F.,
989 Ayala, C., Rodríguez-Caderot, G., Galindo-Zaldívar, J., Rimi, A., Harnafi, M.,
990 2015. Topo-Iberia project: CGPS crustal velocity field in the Iberian Peninsula
991 and Morocco. *GPS Solutions*, 19, 287-295.

992 Garzón, G., Garrote, J., Tejero, R., 2014. La integración de la red fluvial del margen
993 norte del río Tajo. El papel de las depresiones cenozoicas. In: Schnabel, S.,
994 Gómez-Gutiérrez, A. (Eds.), *Avances de la Geomorfología en España 2012-*
995 *2014*. Universidad de Extremadura, SEG, Cáceres, Spain, pp. 393-396.

- 996 Génova, M., Gómez-Manzanaque, F., Martínez-García, F., Postigo-Mijarra, J.M., 2016.
997 Early Holocene vegetation in the Ayllón Massif (Central System Range, Spain)
998 based on macroremains. A paleoecological approach. *Palaeogeogr.*
999 *Palaeoclimatol. Palaeoecol.* 441, 811–822.
- 1000 Gillespie, A.R., Clark, D.H., 2011. Glaciations of the Sierra Nevada, California, USA. In:
1001 Ehlers, J., Gibbard, P.L., Hugges, P.D. (Eds.), *Quaternary Glaciations – Extent*
1002 *and Chronology*. Elsevier, Amsterdam, Netherlands, pp. 447-462.
- 1003 Glasser, N.F., Ghiglione, M.C., 2009. Structural, tectonic and glaciological controls on
1004 the evolution of fjord landscapes. *Geomorphology* 105, 291–302.
- 1005 Grunewald, E., Knight, R., 2011. The effect of pore size and magnetic susceptibility on
1006 the surface NMR relaxation parameter T_2^* . *Near Surface Geophysics* 9, 169-
1007 178.
- 1008 Hausmann, J., Steinell, H., Kreck, M., Werban, U., Vienken, T., Dietrich, P., 2013. Two-
1009 dimensional geomorphological characterization of a filled abandoned meander
1010 using geophysical methods and soil sampling. *Geomorphology* 201, 335–343.
- 1011 Herrero-Simón, R., 2003. Anasim code V.6.0; Internal software from the Nuclear and
1012 Physics Engineering Department of the Universitat Politècnica de Catalunya
1013 (UPC), Terrassa, Spain.
- 1014 Herrero-Simón, R., 2007. Simusism code V.2.0; Internal software from the Nuclear and
1015 Physics Engineering Department of the Universitat Politècnica de Catalunya
1016 (UPC), Terrassa, Spain.
- 1017 Hertrich, M., 2008. Imaging of groundwater with nuclear magnetic resonance. *Prog.*
1018 *Nucl. Magn. Reson. Spectrosc.* 53, 227–248.
- 1019 IGN, 2016. Mapas de sismicidad y peligrosidad. Instituto Geográfico Nacional, Spain.
1020 <http://www.ign.es>
- 1021 Jalut, G., Turu, V., Dedoubat, J.J., Otto, T., Ezquerro, J., Fontugne, M., Belet, J.M.,
1022 Bonnet, L., de Celis, A.G., Redondo-Vega, J.M., Vidal-Romaní, J.R., Santos, L.,
1023 2010. *Palaeoenvironmental studies in NW Iberia (Cantabrian range): Vegetation*

Formatted: Spanish (Spain,
International Sort)

1024 history and synthetic approach of the last deglaciation phases in the western
1025 Mediterranean. *Palaeogeogr. Palaeoclimatol. Palaeoecol.* 297, 330–350.

1026 Lange, G., Yaramanci, U., Meyer, R., 2007. Surface Nuclear Magnetic Resonance. In:
1027 Knödel, K., Lange, G., Voigt, HJ. (Eds.), *Environmental Geology*. Springer
1028 Berlin Heidelberg, Germany, pp. 403–430.

1029 Legchenko, A.V., Shushakov, O.A., 1998. Inversion of surface NMR data. *Geophysics*,
1030 63 (1), 75-84.

1031 Loke, M.H., Barker, R.D., 1996. Rapid least-squares inversion of apparent resistivity
1032 pseudosections by a quasi-Newton method. *Geophys. Prospect.* 44, 131-152.

1033 Loke, M.H., Wilkinson, P.B, Chambers, J.E., 2010. Parallel computation of optimized
1034 arrays for 2-D electrical imaging surveys. *Geophys. J. Int.* 183, 1302-1315.

1035 López-Sáez, J.A., Abel-Schaad, D., Pérez-Díaz, S., Blanco-González, A., Alba-
1036 Sánchez, F., Dorado, M., Ruiz-Zapata, B., Gil-García, M.J., Gómez-González,
1037 C., Franco-Múgica, F., 2014. Vegetation history, climate and human impact in
1038 the Spanish Central System over the last 9000 years. *Quat. Int.* 353, 98–122.

1039 López-Sáez, J.A., Abel-Schaad, D., Robles-López, S., Pérez-Díaz, S., Alba-Sánchez,
1040 F., Nieto-Lugilde, D., 2016. Landscape dynamics and human impact on high-
1041 mountain woodlands in the western Spanish Central System during the last
1042 three millennia. *JASREP* 9, 203–218.

1043 Maillet, R., 1947. The fundamental equations of electrical prospecting. *Geophysics* 12,
1044 529-556.

1045 Mejías, M., Plata, J., 2007. General concepts in Hydrogeology and Geophysics related
1046 to MRS. *Bol. Geol. y Min.* 118, 423–440.

1047 Mendes-Victor, L., Oliveira, C.S., Azevedo, J., Ribeiro, A. (Eds.), 2009. *The 1755*
1048 *Lisbon Earthquake: Revisited*. Springer, Netherlands.

1049 Molina-Ballesteros, E., García-González, M.T., Espejo, R., 1991. Study of
1050 Paleoweathering on the Spanish Hercynian basement Montes de Toledo
1051 (Central Spain). *Catena* 18, 345-354.

Formatted: English (United Kingdom)

- 1052 Molina-Ballesteros, E., García-Talegón, J., Vicente-Hernández, M. A., 1994. Las
1053 paleoalteraciones sobre el zócalo hercínico ibérico. Aproximación a una
1054 interpretación regional a partir de perfiles españoles. Cuaderno Lab. Xeológico
1055 de Laxe 19, 261-271.
- 1056 Molina-Ballesteros, E., García-Talegón, J., Vicente-Hernández, M.A., 1997.
1057 Palaeoweathering profiles developed on the Iberian Hercynian Basement and
1058 their relationship to the oldest Tertiary surface in central and western Spain.
1059 Geol. Soc. London, Spec. Publ. 120, 175–185.
- 1060 Moreno, F., 1991. Superficies de erosión y tectónica neógena en el extremo occidental
1061 del Sistema Central español. Geogaceta 9, 47-50.
- 1062 Muñoz Martín, A., De Vicente, G., Olaiz, A., Antón, L., Vegas, R., Granja, J.L., 2012.
1063 Mapa de esfuerzos activos en línea de la Península Ibérica a partir de
1064 Mecanismos Focales calculados desde el Tensor de Momento Sísmico.
1065 Geotemas 13, 1-4.
- 1066 Olaiz, A.J., Muñoz-Martín, A., De Vicente, G. Vegas, R., Cloeting, S., 2009. Oblique
1067 strain partitioning and transpression on an inverted rift: The Castilian Branch of
1068 the Iberian Chain. Tectonophysics 470, 224-242.
- 1069 Olvmo, M., Johansson, M., 2002. The significance of rock structure, lithology and pre-
1070 glacial deep weathering for the shape of intermediate-scale glacial erosional
1071 landforms. [Earth Surf. Process. Landforms 27, 251–268.](#)
- 1072 Palmer, D., 1980. The generalized reciprocal method of seismic refraction
1073 interpretation. [Society of Exploration Geophysicists, Tulsa, USA.](#)
- 1074 Pedraza, J., 1976. Algunos procesos morfogenéticos recientes en el valle del río
1075 Alberche (Sistema Central Español). La depresión de Aldea del Fresno-
1076 Almorox. Bol. Geol. y Min. 87, 1–12.
- 1077 Pedraza, J., 1994. Sistema Central. In: Gutiérrez Elorza, M. (Ed.), Geomorfología de
1078 España. Rueda, Spain, pp. 63–100.

Formatted: English (United Kingdom)

Formatted: Spanish (Spain, International Sort)

1079 Pedraza, J., 2012. Late Pleistocene glacial evolutionary stages in the Spanish Central
1080 System. *Quat. Int.* 279–280, 371–372.

Formatted: Spanish (Spain, International Sort)

1081 Pedraza, J., Carrasco, R. M., 2006, El glaciario pleistoceno del Sistema Central.
1082 *AEPECT*, 13 (3), 278-288.

Formatted: Spanish (Spain, International Sort)

1083 Pedraza, J., Carrasco, R.M., Domínguez-Villar, D., Villa, J., 2013. Late Pleistocene
1084 glacial evolutionary stages in the Gredos Mountains (Iberian Central System).
1085 *Quat. Int.* 302, 88–100.

1086 Pèlachs, A., Julià, R., Pérez-Obiol, R., Burjachs, F., Expósito, I., Yll, R., Vizcaino, A.,
1087 Turu, V., Soriano, J.M., 2011. Dades paleoambientals del complex
1088 glaciolacustre de l'estany de Burg durant el Tardiglacial (Vall Ferrera, Pallars
1089 Sobirà). In: Turu, V. and Constante, A. (Eds.), *Simposio de Glaciario: El*
1090 *Cuaternario en España y áreas afines, Avances en 2011*. Fundació Marcel
1091 *Chevalier- AEQUA*. Andorra la Vella, pp. 40–50.

1092 Pellicer, X.M., Zarroca, M., Gibson, P., 2012. Time-lapse resistivity analysis of
1093 Quaternary sediments in the Midlands of Ireland. *J. Appl. Geophys.* 82, 46–58.

Formatted: English (United Kingdom)

1094 Plata, J.L., Rubio, F.M., 2008. The use of MRS in the determination of hydraulic
1095 transmissivity: The case of alluvial aquifers. *J. Appl. Geophys.* 66, 128–139.

Formatted: Spanish (Spain, International Sort)

1096 Pol, C., Sánchez del Corral, A., Carballeira, J., 1989. Neotectónica en la cuenca del
1097 alto Tormes (Sistema Central, Ávila): Influencia en la morfología fluvial.
1098 *Geogaceta* 6, 90–94.

1099 Prasicek, G., Larsen, I.J., Montgomery, D.R., 2015. Tectonic control on the persistence
1100 of glacially sculpted topography. *Nat. Commun.* 6, 8028.

1101 Reynolds, J.M., 2011. *An Introduction to Applied and Environmental Geophysics*.
1102 Wiley-Blackwell, Chichester, UK.

1103 Rodríguez Fernández, L.R.; Oliveira, J.T. (Ed.), 2015. *Mapa Geológico de la Península*
1104 *Ibérica, Baleares y Canarias a escala 1:1.000.000*. Instituto Geológico y Minero
1105 de España. Madrid, Spain. <http://www.igme.es>

Formatted: Spanish (Spain, International Sort)

Field Code Changed

Formatted: Spanish (Spain, International Sort)

Formatted: Spanish (Spain, International Sort)

- 1106 Rubiales, J.M., García-Amorena, I., Génova, M., Gómez Manzaneque, F., Morla, C.,
1107 2007. The Holocene history of highland pine forests in a submediterranean
1108 mountain: the case of Gredos mountain range (Iberian Central range, Spain).
1109 Quat. Sci. Rev. 26, 1759–1770.
- 1110 Rubio, J.C., 1990. Geomorfología y Cuaternario de las sierras de la Nava y Béjar
1111 (Sistema Central Español). PhD Thesis, Complutense Univ., Madrid, Spain.
- 1112 Ruiz-Zapata, M.B., Carrasco, R.M., Gil-García, M.J., Pedraza, J., Razola, L.,
1113 Domínguez- Villar, D., Gallardo, J.L., 2011. Dinámica de la vegetación durante
1114 el Holoceno en la Sierra de Gredos (Sistema Central Español). *Bol. R. Soc.*
1115 *Esp. Hist. Nat.* 105, 109-123.
- 1116 Salazar-Rincón, A., Mata-Campo, P., Rico-Herrero, M.T., Valero-Garcés, B.L., Oliva-
1117 Urcia, B., Ibarra, P., Rubio, F.M., 2013. El paleolago de La Larri (Valle de
1118 Pineta, Pirineos): Significado en el contexto del último máximo glaciar en el
1119 Pirineo. *Cuadernos de Investigación Geográfica* 39, 97-116.
- 1120 Santanach, P., 1994. Las cuencas terciarias gallegas en la terminación occidental de
1121 los relieves pirenaicos. *Cuad. Lab. Xeol. Laxe* 19, 57-71.
- 1122 Santanach, P., Baltuille, J.M., Cabrera, L., Monge, C., Sáez, A., Vidal-Romaní, J.R.
1123 1988. Cuencas terciarias gallegas relacionadas con corredores de falla
1124 direccionales. II Congreso Geológico de España, IGME, Granada, Spain, pp.
1125 123-133.
- 1126 Santanach, P, Ferrús, B., Cabrera, L., Sáez, A., 2005. Origin of a restraining bend in
1127 an evolving strike-slip system: The Cenozoic As Pontes basin (NW Spain).
1128 *Geol. Acta* 3, 225–239.
- 1129 Sanz-Donaire, J.J., 1979. El Corredor de Béjar. Instituto de Geografía aplicada. CSIC,
1130 Madrid, Spain.
- 1131 Schrott, L., Hördt, A., Dikau, R. (Eds.), 2003. Geophysical applications in
1132 geomorphology. *Zeitschr. f. Geomorphologie Supplementbände*, 132, 190S.

Formatted: Spanish (Spain,
International Sort)

Formatted: Spanish (Spain,
International Sort)

- 1133 Sheehan J.R., Doll W.E., Mandell W.A., 2005. An evaluation of methods and available
1134 software for seismic refraction tomography analysis. J. Environ. Eng.
1135 Geophysics. 10, 21–34.
- 1136 Sheriff, E.R., Geldart, L.P., 1991. Exploración sísmológica. Volumen II. Procedimientos
1137 e interpretación de datos. Limusa, México.
- 1138 Shushakov, O.A., Legchenko, A.V., 1994. Groundwater proton magnetic resonance in
1139 the horizontally stratified media of different electrical conductivity ~~(in Russian).~~
1140 Geol. Geophys. 35, 130-136. (in Russian).
- 1141 Silva, P., Goy, J.L., Zazo, C., 1988. Evolución Geomorfológica de la confluencia de los
1142 ríos Jarama y Tajuña durante el cuaternario (Cuenca de Madrid, España).
1143 Cuaternario y Geomorfología 2, 125–133.
- 1144 Turu, V., 1999. Aplicación de diferentes técnicas geofísicas y geomecánicas para el
1145 diseño de una prospección hidrogeológica de la cubeta de Andorra, (Pirineo
1146 Oriental): implicaciones paleohidrogeológicas en el contexto glacial andorrano.
1147 In: Actualidad de las técnicas geofísicas aplicadas en hidrogeología. ITGE-
1148 IGME, Madrid, Spain, pp. 203-210.
- 1149 Turu, V., 2012. Surface NMR survey on Hansbreen Glacier, Hornsund, SW
1150 Spitsbergen. Landform Analysis 21, 57-74.
- 1151 Turu, V., Boulton G. S., Ros X., Peña-Monne J. L., Marti-Bono C., Bordonau J.,
1152 Serrano-Cañadas E., Sancho-Marcén, C., Constante-Orrios A., Pous J.,
1153 Gonzalez-Trueba J. J., Palomar J., Herrero-Simón, R., García-Ruiz, J. M.,
1154 2007. Structure des grands bassins glaciaires dans le nord de la Péninsule
1155 Ibérique: comparaison entre les vallées d’Andorre (Pyrénées Orientales), du
1156 Gállego (Pyrénées Centrales) et du Trueba (Chaîne Cantabrique). Quaternaire
1157 18, 309–325.
- 1158 Turu, V., Ventura, J., Ros, X., Pélachs, A., Vizcaino, A., Soriano, J.M., 2011.
1159 Geomorfologia glacial del tram final de la Noguera Pallaresa i riu Flamicell (Els
1160 Pallars). In: In: Turu, V., Constante-Orrios, A. (Eds.), Simposio de glaciariismo:

Formatted: English (United Kingdom)

Formatted: Spanish (Spain, International Sort)

1161 El Cuaternario en España y áreas afines, avances en 2011. Fundació Marcel
1162 Chevalier-AEQUA, Andorra la Vella, pp. 37-43.

1163 ~~Turu, V., Carrasco, R.M., Pedraza, J., Ros, X., Ruiz-Zapata, B., Soriano-López, J.M.,
1164 Mur-Cacuho, E., Pélachs-Mañosa, A., Muñoz-Martín, A., Sánchez, J.,
1165 Echeverría-Moreno, A., 2017a. Late glacial and post-glacial deposits of the
1166 Navamuño peatbog (Iberian Central System): Chronology and
1167 paleoenvironmental implications. Quat. Int. 1-14.
1168 <http://dx.doi.org/10.1016/j.quaint.2017.08.018>~~

Formatted: English (United Kingdom)

1169 Turu, V., Calvet, M., Bordonau, J., Gunnell, Y., Delmas, M., Vilaplana, J.M., Jalut, G.,
1170 2017b. Did Pyrenean glaciers dance to the beat of global climatic events?
1171 Evidence from the Würmian sequence stratigraphy of an ice-dammed
1172 palaeolake depocentre in Andorra. Geol. Soc. London, Spec. Publ. 433, 111-
1173 136.

1174 ~~[Turu, V., Carrasco, R.M., Pedraza, J., Ros, X., Ruiz-Zapata, B., Soriano-López, J.M.,
1175 Mur-Cacuho, E., Pélachs-Mañosa, A., Muñoz-Martín, A., Sánchez, J.,
1176 Echeverría-Moreno, A., 2018. Late glacial and post-glacial deposits of the
1177 Navamuño peatbog \(Iberian Central System\): Chronology and
1178 paleoenvironmental implications. Quat. Int. 470, 82-95.](#)~~

1179 Udías, A., López Arroyo, A., 2009. The Lisbon Earthquake of 1755 in Spanish
1180 Contemporary Authors. In Mendes-Victor, L., Oliveira, C.S., Azevedo, J.,
1181 Ribeiro, A. (Eds.), The 1755 Lisbon Earthquake: Revisited. Springer, Dordrecht,
1182 Netherlands, pp. 7-24.

1183 Vail, P.R., Colin, J.P., du Chene, R.J., Kuchly, J., Mediavilla, F., Trifilieff, V., 1987. La
1184 stratigraphie sequentielle et son application aux correlations
1185 chronostratigraphiques dans le Jurasique du basin de Paris. B. Soc. Geol. Fr. 8,
1186 1301-1321.

- 1187 Vázquez, J.T., Vegas, R., Barranco, L.M., 1987. Rasgos morfológicos de la depresión
1188 del Burguillo (Sistema Central Español) y su relación con deformaciones
1189 recientes. Cuaternario y Geomorfología 1, 295–308.
- 1190 Vera, J.A., 1994. Estratigrafía, Principios y Métodos. Ed. Rueda, Madrid, Spain.
- 1191 Vilaplana, J.M., Casas, A., 1983. Las cubetas de sobreexcavación glacial de Bono y
1192 Barruera (Alta Ribagorça, Pirineo Central). Cuad. Lab. Xeol. de Laxe 6, 283-
1193 309.
- 1194 Villamor, P., Capote, R., Tsige, M., 1996. Actividad neotectónica de la Falla de
1195 Alentejo-Plasencia en Extremadura (Macio Hespérico). Geogaceta 20, 925–
1196 928.
- 1197 Villamor, P., Capote, R., Stirling, M.W., Tsige, M., Berryman, K.R., Martínez-Díaz, J.J.,
1198 Martín-González, F., 2012. Contribution of active faults in the intraplate area of
1199 Iberia to seismic hazard: The Alentejo-Plasencia Fault. J. Iber. Geol. 38, 85–
1200 111.
- 1201 Villaseca, C., 2003. Sobre el origen del batolito granítico del Sistema Central Español.
1202 Bol. R. Soc. Esp. Hist. Nat. 98, 23-39.
- 1203 ▲ Villaseca, C., Barbero, I., Herreros, V., 1999. A re-examination of the typology of
1204 peraluminous granite-types in intracontinental orogenic belts. ▲ Trans. R. Soc.
1205 Edinb. Earth Sci. 89, 113-119.
- 1206 Vouillamoz, J.M., Baltassat, J.M., Girard, J.F., Plata, J., Legchenko, A., 2007.
1207 Hydrogeological experience in the use of MRS. Bol. Geol. y Min. 118, 531–550.
- 1208 Walsh, D. O., 2008. Multi-channel surface NMR instrumentation and software for
1209 1D/2D groundwater investigations. J. Appl. Geophys. 66, 140-150.
- 1210 Watanabe, T., Matsuoka, T., Ashida, Y., 1999. Seismic travelttime tomography using
1211 Fresnel volume approach. SEG Technical Program Expanded Abstracts 1999,
1212 1402-1405.
- 1213 Waxman, M.H., Smits, L.J.M., 1968. Electrical conductivities in oil-bearing shaly sands.
1214 SPE Journal 8, 107–122.

Formatted: English (United Kingdom)

Formatted: English (United Kingdom)

1215 Weichmann, P.B., Lavelly, E.M., Ritzwoller, M.H., 2000. Theory of surface nuclear
1216 magnetic resonance with application to geophysical imaging problems. *Phys.*
1217 *Rev. E.* 62, 1290–1312.

1218 Yamakawa, Y., Kosugi, K., Masaoka, N., Sumida, J., Tani, M., Mizuyama, T., 2012.
1219 Combined geophysical methods for detecting soil thickness distribution on a
1220 weathered granitic hillslope. *Geomorphology* 145-146, 56–69.

1221 Yanites, B.J., Ehlers, T.A., 2012. Global climate and tectonic controls on the
1222 denudation of glaciated mountains. *Earth Planet. Sci. Lett.* 325-326, 63–75.

1223 Yaramanci, U., 2000. Surface Nuclear Magnetic Resonance (SNMR) - A new method
1224 for exploration of ground water and aquifer properties. *Ann. Di Geofis.* 43, 1159-
1225 1175.

1226 Zohdy, A.A.R., 1989. A new method for automatic interpretation of Schlumberger and
1227 Wenner sounding curves. *Geophysics* 54, 244–253.

1228

1229 **Figure captions**

1230

1231 Fig. 1. Geological location of the study area. Geological diagram based on the *Mapa*
1232 *geológico de la Península Ibérica, Baleares y Canarias*. Scale 1: 1.000.000 (Rodríguez
1233 Fernández and Oliveira, 2015).

1234

1235 Fig. 2. A) Stages of retreat in Cuerpo de Hombre paleo-glacier and chronologies ka BP
1236 (based on Carrasco et al., 2015b). 3D image of the Navamuño Depression and Cuerpo
1237 de Hombre paleoglacier using ArcScene 10.4 and PNOA-2014 orthophoto
1238 (<http://www.ign.es>). B) General view of the Navamuño Depression -photographed from
1239 its SW boundary facing NE. C) Panoramic view of the Cuerpo de Hombre valley and
1240 Navamuño depression. Green arrow indicate glacier path. Letters indicate the
1241 morphostratigraphic formations (Carrasco et al., 2015b): PD_-peripheral deposits (B-
1242 boulders and M-moraine); PM_-principal moraine; ID_-internal deposits (M1 to M4,
1243 recessional moraines).

1244

1245 Fig. 3. A) Location of field work carried out in the Navamuño Depression (image: DTM5
1246 m, <http://www.ign.es>). B) Seismic array deployed in the depression distal zone. C)
1247 MRS1 data collection in the centre of the peat bog. D) Profile ERT9 transversal to the
1248 depression and drawn perpendicular to the Cuerpo de Hombre paleoglacier lateral
1249 moraine.

1250

1251 Fig. 4. Fracture network associated with Navamuño tectonic depression.

1252

1253 Fig. 5. Electrical resistivity curves from Vertical Electrical Sounding data. Main
1254 resistivity layers (G1 to G3). Layer G1 corresponds to the shallower geoelectrical layer.
1255 Resistivity from layer G2 is quite variable in resistivity and is interpreted as
1256 corresponding to alluvial fan and floodplain deposits. Layer G3 corresponds to older

1257 sedimentary deposits present in deeper positions in the Navamuño depression, but the
1258 G3 geoelectrical layer is also perched beneath the same deposits. Resistivity
1259 anomalies, as in VES 8 and VES 7, occur when electrodes sharply cross basement
1260 and sedimentary deposits. If this is not the case and a transition exists between granite
1261 and the sedimentary infill, then it is difficult to identify the depth of the basement (VES 4
1262 and VES 6).

1263

1264 Fig. 6. ERT tomography and geological interpretation including VES and MRS
1265 positions.

1266

1267 Fig. 7. Magnetic Resonance Sounding data and inversion results. Solid line-squares:
1268 groundwater signal. Circles: electromagnetic noise.

1269

1270 Fig. 8. Interpretation of the seismic profile using P-wave velocity and thickness of
1271 deduced seismic units. Seismic velocity is inversely related to the slope of the linear
1272 regression. Anomalies in PS1 and PS3 time-distance graphics are related with vertical
1273 jumps (erosive surfaces or sharp facies changes). All numbers that overlap geological
1274 materials are seismic velocities (in meters per second). NRZ = Non-Refraction Zone
1275 from an over-pressurized aquifer. Refractions coming from a denser terrain on PS1 (D)
1276 are interpreted as being related to the bedrock basement. On the opposite side of the
1277 profile (PS4), bedrock basement is located below the moraine at shallow depth.

1278

1279 Fig. 9. Isopach map of the Navamuño basin infill obtained from interpolating the
1280 thicknesses calculated in the geophysical data. In the zones where the upper limit of
1281 the granitic basement was not reached, a minimum thickness has been assigned,
1282 equal to the penetration reached with each technique. The infill isopachs are
1283 superimposed on the LiDAR topography produced by the IGN. The interpolation has
1284 been carried out using kriging at grid resolution of 5 m with a linear variogram, based

1285 | on all the data. ~~T~~Next the grid was then blanked outside the zone with zero thickness.
1286 | To improve the isopach map, we have used the cartographic boundary of the basin
1287 | infill, adding these data with zero thickness to the thickness values calculated using
1288 | geophysical methods.

1 **Near surface geophysical analysis of the Navamuño depression (Sierra de**
2 **Béjar, Iberian Central System): Geometry, sedimentary infill and genetic**
3 **implications of tectonic and glacial footprint**

4

5 Rosa M. Carrasco^a, Valentí Turu^b, Javier Pedraza^c, Alfonso Muñoz-Martín^{c,9}, Xavier
6 Ros^b, Jesús Sánchez^a, Blanca Ruiz-Zapata^d, Antonio J. Olaiz^e, Ramón Herrero-Simón^f,

7

8 ^a Dpt. of Geological and Mining Engineering, Univ. of Castilla-La Mancha, Avda. Carlos
9 III, s/n, 45071 Toledo, Spain.

10 ^b Fundacio Marcel Chevallier, Edifici Socio-Cultural de La LLacuna, AD500 Andorra la
11 Vella, Principality of Andorra.

12 ^c Dpt. of Geodynamic, Complutense University, C/ José Antonio Novais, 12, 28040
13 Madrid, Spain.

14 ^d Dpt. of Geology, Alcalá University, Ctra. A-II km 33,600, 28871 Alcalá de Henares,
15 Madrid.

16 ^e Non Seismic Methods. Repsol Exploration, c/ Méndez Álvaro, 44, 28045, Madrid,
17 Spain.

18 ^f Dpt. de Física i Enginyeria Nuclear, Polytechnic University of Catalonia (UPC). Física
19 Ed. TR1 (EET) C/Colom, 1, 08222 Terrassa.

20 ⁹ Instituto de Geociencias – IGEO (UCM, CSIC), C/ José Antonio Novais, 12, 28040
21 Madrid, Spain.

22 *Corresponding author. Tel.: +34 925268800

23 E-mail address: Rosa.Carrasco@uclm.es (R.M. Carrasco)

24

25 **Abstract**

26

27 The geometric and genetic characterization of the Navamuño depression
28 peatland system (Iberian Central System) is presented here using results from a
29 geophysical survey. This depression is a ~30 ha pseudo-endorheic flat basin over
30 granitic bedrock. Three geophysical techniques were used to map the subsurface
31 geology, and identify and describe the infill sequence: shallow seismic refraction (SR),
32 magnetic resonance sounding (MRS) and electrical resistivity measurements (VES and
33 ERT).

34 The three main geoelectrical layers (G1, G2, G3) identified in previous
35 research, have also been identified in the present work. Using the data obtained in this
36 new research we have been able to analyse these three geological layers in detail and
37 reinterpret them. They can be grouped genetically into two sedimentary units: an
38 ancient sedimentary body (G3), of unknown age and type, beneath an Upper
39 Pleistocene (G2) and Holocene (G1) sedimentary infill. The facies distribution and
40 geometry of the Upper Pleistocene was examined using the Sequence Stratigraphy
41 method, revealing that the Navamuño depression was an ice-dammed in the last
42 glacial cycle, resulting a glaciolacustrine sedimentation.

43 A highly permeable sedimentary layer or regolith exists beneath the
44 glaciolacustrine deposits. Below 40 m depth, water content falls dramatically down to a
45 depth of 80 m where unweathered bedrock may be present.

46 The information obtained from geophysical, geological and geomorphological
47 studies carried out in this research, enabled us to consider various hypotheses as to
48 the origin of this depression. According to these data, the Navamuño depression may
49 be explained as the result of a transtensional process from the Puerto de Navamuño
50 strike-slip fault during the reactivation of the Iberian Central System (Paleogene-Lower
51 Miocene, Alpine orogeny), and can be correlated with the pull-apart type basins
52 described in these areas. The neotectonic activity of this fault and the ice-dammed

53 processes in these areas during the Last Glacial Cycle (MIS2) were the main causes of
54 recent sedimentary infill in this depression.

55

56 **Keywords:** Near Surface Geophysics, Nuclear Magnetic Resonance, intermountain
57 basin, distensive faulting, Late Glacial Period, Iberian Central System.

58

59 **1. Introduction**

60

61 The small endorheic depressions known as *navas* are flat, treeless areas,
62 usually intermountain and sometimes marshy, common throughout the Iberian Central
63 System (ICS). The recent sedimentary evolution of these depressions involves slope,
64 fluvial and nival processes, and in some cases glacial and fluvioglacial processes
65 (Pedraza, 1994). As a result, these depressions have traditionally been studied to
66 reconstruct the environmental conditions pertaining in the ICS during the Quaternary
67 (see Ruiz-Zapata et al., 2011; López-Sáez et al., 2014). However, only very limited
68 data have been obtained to date relating to our understanding of the glacial record in
69 these areas (Ruiz-Zapata et al., 2011; López-Sáez et al., 2016). In previous studies,
70 the sedimentary infill analysed was of limited thickness (3 - 6 m), mainly homogeneous
71 (often only two sedimentary sequences appear) and not pre-Holocene in age (e.g.
72 Franco-Múgica, 1995; Rubiales et al., 2007; López-Sáez et al., 2014; Abel-Schaad et
73 al., 2014; Génova et al., 2016).

74 Taking these precedents into account, one of the aims of the research which
75 commenced several years ago into the ICS Pleistocene glaciation (Carrasco et al.,
76 2009) was to carry out a geological and geophysical prospective of these *nava*-type
77 depressions located in the former glacial areas. In the Navamuño depression (ND), one
78 of the *navas* analysed, a series of indicators was detected enabling the working
79 hypothesis that the ND is a unique case in the ICS. This interpretation was based on

80 the thickness of the sediments hosted by the depression and their posible genetic
81 relationship with the neotectonic activity and glacial dynamics of the Cuerpo de
82 Hombre, one of the reference paleoglaciers used for glacier evolution research in the
83 ICS (Carrasco et al., 2015a, 2015b).

84 With this approach, the main aim of this study is to establish in detail the
85 geometry of the ND, and interpret the thickness and sequence of its sedimentary infill
86 and its genetic context. Previous works (Ruiz-Zapata et al., 2011; Carrasco et al.,
87 2015a, 2015b; Turu et al., 2018) provided the essential data to support the present
88 study of the ND trough.

89 The methods chosen with this aim in mind were based on those applied in other
90 mountain systems in the Iberian Peninsula using geophysical techniques supported by
91 detailed geological surveys (Vilaplana and Casas, 1983; Bordonau, 1992; Turu 1999;
92 Turu et al., 2007, 2011; Pélachs et al., 2011; Pellicer et al., 2012; Salazar-Rincón et al.,
93 2013). Taking as a base the three resistivity levels identified in a previous study (G1,
94 G2, G3; Carrasco et al., 2015a), Electrical Resistivity Tomography (ERT), Vertical
95 Electrical Sounding (VES), Magnetic Resonance Sounding (MRS) and Seismic
96 Refraction (SR) have been applied in the ND for detecting and defining the presence of
97 sharp geological contacts (ERT and SR) such as faults or buried paleo-relief, sub-
98 horizontal stratigraphy (VES) and aquifers (MRS).

99

100 **2. Geological and geomorphological setting**

101

102 *2.1. Regional context*

103

104 The ND is located at 1500 m above sea level (asl) on the western versant of the
105 Sierra de Béjar (ICS, Fig. 1) with a surface area of ~30.76 ha. This depression is
106 confined between scarped slopes on the granitic basement and one of the moraines of
107 the Cuerpo de Hombre paleoglacier (Fig. 2). The bottom of the depression is a

108 seasonal flood-plain with peatland development, currently dissected by fluvial
109 channels.

110 ND forms part of the fracture corridor associated with the Puerto de Navamuño
111 fault (PN fault) and has been classified as a Variscan strike-slip fault (Bellido-Mulas,
112 2006) associated with the NE-trending strike-slip faults of Alentejo-Plasencia (AP;
113 a.k.a. Plasencia, Odemira-Plasencia, or Messejana-Plasencia; > 500 km) and Hervás-
114 Candelario (HC; around 40 km) (Fig. 1). Together these faults are responsible for the
115 Jerte-Aravalle and Hervás-Candelario corridor-type valleys which limit the Sierra de
116 Béjar pop-up (Sanz-Donaire, 1979; Moreno, 1991; Carrasco, 1997).

117 All these reliefs were formed during the Alpine Orogeny as the result of the
118 transmission to the interior of the Iberian Plate of the compressive stress generated at
119 its edges due to collision with Eurasia during the lower Oligocene-Miocene
120 (Cantabrian-Pyrenean) and with Africa since 9 Ma (De Vicente and Vegas, 2009). De
121 Vicente et al. (2007) and De Vicente (2009) propose partitioning of deformation in the
122 ICS with a generalized NNW-SSE shortening in a transpressive regime. This regime
123 has not varied substantially from the Oligocene to the present, although its maximum
124 intensity was concentrated during the Lower Eocene-Miocene (Continental Iberia-
125 Eurasia collision). Fission track dating (De Bruijne and Andriessen, 2002), seismic
126 (Olaiz et al., 2009; Muñoz-Martín et al., 2012), and GPS (Garate et al., 2015) data
127 confirm this model.

128 Minor depressions such as the ND are common throughout the ICS and the
129 Iberian Massif and have been analysed in depth along the AP fault (Brum da Silveira,
130 1990; Carrasco and Pedraza, 1991; Cabral, 1995, 2012; Capote et al., 1996; Brum da
131 Silveira et al., 2009; De Vicente et al., 2011; Villamor et al., 2012). According to these
132 data, these depressions originated in the Paleogene-Lower Miocene as pull-apart type
133 sedimentary basins and some of them continued active throughout the Miocene.
134 Others, however, halted at the start of the Upper Miocene and their function changed to
135 shallow sedimentary basins regulated by neotectonic readjustments during the recent

136 times (Upper Pliocene and Quaternary). In other ICS depressions developed on a rock
137 substratum (El Burguillo and Alto Tormes valleys; Fig. 1), some anomalies detected in
138 the layout of the current drainage network have also been interpreted as indicators of
139 neotectonic activity (Vazquez et al., 1987; Pol et al., 1989).

140 Although this area of the ND is presently characterized by moderate to very low
141 seismic activity, according to instrumental and historical records (IGN, 2016), the 1755
142 Lisbon earthquake (Mendes-Victor et al., 2009) originated small-scale slope
143 movements in the Valle del Jerte (11.83 km SE of ND) and resulted in cracks in the
144 walls and partial roof collapse in some monumental buildings in the city of Plasencia
145 (40.53 km SW of ND) (Carrasco, 1997; Udías and López-Arroyo, 2009). On the other
146 hand, and this is one of the fundamental points under debate, the neotectonic activity
147 of these faults during the Quaternary is framed within the context of low deformation
148 rates, reflected in the presence of slow faults with much longer return periods than the
149 time period covered by the historical or instrumented seismic data (Cabral, 2012;
150 Foroutan et al., 2016).

151 The lithological context of the ND substratum is that of the Sierra de Béjar,
152 which forms part of one of the most important granitic batholiths of the Iberian Massif
153 (Villaseca et al., 1999; Villaseca, 2003). The most abundant rocks in the area are
154 monzogranites and Variscan granodiorites, with associated migmatites, schists,
155 quartzites and other pre-Variscan metasediments. In the ICS, and the Iberian Massif in
156 general, various supergenic weathering sequences have been identified in these
157 granitic substrata. The oldest (pre-Tertiary), thick weathering mantles correspond to
158 laterite profiles (Molina-Ballesteros et al., 1991, 1997). The most recent weathering
159 mantles (Tertiary and in some cases Quaternary) are less thick, sometimes sub-
160 surficial, and are associated with wash-exposure rock weathering stages and therefore
161 their transformation levels vary, ranging from simple bisialitization (predominance of
162 montmorillonite) to monosialitization (predominance of kaolinite) (Centeno and Brell,
163 1987; Molina-Ballesteros et al., 1994).

164

165 *2.2. Study area and hypothesis*

166

167 In earlier studies of the ND (Carrasco et al., 2015a), a sedimentary trough was
168 detected, occupying part of the depression and hosting sediments calculated to be
169 approx. 60 m thick. The sedimentary sequence, established from lithological data (16
170 m test bore) and from data obtained using geophysics, consists of three geoelectrical
171 layers (Carrasco et al., 2015a; Turu et al., 2018): G1 (10-18 m thick), nearest the
172 surface, interpreted as coarse sand with intercalated clays and silts, sometimes
173 presenting zones with organic material indicating the presence of paleochannels and/or
174 peatbog zones; G2 (7-10 m thick in some zones, 40-50 m thick in others), interpreted
175 either as a sedimentary debris-flow deposit, highly porous, coarse-grained, and
176 saturated with water (arkosic), or as arenized granite; and G3 substratum of the trough
177 on non-weathered granitic rock. The nomenclature of these layers has been
178 maintained in this research, although the layers may be redefined with the new data
179 obtained. ¹⁴C dating establishes approximate ages of 5700 BP for a sample located at
180 485 cm and 10000 BP at a level one meter lower (565-570 cm) and 13720 BP for a
181 level located at depth 16 m (Ruiz-Zapata et al., 2011; Carrasco et al., 2015a; Turu et
182 al., 2018).

183 These earlier studies mentioned the possibility that the evolution of the
184 sedimentary trough in ND was related to an obstruction process generated by the left-
185 lateral moraine of the Cuerpo de Hombre paleoglacier, which defines the eastern
186 margin of the depression. The abrupt change of direction presented by this left lateral
187 moraine of the Cuerpo de Hombre, aligned along NW-SE and NNE-SSW structures,
188 has also been highlighted in various studies (Rubio, 1990; Carrasco et al., 2013,
189 2015b). This left-lateral moraine forms part of the morphostratigraphic formation called
190 'principal moraine' (PM), and has been used as reference to establish the evolutive

191 sequence of the ICS paleoglaciers (Pedraza, 2012; Pedraza et al., 2013; Carrasco et
192 al., 2013).

193 The evolutive sequence in the Cuerpo de Hombre paleoglacier was dated using
194 ^{10}Be -TCN technique on scattered erratic blocks or moraine boulders. As a result of this
195 work, the following ages have been established (Carrasco et al., 2015b) (Fig. 2A, 2C):
196 (1) glacial maximum (~25.0 ka; MIS2); (2) some retreat and stabilization stages formed
197 after ~24.3 ka and before ~20.6 ka; (3) some readvance and stabilization phases
198 shown by the PM formation, dated later than ~20.6 ka and earlier than ~17.8 ka; and
199 (4) a deglaciation process showing three stadials in the late glacial sequence dated to
200 (minimum ages) ~17.5 ka, ~13.9 ka and ~11.1 ka.

201 All these earlier data as well as those corresponding to the regional geological
202 context described in the previous section, were used as the basis for the central
203 hypothesis on which the new research described herein was planned and carried out.
204 This hypothesis considers that the primary origin of the ND converged with the pull-
205 apart type basins described in these areas, and its recent evolution was associated
206 with some tectonic readjustments and with the Cuerpo de Hombre paleoglacier. Thus,
207 the chronoevolutive sequence of this paleoglacier has been used as reference to
208 establish the sequence and chronology of the infill stages of the ND depression during
209 the obstruction period.

210 This is a topic of general interest in the study of paleoglaciers, since it related to
211 the impact of non-climatic factors on glacier dynamics and therefore on the typology
212 and arrangement of geomorphological indicators used as reference to establish
213 chronologies, evolutive sequences and global paleoclimatic deductions (Olvmo and
214 Johansson, 2002; Ber, 2009; Glasser and Ghiglione, 2009; Cotton et al., 2014; Yanites
215 and Ehlers, 2012; Prasicek et al., 2015; Bathrellos et al., 2017).

216

217 **3. Methods**

218

219 *3.1. Surficial geology and fracture network*

220

221 Geological mapping was produced using vertical aerial photographs (Scale 1:
222 10000 and 1:18000) and PNOA-2014 orthophotos (Instituto Geográfico Nacional, IGN).
223 This procedure and field surveys were used to define the geological and
224 geomorphological units presented in this study.

225 There was abundant information previously available on the bedrock lithology
226 (Bellido-Mulas, 2006) and the glacial morphology of the Sierra de Béjar and its
227 immediate surroundings as a whole, including the ND (Sanz-Donaire, 1979; Rubio
228 1990; Carrasco, 1997; Carrasco et al., 2013, 2015a, 2015b). Nevertheless, the
229 boundaries of the depression and contacts between the different lithological formations
230 have had to be mapped with new, complementary data. A detailed morphotectonic
231 information has also been produced which includes scarps, alignments, fractures and
232 fracture corridors. The main aim of this information is to contribute a complementary
233 data series to the geophysical research into the deposits hosted in the depression, as
234 this is where the search has been focused for indicators to interpret the genesis and
235 evolution of this depression and the possible existence of neotectonic activity. This
236 methodological approach takes into account the precedents described above in
237 Section 2.0 to interpret neotectonic activity in these areas. In all cases, indicators of
238 this activity have been obtained in the sedimentary fill in the depressions (fractured or
239 folded sediments, abrupt or anomalous contacts, etc.). This is because the data
240 provided by the rock substrate formations are limited to some faceted surfaces and
241 anomalies in the drainage network which are often difficult to interpret and must be
242 obtained by studying wider areas than the intermountain depressions. On the other
243 hand, this information is a basis for correlation with morphostructures established at a
244 regional level in other depressions similar to the ND, such as the Amblés, Jerte and
245 Garganta del Villar valleys (Fig. 1).

246 The aim of the field work was to carry out a detailed review of the geological
247 formations obtained from photointerpretation and to characterize the typology of some
248 surficial formations not analysed in previous studies. In this review special attention
249 was paid to the location and typology of weathered bedrock materials (*grus*), as in
250 some cases these formations present hydrogeological, geotechnical and geophysical
251 characteristics similar to the arkose formations which appear in some ICS intermountain
252 depressions.

253

254 3.2. Geophysical methods

255

256 3.2.1. Vertical electrical soundings (VES) and Electrical resistivity tomography (ERT)

257

258 Electrical resistivity methods (VES and ERT) consist of obtaining the apparent
259 resistivity (ρ_{ap}) of rocks and soils from the voltages observed in potential electrodes, in
260 response to the introduced DC intensity in the current electrodes. If the distance
261 between the current electrodes is gradually increased in relation to a central point, the
262 vertical resistivity distribution can be examined, i.e. in 1D (VES). In ERT an electrode
263 array is deployed laterally along a profile, obtaining a 2D resistivity model of a subsoil
264 section (Reynolds, 2011). The ERT results obtained enable an understanding of the
265 bedrock geometry and differentiate infill types from their contrasting electrical resistivity
266 (Descloitres et al., 2008; Hausmann et al., 2013).

267 VES data acquisition was completed in 3 survey campaigns: the first two
268 provided a preliminary estimation of the depression geometry (Carrasco et al., 2015a)
269 and the third completed the data required to define the geometry and produce the final
270 infill model. All VES were carried out with a Schlumberger-type configuration and the
271 maximum array length is 266 m (Fig. 3). For a correct interpretation, the ‘apparent’
272 resistivity values (i.e. the mean value of the rock volume affected by the current flow)
273 must be converted to ‘real’ resistivity of the different subsoil units using an inversion

274 process, in either 1D (VES, Zohdy, 1989; Barker, 1992) or 2D (ERT, Loke and Barker,
275 1996; Loke et al., 2010). In the case of VES, due to the principle of electrical
276 equivalence (Maillet, 1947; Bhattacharya and Patra, 1968; Reynolds, 2011), there is
277 inherent uncertainty in the method, in that the electrical behaviour of a layer is defined
278 by the combination of its thickness and its resistivity, which may generate important
279 uncertainty. This uncertainty is limited or resolved by: (1) an equivalence analysis and
280 (2) inclusion of other subsoil survey techniques. In the ND the VES inversion and
281 equivalence analysis were performed using Moscow State University IPI2Win free
282 software (Bobachev et al., 2003), obtaining a 1D resistivity model and corresponding
283 equivalence analysis (see supplementary material).

284 ERT data were collected in field work using a RESECS DMT 64 channel
285 resistivity meter with 5 m spacing between electrodes. Nine profiles were measured
286 with lengths from 205 - 275 m (Fig. 3). Wenner and Dipole-Dipole electrode
287 configurations were used and the maximum depth reached was 70 m.

288 RES2DINV software (Loke and Barker, 1996; Loke et al., 2010) was used for
289 field data inversion. A normal inversion algorithm using 4-node finite element modelling
290 has been used. The size of the elements was the same as the distance between
291 electrodes (5 m). The resistivity data were of very good quality with high S/N ratio, and
292 repeat measurement errors below 1%. The ND data inversion models gave
293 consistently low error statistics with RMS <3%. The result of all this information,
294 combined with VES, enabled a better understanding of the 2D distribution of the
295 different geo-resistive bodies and how they relate to surface geomorphological and
296 geological data.

297

298 3.2.2. Magnetic resonance sounding (MRS)

299

300 The MRS technique is applied in different geological contexts (Behroozmand et
301 al., 2015), and allows quantification of porosity, permeability and thickness of aquifer

302 levels to a depth of the first 150 m (Yaramanci, 2000; Vouillamoz et al., 2007; Lange et
303 al., 2007; Mejías and Plata, 2007; Plata and Rubio, 2008; Hertrich, 2008).

304 MRS is based on the properties of nuclear magnetic resonance (NMR) which
305 uses the resonance produced in protons subjected to a magnetic field with a specific
306 frequency. The method consists in energising the terrain with an increasing
307 electromagnetic pulse moment (q , in A·ms) generated in a loop, with the aim of
308 penetrating deeper into the subsoil (Table 1). When the pulse terminates, the terrain
309 response is logged as initial amplitude, (E_0 in nV), decay time (ms) and phase
310 (degrees). The initial amplitude value (E_0) is directly related to the amount of water
311 contained in the soil to the slice depth affected by the pulse, while the decay time ($T2^*$)
312 depends on the hydraulic permeability. To suppress random noise and improve the
313 signal/noise ratio, each pulse is repeated several times for signal-stacking purposes.
314 Greater depth is reached in the research by increasing the value of q , with a maximum
315 depending on the loop dimensions. The test sounding consists of various
316 measurements of increasing values of q , to establish functions E_0 and $T2^*$ as a function
317 of q .

318 These parameters depend on the electrical conductivity of the subsoil, magnetic
319 field (inclination and magnitude), loop size, electromagnetic noise and possible
320 presence of magnetic rocks (Weichman et al., 2000; Hertrich, 2008).

321 Two MRS soundings were carried out in the ND at the same point but using
322 different sized loop (30x30 m and 60x60 m) (Fig. 3). This survey method has been
323 successfully tested in other geological contexts (Turu, 2012; Behroozmand et al., 2015)
324 with a twofold aim: to achieve sounding to the maximum depth possible with the
325 apparatus used but without resolution loss in the first tens of meters of the subsoil.
326 NMR data were collected in the field using Iris-Instruments NUMIS LITE equipment
327 which can penetrate to maximum depth 90 m. The field data inversion was performed
328 using Shushakov and Legchenko (1994) and Legchenko and Shushakov (1998)

329 methods, and the results obtained enabled 1D quantification of the hydrogeological
330 parameters mentioned above.

331

332 3.2.3. Seismic refraction (RS)

333

334 Seismic techniques are often used to study Quaternary deposits and research
335 the subsoil layers, paleorelief geometry and geomechanical properties of surficial
336 deposits (Turu, 1999; Turu et al., 2007; Schrott et al., 2003; Yamakawa et al., 2012).
337 This technique is based on measuring the travel time of P waves which travel directly
338 or critically refracted to a geophone array deployed along a seismic line (Sheriff and
339 Geldart, 1991; Reynolds, 2011). Analysis of the travel times picks from each source to
340 the geophone array are plotted as time/distance curves on a time-distance graph. The
341 qualitative analysis of these travel times using the general reciprocal method (GRM)
342 (Palmer, 1980), or tomographic techniques (Watanabe et al., 1999; Sheehan et al.,
343 2005), enables reconstruction of the contacts between different media (refractors) and
344 the depth distribution of the P wave velocities. The seismic source used varies
345 depending on the test depth, and a sledge hammer is usually used in superficial
346 studies to reach depths of up to 25 m.

347 The results obtained by seismic refraction are a 2D vertical section of the P
348 wave velocity distribution (V_P), with lateral resolution defined by the distance between
349 the geophones (normally 1 - 5 m).

350 The seismic survey in the ND centred on the axial zone and on its northern
351 margins. Five 48 m-long seismic refraction profiles were generated, with geophones
352 regularly spaced at 6 m intervals (Fig. 3). The seismic waves were generated by
353 percussion with a 6 kg hammer on a metal plate placed on the ground, with shooting
354 points at each end and in the centre of the profile. As the ND is included in a Special
355 Protection Area for birds, more efficient seismic wave generation methods were ruled
356 out.

357 The seismograph used was a 16-channel prototype designed by the
358 Universidad Politécnica de Cataluña (UPC). Signal processing and inversion was
359 performed using specific software (Anasim 6.0; Herrero-Simón, 2003) which allows
360 detection of refracted and reflected waves and subsequent subsoil characterization
361 using models of inclined layers (velocity, depth and inclination). This was particularly
362 useful in the peat bog profiles, as the low ground compaction muffled the signal
363 generated with the hammer. The results obtained were verified using Simusism2
364 software (Herrero-Simón, 2007), also produced by the UPC, which simulates seismic
365 wave propagation in subsoils with random velocity distribution.

366 The aim of the seismic refraction was to define the contact between low-velocity
367 to higher-velocity layers, such as from overburden to bedrock and/or highly weathered
368 rocks, and from peat to clastic sediments. Also the presence of discontinuities in the
369 upper surface of the basement, produced by faults and/or erosive surfaces. In these
370 cases, sharp contacts such as occur in a gully or in faults, delay the wave arrival time
371 and disturb the dromochronic representation. Where this occurs, the throw can be
372 calculated as the delay is exponentially related to the seismic velocity of the layers
373 involved.

374

375 **4. Results and interpretation**

376

377 Although the ND is generally rectangular in shape, bounded by mainly
378 rectilinear scarped slopes, when analysed in detail the boundaries are found to be
379 more complex. The slopes forming the northern and western sides are formed on
380 granitic rocks (monzogranites and porphyritic biotite granodiorite; Bellido-Mulas, 2006)
381 and associated with NE-SW and NNE-SSW fractures (Fig. 4). The mainly rectilinear
382 northern boundary is due to a minor ENE-WSW fault. The western boundary is less
383 regular, with directional changes originating in a series of minor faults, which displace
384 the two main NNE-SSW and NNW-SSE faults. These morphostructural differences are

385 also clearly seen in the fluvial plain forming the floor of the depression and in the
386 granitic materials. The northern area of this fluvial plain is directly linked to the scarped
387 slope with a clear knickpoint slope break and the granitic rock appears fairly fresh. In
388 the western part, however, between the scarped slope and the fluvial plain,
389 intermediate minor *glacis* reliefs are seen, formed on the weathered rock substratum
390 *grus* and surficial deposits (lithosoils and slope deposits; Figs. 2B, 5).

391 The granitic materials are in general unweathered and very heavily fractured.
392 The weathered rock is found in bands associated with fractures, and on the surface
393 forms a regolith composed of *grus*, scree and soil. In places where the weathered rock
394 can be observed in situ, and in line with standard field classifications (Anon, 1977;
395 Dearman, 1978), two degrees of transformation can be identified: Grade III (moderate),
396 in which the rock shows general discolouration and is easily broken by hand, although
397 the majority of minerals are recognizable most of the original textures have been lost;
398 and Grade II (slight), in which the original minerals, textures and structures of the rock
399 are recognizable (although the rock is difficult to break up by hand and there are
400 abundant fragments of fresh rock) but shows discolouration due to migration of iron
401 oxides resulting from the transformation of certain minerals, particularly biotite.

402 The southern boundary is more complex and is defined by a system of steps
403 and shoulders due to two fault sets, one parallel to and the other conjugate with the PN
404 fault. These steps have been fossilized and smoothed by the outermost surficial
405 deposits of the Cuerpo de Hombre paleoglacier and by a torrential fan system. All
406 these geomorphical features penetrate into the interior of the depression and mark the
407 southern limit of the base fluvial plain. Finally, the eastern boundary, defined by the
408 slope corresponding to the left lateral moraine of the Cuerpo de Hombre paleoglacier,
409 is fairly rectilinear and is parallel to the western side, with a clearly defined contact with
410 the depression base fluvial plain (Figs. 2, 5).

411 The base of the depression is a fluvial plain where a channel system forms a
412 general network pattern, with occasional meanders or anastomosis and some flood
413 zones where small peatland and marshy formations accumulate.

414

415 *4.1. Vertical Electrical Soundings (VES)*

416

417 Three geoelectrical layers have been detected in the ND, confirming and
418 complementing previously obtained data (Carrasco et al., 2015a). These layers are
419 called G1, G2 and G3 from highest to lowest (Table 2, Fig. 5).

420 The first resistive layer (G1) is found immediately under the ground surface and
421 has variable resistivity, due to its heterogeneous lithological composition. In general
422 terms, it is 3-4 m thick, although in the southernmost part of the depression centre, a
423 thickness of up to 20 m has been detected (VES 8).

424 The second resistive layer (G2) obtains resistivity values ranging from 500 - 800
425 Ωm , except in the distal zone of the depression (between VES 5 and 9) which exhibits
426 contrasting resistivity values of 250-300 Ωm . Where geoelectrical layer G2 has been
427 identified, the thickness varies, oscillating between 20 and 50 m.

428 The third resistive layer (G3) corresponds to the deepest sediment levels
429 deposited in the depression and overall this layer displays resistivity values between
430 600 and 1600 Ωm .

431 In general, stacking of the three geoelectrical layers is observed but exceptions
432 are found at the edges of the depression. Close to the moraine (Fig. 5) the three
433 geoelectrical levels described are detected in VES 1 position, and also resistive
434 deposits which form the lateral moraine of the Cuerpo de Hombre paleoglacier (Fig. 6,
435 ERT 1 and ERT 2). In contrast, the geoelectrical layers are not present above the
436 moraine sediments (VES 3). The absence of contrasting electric resistivity between
437 levels G3 and G2 in the central sector of the depression (VES 6) makes them difficult
438 to separate with this survey method. In the northern sector (VES 4) the existence of the

439 nearby crystalline basement did not facilitate sedimentation of all the geoelectrical
440 layers. The granitoid basement with characteristic relatively high resistivity (around
441 2000 Ωm) was identified in the central area of the depression (VES 7 and VES 8) from
442 the abrupt slope change shown by the resistivity curve, otherwise it is difficult to detect,
443 as for example in VES 4 and 6. VES 5 is the only one with an H-type curve, which
444 means that the second layer has a lower resistivity than the one above and the one
445 below. For this reason, VES 9 was carried out nearby. The final VES has 4 layers and
446 any significant continuity in the intermediate layer is ruled out. For this reason, a
447 dashed line is drawn between VES 9 and VES 5 on the map in Fig. 5.

448

449 *4.2. Electrical Resistivity Tomography (ERT)*

450

451 The depth reached in the ERT sections ranged between 40 and 60 m and the
452 three geoelectrical layers defined above (and previously, Carrasco et al., 2015a) are
453 identified, i.e. G1, G2 and G3 (Fig. 6).

454 Geoelectrical layer G1 exhibits the greatest resistivity (1600 - 16000 Ωm). This
455 implies genetically that G1 has a larger overall grain size and a lower silt and clay
456 content (cf. Waxman and Smits, 1968). In geometric terms, there are notable thickness
457 variations of this layer (ERT 3, Fig. 6). Sedimentary accretion (ERT 3 and ERT 7, Fig.
458 6) denotes greater accommodation northwards, at the depression centre.

459 The contact between layer G1 and the other two layers displays paraconformity in
460 ERT 3, and overall concordance in ERT 1 and ERT 7, above all towards the
461 depression centre (ERT 2 and ERT 8, Fig. 6). In G1, the onlap contact of the resistive
462 materials in ERT 7 and ERT 1 is observed with sedimentary aggradation towards the
463 depression centre. Less marked onlap contact can also be deduced from the
464 synsedimentary tilting of the base of layer G2 in the central part of the depression (ERT
465 2). These onlap contacts are interpreted as tilting (as in ERT 2) or fossilization of fault
466 scarps (as in ERT 7 and ERT 1) which affect the basement rock (layer G3). The

467 subsidence activity would then be responsible for the synsedimentary accretion
468 towards the north in layers G1 and G2 (ERT 1 and ERT 7). Finally, the granitic
469 substratum which forms the depression boundary is identified by the sharp lateral
470 resistivity contrasts with layers G2 and G3 (ERT 2 and ERT 8, Fig. 6). This sharp
471 contact is interpreted as the confinement of sedimentary infill by sinking of the rock
472 basement. Subsidence activity would then be responsible for the synsedimentary
473 accretion towards the north in layers G1 and G2 (ERT 1 and ERT 7). Finally, the
474 granitic substratum which forms the depression boundary is identified by the sharp
475 lateral resistivity contrasts with layers G2 and G3 (ERT 2 and ERT 8, Fig. 6). This
476 sharp contact indicated in Fig. 6 is interpreted as the confinement of sedimentary infill
477 by sinking of the granite basement.

478 Goelectrical layer G2 is more heterogeneous than G1 and with lower resistivity
479 (20 - 2000 Ω m). This layer exhibits greater geometrical development towards the
480 centre of the basin and marked lateral variations in resistivity, especially in the central
481 zone of the depression (ERT 2, ERT 8, Fig. 6). Thus, the fine-grained sedimentary
482 facies (silts and clays) are interpreted in the conductive nuclei in ERT 2 and ERT 8 and
483 should be attributed to lacustrine environment deposits. On the contrary, the most
484 resistive bodies correspond to coarse-grained sedimentary facies (sands and gravels),
485 attributable to fluvial environment deposits (ERT 2, Fig 6).

486 Goelectrical layer G3 corresponds to the lower level of the ND infill, with low
487 resistivity (200 - 2000 Ω m) contrasting with the rock substratum resistivity (2000 -
488 20000 Ω m). This goelectrical layer rests directly on the resistive rock substratum in
489 the centre of the depression (ERT 2 and ERT 8, Fig. 6). In the southern sector of the
490 depression, G3 presents an important vertical variation in resistivity and also horizontal
491 variation, although to a lesser degree. In e.g. ERT 7, vertical values range from 3 k Ω m
492 to up to ten times lower. In contrast, the horizontal resistivity ratio is half of that
493 detected on the left margin of ERT 1 and ERT 3 and that of the opposite edge (Fig. 6).

494 These resistivity variations can be interpreted as variations in the sedimentary infill
495 grain size, just as in geoelectrical layer G2. However, the nature of the geoelectrical
496 layer G3 is unknown, in contrast to that of G1 and G2 which have been identified by
497 Carrasco et al. (2015a) in a 8 m depth borehole performed in the centre of the
498 depression.

499 Three test bores were performed in ND, with one reaching a maximum depth 16
500 m, and used for paleoenvironmental studies (Ruiz-Zapata et al., 2011; Carrasco et al.,
501 2015a; Turu et al., 2018). In this sounding, 3 layers can be distinguished from top to
502 bottom: the top layer (0-300 cm) is composed of clayey silt interspersed with gravel
503 (geoelectric unit G1); the second layer (300-800 cm) comprises sands with beds of
504 finely-laminated clay to 500 cm, and then sands and gravels interspersed with beds of
505 clays and silts to the bottom of the sounding (geoelectric unit G2). Carbon-14 dating
506 presented in Carrasco et al. (2015a) and Turu et al. (2018) shows approximate ages of
507 5700 BP for a sample located at 485 cm and 13720 BP for a level located at depth 16
508 m. This indicates that in the central part of the depression, the bottomset is Late Glacial
509 in age.

510

511 *4.3. Magnetic Resonance Sounding (MRS)*

512

513 Two double pulse MRS were performed in ND. Quantitative results show that
514 contact with the impermeable substratum is located at a depth of approximately 80 m,
515 while at 50 - 70 m there is a zone with gradually decreasing porosity and permeability
516 (Figs. 7C, 7D). Interpretation of the field-curve data from the two surveys undertaken
517 suggests that water is present in all geoelectrical layers in the first 30 m (Fig. 7C),
518 decreasing the water content from 30 to 60 m depth. The main aquifer is found in the
519 first 40 m from the subsurface, although it reflects the inherent heterogeneity of the
520 depression infill sedimentary deposits (Fig. 7C). The infill layer down to 40 m,
521 containing the main aquifer, corresponds to electrical units G1 and G2, while the zone

522 with gradually decreasing permeability (40 - 80 m) corresponds to unit G3. This unit
523 exhibits relatively high values of resistivity with lateral changes, and a progressive
524 decrease in water content and permeability. The most likely interpretation of its nature
525 are the following: (1) that it is a sedimentary infilling with a lower porosity towards its
526 base; and (2) that it is a zone of altered basement rock, with a maximum alteration at
527 its top, and a reduction with depth.

528 Water is not detected in the main aquifer at depths of 13 - 17 m. Given that only
529 free water is detected by MRS, this apparently small quantity of water can only be
530 justified by the presence of low porosity in clay deposits. In addition, the free water
531 presence in the clay displays a very short relaxation time (Fig. 7D) in the MRS signal
532 and may not be detected due to instrumental limitations (Turu, 2012). The relaxation
533 time of the water signal is a permeability-related parameter (Mejías and Plata, 2007)
534 and both $T2^*$ and $T1$ show a wide range of values (Figs. 7E, 7F). This is interpreted as
535 significant infill grain-size variability, ranging from clay and silt (100 ms; Fig. 7E) to
536 sand and gravel (values higher than 300 ms; Fig. 7F). However, $T2^*$ and $T1$ relaxation
537 times do not converge at all depths. Usually $T1 > T2^*$ but in the case that they are not,
538 $T1$ measurements are more approximate and pseudo-saturation recovery
539 complications would not produce a 90° pulse and distribution of tip angles, reducing the
540 estimation of $T1$ (Grunewald and Knight, 2011). This is the case for Fig. 7E at a 22 m
541 depth; here $T2^* > T1$ (Fig. 3F), just at the bottom of the inferred fine grained deposits or
542 low resistive (ERT 8, Fig. 6). If $T2^* \ll T1$ then paramagnetic geology produces
543 inhomogeneous field dephasing, due to magnetic grains or field-scale magnetic
544 anomalies reducing $T2^*$ relaxation time (Walsh, 2008). This seems to be the case
545 below a depth of 36 m, where $T2^*$ is systematically lower than $T1$.

546

547 *4.3. Seismic Refraction (RS)*

548

549 The seismic refraction sections performed along the northern edge of the
550 depression allowed the reconstruction of an NW-SE transect to 15-20 m in depth (Fig.
551 8). In this section the contact can be observed between the sedimentary infill (V_p
552 between 350 and 1350 m/s, Table 3) and the rock substratum ($V_p > 1800$ m/s). Minor
553 variations in sedimentary fill velocity were observed, interpreted as erosive surfaces,
554 but in general terms the refractions fit a stratified model.

555 In profile RS1 delays can be observed in the refracted wave reception time (Fig
556 8), which is linked to sharp contacts attributable to filled gullies, as those described by
557 Turu et al. (2018). In the sector of this profile near the slope and in RS5, the presence
558 of rock substratum is characterized by high seismic velocity. In profile RS4, beneath
559 the moraine and at a shallow depth, the rock substratum has also been detected from
560 its seismic velocity (ERT 8, Fig. 6 and Table 3). The geological units detected in RS3
561 and RS4 are different at the edge of the lateral moraine which is the boundary of the
562 ND, interpreted as an onlap contact between the moraine and the depression infill (Fig.
563 8). The absence of refracted waves in this part of the profile is due to an inversion of
564 the seismic velocity ($V_1 > V_2$), implying that the underlying deposits are less dense than
565 those nearer the surface. The explanation for this anomaly may be related to the
566 presence of a pressurized aquifer.

567 A refractor located at a depth of 9 m was identified in the overlap of the two
568 seismic profiles RS3 and RS2 (Fig. 8). Because of its continuity and increasing depth
569 towards the centre of the depression, this layer can be catalogued as a first order
570 reflector equivalent to the division of the sedimentary fill between the geoelectric layers
571 G2 and G3 in the electrical tomography profiles (ERT 8).

572

573 *4.4. Stratigraphic architecture inferred from geophysical data*

574

575 The architecture of the infill examined can be subdivided into depositional
576 sequences and system tracts, as has already been carried out in other glacial

577 obstruction depressions (Jalut et al., 2010; Turu et al., 2017). The limits between
578 depositional sequences are the result of stratigraphic discontinuities and their
579 correlative surfaces throughout the basin under analysis (Vail et al., 1987). It is
580 therefore important to identify them from the layer geometry or sharp changes in their
581 properties (Turu et al., 2017). Based on this, unconformity surfaces (US) are
582 highlighted on the electrical tomography profiles (Fig. 6).

583 The sedimentary fill of geoelectrical layer G1 was identified by Carrasco et al.
584 (2015a), allowing the depositional system of G1 to be described as fluvial type. Proof of
585 this is the contacts located in the seismic refraction profile (Fig. 8) that are associated
586 with paleochannels.

587 Geoelectrical layer G2 is interpreted as genetically related to an alluvial fan
588 supplied by marginal fluvio-glacial flows from the Cuerpo de Hombre glacier. This delta
589 fan is centred on the kame terrace where fluvio-glacial flows originated (Fig. 5). Thus,
590 there must have been a lacustrine paleoenvironment in the ND. This kind of
591 environment progresses from the margin to the bottom of lake (in the ND located
592 between ERT1 and ERT 2) as a Gilbert delta type, in which the sediments are packing
593 like sigmoids identified as clinofolds in the ERT survey. As occurs in other similar
594 contexts (Jalut et al., 2010; Turu et al., 2017), in the ND drainage was obstructed by
595 the ice and/or the lateral moraine of the glacier. The low resistivity materials present in
596 ERT 8 are therefore interpreted as fine-grained sediment at the bottom of this ice-
597 dammed lake.

598 As also observed in other areas (Turu et al., 2017), the local base-level falls and
599 the sedimentary facies change when the ice-damming comes to an end, producing
600 diastems (unconformity surfaces, US). These erosive surfaces (ERT 8) mark the start
601 of a new depositional sequence, initiating a Low System Tract (LST; Catuneanu, 2006).
602 When the obstruction ceases, lacustrine sedimentation also stops, and an alluvial fan is
603 initiated on the ND plain. The sigmoidal arrangement of clinofolds above the US in
604 ERT 8 is an example of this sequence. These clinofolds are formed from a lateral

605 accretion in the erosive entrenched channel, where migration of the sedimentary facies
606 proceeds according to Walther's law (Vera, 1994).

607 The sedimentary evolution on this fluvial plain varies depending on changes in
608 the local base level, which may be related to climatic factors (higher or lower moisture
609 contribution), glacial dynamics (retreat) or tectonics (greater subsidence or formation of
610 erosive scarps).

611 In ND clinofolds display offlap evolution (ERT 8, Fig. 6.) This type of evolution
612 is related to retrograde parasequences (Catuneanu, 2006). When maximum flooding is
613 reached the finest grain-size sediments are deposited (Catuneanu, 2006), and promote
614 low resistivities (Waxman and Smits, 1968) in ERT 8 (Fig. 6). This maximum flooding
615 surface (msf) is known as a transgressive surface (TS, Catuneanu, 2006), and its
616 identification is a key issue in sequence stratigraphy. Above this surface an
617 aggradational sequence starts, present here on the left-hand side of unit G2 in ERT 8
618 (Fig. 6), and progressing to the end of unit G1 in ERT 8 (Fig. 6).

619 In the southernmost sector of the depression, a clear paraconformity is
620 identified bringing resistive layers G1 and G2 into contact (ERT 1 and ERT 2). Here,
621 layer G2 displays an onlap contact with layer G3 (ERT 1 and ERT 2). A possible
622 explanation for this phenomenon is that tectonic subsidence facilitated the formation of
623 this angular discontinuity between G2 and G3, and at the same time preserved the
624 resistive layer G2 from erosion by G1. This interpretation is also supported by the fact
625 that the sedimentary fill in ERT 2 would have been conditioned by greater subsidence
626 on the western edge of the depression, forcing lateral accretion of the sigmoidal
627 clinofolds in this direction. The lateral accretion and correlative vertical onlap surfaces,
628 have no available space in ERT 8 and ERT 2, interpreted as a shallowing upward
629 sequence. This sequence occurs at the start of the ERT 8 erosive surface (US, Fig. 6)
630 which marks the end of the glacial obstruction in the ND. At that point alluvial fans
631 progress over the ND plain (Fig. 5). A shallowing-upward sequence may indicate an
632 accommodation lowering (Catuneanu, 2006), and thus a slight subsidence in the ND.

633

634 *4.5. Navamuño basin geometry and tectonic controls*

635

636 Taking into account the depth of the basement rock surface obtained in the
637 VES, ERT sections and MRS, the Navamuño basin infill thickness was calculated and
638 mapped (Fig. 9). These can be considered as minimum thickness values as the upper
639 limit of the basement was not reached in some zones and so they were assigned the
640 maximum penetration reached with the corresponding geophysical technique used.
641 The calculated sediment volume for the basin is approx. $3.8 \cdot 10^6 \text{ m}^3$, with a surface
642 area $129,694 \text{ m}^2$.

643 The isopach map shows a depocentre over 60 m deep in the south and centre
644 of the basin with a longitudinal NNE-SSW axis, parallel to the fractures defining the
645 western edge of the basin. The maximum thickness variation gradients are the W and
646 S borders, running NNE and ENE, respectively. These gradients, together with the
647 morphostructural map (Fig. 4) suggest a clear structural control of ND basin at both
648 edges by the NNE (PN Fault) and ENE (La Jara Fault) fracture families described in
649 Section 2.0, above. To the N the infill thickness decreases more gradually, while the
650 eastern boundary of the ND is more sharp (see onlap contacts in the right-hand side of
651 ERT 1 and ERT 8, Fig. 6), limited by the lateral moraine.

652 Considering the morphology of the sedimentary infill provided by the ERT
653 sections (Fig. 6, section 4.3), it was observed that unit G2 presents tilt in the centre of
654 the depression (ERT 2), while G1 presents sedimentary accommodation towards the
655 southern edge of the depression (ERT 7 and ERT 1). Geoelectrical layer G3 exhibits
656 clearly defined limits (in ERT 7 and ERT 1) and is clearly confined by the rock
657 substratum with structural limits in ERT 2 and ERT 8. All the above indicates a strong
658 tectonic component which configures the limits of the depression and affects its
659 sedimentary fill.

660

661 5. Discussion

662

663 The ND is one of the intermountain depressions forming the relief associated
664 with the Hervás-Candelario corridor-type valleys, one of the main morphostructures of
665 the W sector of the ICS. The evolution of these depressions is more complex than that
666 of the great sedimentary transpressional basins (De Vicente et al., 2011) and is
667 generally associated with NE-trending (NE-SW, NNE-SSW and N-S) strike-slip faults
668 (Santanach et al., 1988, 2005; Carrasco and Pedraza, 1991; Santanach, 1994;
669 Cabrera et al., 1996; Villamor et al., 1996; Alonso-Gavilán et al., 2004; Brum da
670 Silveira, et al., 2009). Two examples of this morphotectonic configuration are the Valle
671 del Jerte, 10 km to the east of the ND and linked to the AP fault (Carrasco and Pedraza
672 1991; Carrasco, 1997), and the series of depressions and platforms originating in the
673 NE trend of the HC and Galisteo strike-slip faults and their associated faults (Moreno,
674 1991), including the PN fault which is mainly responsible for the ND morphostructure
675 (Fig. 1).

676 Most of these ICS depressions occurring during the Paleogene /Lower Miocene,
677 correlative with the early stages of tectonic reactivation of present relief. In general, are
678 considered pull-apart type basins and in many cases aborted. Some of these were
679 reactivated during the Plio-Pleistocene and Quaternary, hosting new deposits which
680 present deformation structures catalogued as indicators of neotectonic activity (Brum
681 da Silveira, 1990; Carrasco et al., 1991; Capote et al., 1996; Villamor et al., 1996,
682 2012; De Vicente, 2009; De Vicente et al., 2011).

683 Geophysical data obtained from the ND show a relatively deep depression, with
684 sedimentary infill over 60 m thick. In the most surficial part of this fill (to depth 35 m) a
685 coarsening-upward sedimentary sequence is found corresponding to geoelectrical
686 layers G1 and G2, which from the available chronological data (Ruiz-Zapata et al.,
687 2011; Carrasco et al., 2015a; Turu et al., 2018) corresponds to Upper Pleistocene and
688 Holocene deposits. At depths of 35-45 m, the permeability and water content increase

689 considerably, but lower down both decrease rapidly to low permeability and low water
690 content by depth 90 m.

691 From a genetic viewpoint, the deepest aquifer (below 45 m depth) should be
692 associated with characteristic joints in rock with a weathering front above a depth of 60
693 m. The intermediate aquifer (at depths of 35-45 m) is the most productive and
694 coincides with geoelectrical layer G3. This layer must be coarse grained to be so
695 permeable and may correspond to arkosic deposits similar to described in depressions
696 associated with the AP fault (Brum da Silveira, 1990; Capote et al., 1996; Villamor et
697 al., 1996, 2012). In agreement with this data, the ND is similar to other small ICS
698 depressions, which in genetic and evolutionary terms are associated with strike-slip
699 faults and which, in some cases, have been interpreted as pull-apart type basins (Brum
700 da Silveira, 1990; Carrasco and Pedraza, 1991; Capote et al., 1996; Villamor et al.,
701 1996, 2012; De Vicente, 2009; De Vicente et al., 2011). The difference between the ND
702 depression and these others is that the recent (Quaternary) sediments here are 30-35
703 m thick, compared with the 10-15 m obtained in other ICS intermountain depressions.
704 Another distinctive characteristic of the ND, is that its evolution was linked to that of the
705 Cuerpo de Hombre glacier during the Glacial Period in this area (Upper Pleistocene;
706 ~MIS2), and the depression remained obstructed by moraines (and possibly by ice
707 during the Maximum Ice Extent, MIE) during the stages of glaciación.

708 In this context, both the subsidence dynamics and glacial-damming should be
709 considered determining factors in the recent infill process of the ND. Although the data
710 available from direct soundings is limited to the first 16 m of sediments (Carrasco et al.,
711 2015a, Turu et al., 2018), the chrono-evolutionary data obtained from the study of the
712 Cuerpo de Hombre paleoglacier (Carrasco et al., 2015b; Fig. 2) enable a chronological
713 succession to be established for how this depression evolved throughout the Upper
714 Pleistocene. The basin hydrologic regime was initially exorheic (drained by the Cuerpo
715 de Hombre river) and was later obstructed by the glacier. The obstruction process
716 started as ice-damming during the expansion stage of the glacier towards its MIE

717 (dated to 25.0 ± 1.3 ka; Carrasco et al., 2015b). Later, between 20.6 ± 2.5 ka and 17.8
718 ± 1.0 ka, the glacier built a wall-shaped lateral moraine (morainic Peripheral Deposits
719 and Principal Moraine from Carrasco et al., 2015b; PD-M and PM, respectively, Figs.
720 2A, 2C) and blocked the eastern boundary of ND. This interpretation is based on an
721 existing layer of alluvial fan deposits observed by Carrasco et al. (2015a) and Turu et
722 al. (2018). The age obtained for the bottom of the peatland above the alluvial fan
723 deposits is mid-Holocene (5160 ± 40 cal. yr BP, sample from 4.5 m depth, Ruiz-Zapata
724 et al., 2011).

725 The path of the Cuerpo de Hombre glacier was carefully considered to explain
726 the obstruction process. The current morphology of the Cuerpo de Hombre
727 paleoglacier displays a confined valley between the two major lateral moraines (PM
728 formations; Carrasco et al., 2015b). The right lateral moraine is attached to the bedrock
729 slopes and displays a constant NW-SE direction throughout its upper and middle
730 sector. The left lateral moraine also presents those same characteristics in its upper
731 sector. However, its middle sector changes markedly. From the area where the
732 moraine connects with the southern end of the ND, it is no longer confined in the
733 bedrock relief, and runs in a NNW-SSE direction turning after to NNE-SSW parallel to
734 PN fault (Figs. 2A, 4). These changes are maintained to the northern edge of the ND,
735 giving rise to the wall-shaped lateral moraine relief which forms the boundary between
736 the paleoglacier valley and the ND (Figs. 2A, 2C).

737 To explain the causes of this process, and most importantly, why the ice did not
738 expand on to the ND plain during the advance stage towards its glacial maximum,
739 three hypotheses can be established: (1) that the glacier in this zone was already in a
740 reach with non-expansive stagnant flow; (2) that there was an ice flow process adapted
741 to the morphological directives of a pre-glacial entrenched valley; and (3) that the ice
742 flow was conditioned by the tectonic structure of the depression and its neotectonic
743 evolution.

744 For the first hypothesis (1), from the data of this paleoglacier reconstruction
745 during its Maximum Ice Extent (MIE) provided by Carrasco et al. (2015b) and revised
746 and completed in this new research, the following can be established: (i) that the zone
747 connecting the glacier and the ND plain starts at altitude 1600 m asl, at a distance of
748 1.7 km from the Equilibrium-Line Altitude (ELA, estimated at altitude 1966 m asl), and
749 at 1.9 km from the glacier terminus which then was located at altitude 1260 m asl; and
750 (ii) that the thickness of the glacial tongue ice in this reach was 50 m, much thicker than
751 the ice in the stagnation zones close to glacier terminus or snout (with thickness 10-15
752 m). According to this data, the glacier tongue in this confluence zone was advancing in
753 its middle-upper reach, and could have expanded on to the ND plain.

754 For the second hypothesis (2) and according to surface geomorphological data,
755 there are no indicators of an existing pre-glacial entrenched valley which would have
756 channelled the ice. The valley of the Cuerpo de Hombre paleoglacier and the ND are
757 separated by the left lateral moraine of the PM formation, which originated a wall-
758 shaped lateral moraine accumulating directly on both plains (Figs. 2A, 2C). In the reach
759 where the paleoglacial valley and the ND appear connected, the plain of the ancient
760 glacier bed (defined on the bedrock or with a thin layer of subglacial sediments of less
761 than 2 m) and the ND plain are located at similar altitudes, presenting a gentle slope
762 from the former to the latter (1585-1520 m asl and 1520-1480 m asl; maximum and
763 minimum altitudes of the glacial valley bottom and the depression plain, respectively).
764 A possible interpretation is therefore that in the pre-glacial stage both plains formed a
765 single unit, later divided by the lateral moraine. Given the gradient between the two
766 plains, in the glacier advance stages towards its maximum (MIE), previous to the
767 development of the moraine (established from a first post-MIE retreat of the glacier,
768 Carrasco et al., 2015b), the ice would have expanded towards the ND.

769 For the third hypothesis (3) and given that ND is associated with multiple faults,
770 there is a solidly based argument for the existence of a tectonic structure in the relief
771 (hypothesis 3) which conditioned the path of the glacial tongue.

772 Many studies have highlighted the impact of tectonic activity on the shape,
773 location and path of glaciers, but also their capacity for adapting to tectonic structures
774 (Clark, 1967, 1972; Clark et al., 2003; Gillespie and Clark, 2011; Glasser and Ghiglione
775 2009; Cotton et al., 2014; Bathrellos et al., 2017). In studies of ICS glacial morphology
776 carried out to date (see here Pedraza and Carrasco, 2006), the general theory is that
777 the glacial basins occupied structurally controlled pre-glacial river valleys, but indicators
778 of the impact of tectonic structures or neotectonic activity on glacier dynamics have not
779 been detected. By interpreting the data obtained from near surface geophysical
780 research in ND, it can be deduced that the left lateral moraine of the Cuerpo de
781 Hombre paleoglacier fossilized a small raised block which may initially have acted as
782 the boundary between the glacier and the ND (Fig 8). In addition, and as previously
783 described, in the sedimentary infill a series of structures is also detected which may be
784 associated with neotectonic readjustment fault processes. According to these data, the
785 evolutive sequence of ND, and the effect of these processes on the path of the Cuerpo
786 de Hombre glacier, can be established as detailed below.

787 The depression obstruction process may have already been initiated by the
788 glacier tongue during its expansion phase towards the maximum extent (MIE) and was
789 later consolidated by the moraines. In this context, still supposing that the
790 sedimentation rate in the obstructed cuvette was very low or nil during the glacial
791 phase and the majority of the sediments detected by geophysics were all pre-glacier,
792 the 16 m of sediments of post-glacier fill detected with direct test bores (Carrasco et al.,
793 2015a; Turu et al., 2018) imply the elevation of the depression plain which: (1) must
794 have fossilized almost completely the formation of dispersed erratic boulders (PD-B;
795 Carrasco et al., 2015b, Fig. 2C); and (2) reveals that the base of the depression at the
796 onset of the glacial stage was some 15-30 m (extreme north and south, respectively)
797 lower than the floor of the glacial valley. Therefore, there was evidently a sufficient
798 longitudinal gradient of the terrain for the glacier to maintain its trajectory according to
799 the line of minimum slope. However, and as has been shown, after a slight advance

800 towards the depression, the glacier made an abrupt turn and came to a standstill at its
801 margin.

802 According to these data, it can be established that: (1) at that point the
803 configuration of the relief on the bottom of the depression must have been very
804 different and acted as a threshold controlling the direction of the ice flow; and (2) given
805 that the present base of the depression is at lower elevations than the floor of the
806 glacial valley and hosts the sediments corresponding to the obstruction process, the
807 only possible explanation for this process is the sinking of the depression during these
808 infill phases.

809 In relation to this sinking of the sedimentary depression, the suggestions are
810 that it was caused by gravitational movements (rotation platform) or by differential
811 movements between blocks limited by faults (tectonic readjustments). Both the data
812 provided by geophysics and the regional context data are sufficient arguments to
813 consider that the most probable process was the latter. The onlap contact shown in
814 geoelectrical layer G2 in ERT 1, and geoelectrical layer G1 in ERT 7, are indicators of
815 syntectonic sedimentation in ND (Fig. 6). The same occurs with geoelectrical layer G3
816 (ERT 1, ERT 3 and ERT 7) which is limited by high dip faults in ERT 2 and ERT 8 (Fig.
817 6). This rock threshold where the lateral moraine of the Cuerpo de Hombre
818 paleoglacier is found, corresponds to a raised block, and would have acted as a limit to
819 the path of the ice.

820 On the other hand, although the ICS and the centre of the Iberian Peninsula are
821 classified as zones of very low to moderate seismicity, (IGN, 2016), from analysing the
822 current river network of the ICS and other related areas in the central Iberian Meseta,
823 multiple indicators emerge of structural control, and of recent and current impact of
824 neotectonics with paleoseismic structures originating throughout the Pleistocene
825 (Pedraza, 1976; Carrasco et al., 1991; Silva et al., 1988; Pol et al., 1989; De Vicente et
826 al., 2007, 2011; Garzón et al., 2014). In this context, the proposed model for the route
827 followed by the paleoglacier can be considered coherent.

828

829 **6. Conclusions**

830

831 The ND is a ~30 ha pseudo-endorheic flat basin over granitic bedrock with
832 water ponding associated with the PN fault, a NNE-SSW trending Variscan strike-slip
833 fault correlated with the series of strike-slip faults described along the ICS. In the
834 geomorphological and geophysical studies carried out in this research, a sedimentary
835 infill over 60 m thick has been proven. This agrees with that established in recent
836 previous investigations and allows us to catalog the ND as the largest and deepest
837 sedimentary basin of the ICS associated with glacial processes (glacier obstruction or
838 overdeepening).

839 Geophysical surveys have been critical in identifying the infill depth in the
840 depression and the geometrical relationships existing in the rock substrata. This
841 information, together with that provided by the surficial geology and geomorphology,
842 supports the hypothesis that: (1) ND can be correlated with the small sedimentary
843 basins located along the Variscan strike-faults described in the Iberian Massif and
844 classified as an intermountain tectonic basin with primary origin due to a transtensional
845 process in the PN strike-slip fault during the stages of reactivation of the ICS
846 (Oligocene-lower Miocene); (2) part of the sedimentary infill is related to the
847 contribution made at the time by the Cuerpo de Hombre glacier meltwater through a
848 system of marginal flows; and (3) both in the path of the glacier and in the sedimentary
849 infill of the ND correlative to the glacial and postglacial stages, we have detected
850 indicators of neotectonic activity.

851 The Cuerpo de Hombre paleoglacier had a marked influence on sedimentary
852 evolution in the ND, as it was responsible for the shift from an exorheic hydrologic
853 regime to a semi-endorheic regime with ponding. From the available data, this process
854 took place during the maximum glacial advance stage (approx. 25.0 ± 1.3 ka BP) and
855 continued at least until silting-up occurred during the Holocene. Neotectonic

856 readjustment has continued from the last glacial cycle to the present day. However, the
857 post-glacial sedimentary infill in the depression presents a shallowing-upward
858 sequence, which is considered an indicator of decreasing subsidence.

859

860 **Acknowledgements**

861

862 This work was supported by the Spanish Ministry of Economy and Competitiveness
863 (Projects CGL2013-44076-P and CGL2016-78380-P). The authors also wish to
864 acknowledge the help and assistance of the Regional Environment Department (JCyL)
865 and the Local Authority in the village of Candelario. We also thank to the Editor and the
866 reviewers, for their helpful comments and constructive suggestions that greatly
867 improved this manuscript.

868

869 **References**

870

- 871 Abel-Schaad, D., Pulido, F., López-Sáez, J.A., Alba Sánchez, F., Nieto Lugilde, D.,
872 Franco Múgica, F., Pérez-Díaz, S., Ruiz Zapata, M.B., Gil García, M.J., Dorado
873 Valiño, M., 2014. Persistence of tree relicts in the Spanish Central System
874 through the Holocene. *Lazaroa* 35, 107-131.
- 875 Alonso-Gavilán, G., Armenteros, I., Carballeira, J., Corrochano, A., Huerta, P.,
876 Rodríguez, J. M., 2004. Cuencas cenozoicas del Macizo Ibérico. In Vera, J.A.
877 (Ed.), *Geología de España*. SGE-IGME. Madrid, Spain, pp. 581-584.
- 878 Anon, 1977. The description of rock masses for engineering purposes: Report by the
879 Geological Society Engineering Group Working Party. *Q. J. Eng. Geol.*
880 *Hydrogeol.* 10, 355-388.
- 881 Barker, R., 1992. A simple algorithm for electrical imaging of the subsurface. *First*
882 *Break* 10, 53 – 62.

883 Bathrellos, G., Skilodimou, H., Maroukian, H., 2017. The significance of tectonism in
884 the glaciations of Greece. Geological Society, London, Special Publications
885 433, 237-250.

886 Behroozmand, A.A., Keating, K., Auken, E., 2015. A Review of the Principles and
887 Applications of the NMR Technique for Near-Surface Characterization. Surv.
888 Geophys. 36, 27-85.

889 Bellido-Mulas, F. (Ed.), 2006. Mapa Geológico de Cabezuela del Valle, 1:50 000. Map
890 576. Instituto Geológico y Minero de España. Madrid, Spain. <http://www.igme.es>

891 Ber, A., 2009. Vertical stress of the pleistocene continental glaciers and its hypothetical
892 evidence in present relief of Northern Europe. Polish Geol. Inst. Spec. Pap. 25,
893 7–12.

894 Bhattacharya, P.K., Patra, H.P. (Eds.), 1968. Direct current geoelectric sounding,
895 principles and interpretation. Elsevier, Amsterdam, Netherlands.

896 Bobachev, A.A, Shevnin, V.A., Modin, I.N., 2003. IPI2WIN version 3.0.1e.
897 <http://geophys.geol.msu.ru/ipi2win.htm>.

898 Bordonau, J., 1992. Els Complexos glàcio-lacustres relacionats amb el darrer cicle
899 glacial als Pirineus. Ph.D. Thesis, Barcelona Univ., Spain.

900 Brum da Silveira, A., 1990. Neotectónica e Sismotectónica da Região Vidigueira–
901 Moura. Ph.D. Thesis, Univ. Lisboa, Portugal.

902 Brum da Silveira, A., Cabral, J., Perea, H., Ribeiro, A., 2009. Evidence for coupled
903 reverse and normal active faulting in W Iberia. The Vidigueira-Moura and
904 Alqueva faults (SE Portugal). Tectonophysics 474, 184–199.

905 Cabral, J., 1995. Neotectónica em Portugal Continental. Memórias do Instituto
906 Geológico e Mineiro 31, Lisboa, Portugal.

907 Cabral, J., 2012. Neotectonics of mainland Portugal: state of the art and future
908 perspectives. J. Iber. Geol. 38, 71–84.

909 Cabrera, L., Ferrús, B., Sáez, A., Santanach P., Bacelar J., 1996. Onshore Cenozoic
910 strike-slip basins in NW Spain. In: Friend, P. F., Dabrio, C.J. (Eds), Tertiary
911 Basins of Spain. Cambridge Univ. Press, New York, USA, pp. 247-254.

912 Capote, R., Villamor, P., Tsige, M., 1996. La tectónica alpina de la Falla de Alentejo-
913 Plasencia (Macizo Hespérico). *Geogaceta* 20, 921–924.

914 Carrasco, R.M., 1997. Estudio Geomorfológico del Valle del Jerte (Sistema Central
915 Español): secuencia de procesos y dinámica morfogenética actual. Ph.D.
916 Thesis, Complutense Univ. Madrid, Spain.

917 Carrasco, R.M., Pedraza, J., 1991. Historia morfodinámica de la Falla de Plasencia en
918 el Valle del Jerte. In: Actas de Gredos, V Jornadas de Verano de La Sierra de
919 Gredos, *Boletín Universitario* 11, UNED, Ávila, Spain, pp. 17–30.

920 Carrasco, R.M., Pedraza, J., Rubio, J.C., 1991. Actividad neotectónica cuaternaria en
921 el Valle del Jerte. *Cuaternario y Geomorfología* 5, 15–25.

922 Carrasco, R.M., Pedraza, J., Domínguez-Villar, D., Willebring, J., Razola, L.,
923 Edwards, L., Wang, Y., Fairchild, I.J., Baker, A., Ruiz-Zapata, M.B., Centeno, J.,
924 2009. Chronology and causes of the Last Glacial Maximum in Spanish Central
925 System: the project methodology. 7th International Conference on
926 Geomorphology (ANZIAG). Conference Abstracts, Melbourne, Australia.

927 Carrasco, R.M., Pedraza, J., Domínguez-Villar, D., Villa, J., Willenbring, J.K., 2013.
928 The plateau glacier in the Sierra de Béjar (Iberian Central System) during its
929 maximum extent. Reconstruction and chronology. *Geomorphology* 196, 83–93.

930 Carrasco, R.M., Sánchez, J., Muñoz-Martín, A., Pedraza, J., Olaiz, A.J., Ruiz-Zapata,
931 B., Abel-Schaad, D., Merlo, O., Domínguez-Villar, D., 2015a. Caracterización
932 de la geometría de la depresión de Navamuño (Sistema Central Español)
933 aplicando técnicas geofísicas. *Geogaceta* 57, 39–42.

934 Carrasco, R.M., Pedraza, J., Domínguez-Villar, D., Willenbring, J.K., Villa, J., 2015b.
935 Sequence and chronology of the Cuerpo de Hombre paleoglacier (Iberian
936 Central System) during the last glacial cycle. *Quat. Sci. Rev.* 129, 163–177.

937 Catuneanu, O., 2006. Principles of Sequence Stratigraphy. Elsevier Science,
938 Amsterdam, Netherlands.

939 Centeno, J.D., Brell, J.M., 1987. Características de las alteraciones de las Sierras de
940 Guadarrama y Malagon (Sistema Central Español). Cuaderno Lab. Xeológico
941 de Laxe 12, 79-87.

942 Clark, M.M., 1967. Pleistocene glaciation of the drainage of the West Walker River,
943 Sierra Nevada, California. Ph.D. Dissertation, Stanford, Stanford University,
944 USA.

945 Clark, M.M., 1972. Range-front faulting: cause of anomalous relationships among
946 moraines of the eastern slope of the Sierra Nevada, California. Geol. Soc. Am.
947 Abstr. Programs 4, 137.

948 Clark, D., Gillespie, A.R., Clark, M.M., Burke, R.M., 2003. Mountain glaciations of the
949 Sierra Nevada. In: Easterbrook, D.J. (Ed.), Quaternary Geology of the United
950 States. International Quaternary Association: INQUA 2003. Field Guide Volume.
951 XVI INQUA Congress. Desert Research Institute, Reno, USA, pp. 287–312.

952 Cotton, M.M., Bruhn, R.L., Sauber, J., Burgess, E., Forster, R.R., 2014. Ice surface
953 morphology and flow on Malaspina Glacier, Alaska: Implications for regional
954 tectonics in the Saint Elias orogen. Tectonics 33, 558–595.

955 Dearman, W.R., 1978. Weathering classification in the characterization of rock: a
956 revision. Bull. Int. Assoc. Eng. Geol. 18, 123–128.

957 De Brujne, C.H., Andriessen, P.A.M., 2002. Far field effects of Alpine plate tectonism in
958 the Iberian microplate recorded by fault-related denudation in the Spanish
959 central system. Tectonophysics 349, 161-184.

960 Descloitres, M., Ruiz, L., Sekhar, M., Legchenko, A., Braun, J.J., Mohan Kumar, M.S.,
961 Subramanian, S., 2008. Characterization of seasonal local recharge using
962 electrical resistivity tomography and magnetic resonance sounding. Hydrol.
963 Process. 22, 384–394.

964 De Vicente, G., 2009. Partición de la deformación cenozoica intraplaca en el Sistema
965 Central. *Geogaceta* 46, 23-26.

966 De Vicente, G., Vegas, R., 2009. Large-scale distributed deformation controlled
967 topography along the western Africa–Eurasia limit: tectonic constraints.
968 *Tectonophysics* 474, 124-143.

969 De Vicente, G., Vegas, R., Muñoz Martín, A., Silva, P.G., Andriessen, P., Cloetingh, S.,
970 González Casado, J.M., Van Wees, J.D., Álvarez, J., Carbó, A., Olaiz, A., 2007.
971 Cenozoic thick-skinned deformation and topography evolution of the Spanish
972 Central System. *Glob. Planet. Change* 58, 335–381.

973 De Vicente, G., Cloetingh, S., Van Wees, J.D., Cunha, P.P., 2011. Tectonic
974 classification of Cenozoic Iberian foreland basins. *Tectonophysics* 502, 38–61.

975 Foroutan, M., Vilanova, S., Heleno, S., Pinto, L., Far, A.S., Falcao-Flor, A., Canora, C.,
976 Pina, P., Vieira, G., Fonseca, J., 2016. New evidence for large earthquakes in
977 mainland Portugal: paleoseismology of the Lower Tagus Valley fault. 35th
978 General Assembly of the European Seismological Commission. ESC2016-489-
979 1.

980 Franco-Múgica, F., 1995. Estudio palinológico de turberas holocenas en el Sistema
981 Central: reconstrucción paisajística y acción antrópica. Ph.D. Thesis, Univ.
982 Autónoma. Madrid, Spain.

983 Garate, J., Martin-Davila, J., Khazaradze, G., Echeverria, A., Asensio, E., Gil, A.J., de
984 Lacy, M.C., Armenteros, J.A., Ruiz, A.M., Gallastegui, J., Alvarez-Lobato, F.,
985 Ayala, C., Rodríguez-Caderot, G., Galindo-Zaldívar, J., Rimi, A., Harnafi, M.,
986 2015. Topo-Iberia project: CGPS crustal velocity field in the Iberian Peninsula
987 and Morocco. *GPS Solutions*, 19, 287-295.

988 Garzón, G., Garrote, J., Tejero, R., 2014. La integración de la red fluvial del margen
989 norte del río Tajo. El papel de las depresiones cenozoicas. In: Schnabel, S.,
990 Gómez-Gutiérrez, A. (Eds.), *Avances de la Geomorfología en España 2012-*
991 *2014*. Universidad de Extremadura, SEG, Cáceres, Spain, pp. 393-396.

992 Génova, M., Gómez-Manzanaque, F., Martínez-García, F., Postigo-Mijarra, J.M., 2016.
993 Early Holocene vegetation in the Ayllón Massif (Central System Range, Spain)
994 based on macroremains. A paleoecological approach. *Palaeogeogr.*
995 *Palaeoclimatol. Palaeoecol.* 441, 811–822.

996 Gillespie, A.R., Clark, D.H., 2011. Glaciations of the Sierra Nevada, California, USA. In:
997 Ehlers, J., Gibbard, P.L., Hugges, P.D. (Eds.), *Quaternary Glaciations – Extent*
998 *and Chronology*. Elsevier, Amsterdam, Netherlands, pp. 447-462.

999 Glasser, N.F., Ghiglione, M.C., 2009. Structural, tectonic and glaciological controls on
1000 the evolution of fjord landscapes. *Geomorphology* 105, 291–302.

1001 Grunewald, E., Knight, R., 2011. The effect of pore size and magnetic susceptibility on
1002 the surface NMR relaxation parameter T_2^* . *Near Surface Geophysics* 9, 169-
1003 178.

1004 Hausmann, J., Steinell, H., Kreck, M., Werban, U., Vienken, T., Dietrich, P., 2013. Two-
1005 dimensional geomorphological characterization of a filled abandoned meander
1006 using geophysical methods and soil sampling. *Geomorphology* 201, 335–343.

1007 Herrero-Simón, R., 2003. Anasim code V.6.0; Internal software from the Nuclear and
1008 Physics Engineering Department of the Universitat Politècnica de Catalunya
1009 (UPC), Terrassa, Spain.

1010 Herrero-Simón, R., 2007. Simusism code V.2.0; Internal software from the Nuclear and
1011 Physics Engineering Department of the Universitat Politècnica de Catalunya
1012 (UPC), Terrassa, Spain.

1013 Hertrich, M., 2008. Imaging of groundwater with nuclear magnetic resonance. *Prog.*
1014 *Nucl. Magn. Reson. Spectrosc.* 53, 227–248.

1015 IGN, 2016. Mapas de sismicidad y peligrosidad. Instituto Geográfico Nacional, Spain.
1016 <http://www.ign.es>

1017 Jalut, G., Turu, V., Dedoubat, J.J., Otto, T., Ezquerro, J., Fontugne, M., Belet, J.M.,
1018 Bonnet, L., de Celis, A.G., Redondo-Vega, J.M., Vidal-Romaní, J.R., Santos, L.,
1019 2010. Palaeoenvironmental studies in NW Iberia (Cantabrian range): Vegetation

1020 history and synthetic approach of the last deglaciation phases in the western
1021 Mediterranean. *Palaeogeogr. Palaeoclimatol. Palaeoecol.* 297, 330–350.

1022 Lange, G., Yaramanci, U., Meyer, R., 2007. Surface Nuclear Magnetic Resonance. In:
1023 Knödel, K., Lange, G., Voigt, HJ. (Eds.), *Environmental Geology*. Springer
1024 Berlin Heidelberg, Germany, pp. 403–430.

1025 Legchenko, A.V., Shushakov, O.A., 1998. Inversion of surface NMR data. *Geophysics*,
1026 63 (1), 75-84.

1027 Loke, M.H., Barker, R.D., 1996. Rapid least-squares inversion of apparent resistivity
1028 pseudosections by a quasi-Newton method. *Geophys. Prospect.* 44, 131-152.

1029 Loke, M.H., Wilkinson, P.B, Chambers, J.E., 2010. Parallel computation of optimized
1030 arrays for 2-D electrical imaging surveys. *Geophys. J. Int.* 183, 1302-1315.

1031 López-Sáez, J.A., Abel-Schaad, D., Pérez-Díaz, S., Blanco-González, A., Alba-
1032 Sánchez, F., Dorado, M., Ruiz-Zapata, B., Gil-García, M.J., Gómez-González,
1033 C., Franco-Múgica, F., 2014. Vegetation history, climate and human impact in
1034 the Spanish Central System over the last 9000 years. *Quat. Int.* 353, 98–122.

1035 López-Sáez, J.A., Abel-Schaad, D., Robles-López, S., Pérez-Díaz, S., Alba-Sánchez,
1036 F., Nieto-Lugilde, D., 2016. Landscape dynamics and human impact on high-
1037 mountain woodlands in the western Spanish Central System during the last
1038 three millennia. *JASREP* 9, 203–218.

1039 Maillet, R., 1947. The fundamental equations of electrical prospecting. *Geophysics* 12,
1040 529-556.

1041 Mejías, M., Plata, J., 2007. General concepts in Hydrogeology and Geophysics related
1042 to MRS. *Bol. Geol. y Min.* 118, 423–440.

1043 Mendes-Victor, L., Oliveira, C.S., Azevedo, J., Ribeiro, A. (Eds.), 2009. *The 1755*
1044 *Lisbon Earthquake: Revisited*. Springer, Netherlands.

1045 Molina-Ballesteros, E., García-González, M.T., Espejo, R., 1991. Study of
1046 Paleoweathering on the Spanish Hercynian basement Montes de Toledo
1047 (Central Spain). *Catena* 18, 345-354.

- 1048 Molina-Ballesteros, E., García-Talegón, J., Vicente-Hernández, M. A., 1994. Las
1049 paleoalteraciones sobre el zócalo hercínico ibérico. Aproximación a una
1050 interpretación regional a partir de perfiles españoles. Cuaderno Lab. Xeológico
1051 de Laxe 19, 261-271.
- 1052 Molina-Ballesteros, E., García-Talegón, J., Vicente-Hernández, M.A., 1997.
1053 Palaeoweathering profiles developed on the Iberian Hercynian Basement and
1054 their relationship to the oldest Tertiary surface in central and western Spain.
1055 Geol. Soc. London, Spec. Publ. 120, 175–185.
- 1056 Moreno, F., 1991. Superficies de erosión y tectónica neógena en el extremo occidental
1057 del Sistema Central español. Geogaceta 9, 47-50.
- 1058 Muñoz Martín, A., De Vicente, G., Olaiz, A., Antón, L., Vegas, R., Granja, J.L., 2012.
1059 Mapa de esfuerzos activos en línea de la Península Ibérica a partir de
1060 Mecanismos Focales calculados desde el Tensor de Momento Sísmico.
1061 Geotemas 13, 1-4.
- 1062 Olaiz, A.J., Muñoz-Martín, A., De Vicente, G. Vegas, R., Cloeting, S., 2009. Oblique
1063 strain partitioning and transpression on an inverted rift: The Castilian Branch of
1064 the Iberian Chain. Tectonophysics 470, 224-242.
- 1065 Olvmo, M., Johansson, M., 2002. The significance of rock structure, lithology and pre-
1066 glacial deep weathering for the shape of intermediate-scale glacial erosional
1067 landforms. Earth Surf. Process. Landforms 27, 251–268.
- 1068 Palmer, D., 1980. The generalized reciprocal method of seismic refraction
1069 interpretation. Society of Exploration Geophysicists, Tulsa, USA.
- 1070 Pedraza, J., 1976. Algunos procesos morfogenéticos recientes en el valle del río
1071 Alberche (Sistema Central Español). La depresión de Aldea del Fresno-
1072 Almorox. Bol. Geol. y Min. 87, 1–12.
- 1073 Pedraza, J., 1994. Sistema Central. In: Gutiérrez Elorza, M. (Ed.), Geomorfología de
1074 España. Rueda, Spain, pp. 63–100.

- 1075 Pedraza, J., 2012. Late Pleistocene glacial evolutionary stages in the Spanish Central
1076 System. *Quat. Int.* 279–280, 371–372.
- 1077 Pedraza, J., Carrasco, R. M., 2006, El glaciarismo pleistoceno del Sistema Central.
1078 *AEPECT*, 13 (3), 278-288.
- 1079 Pedraza, J., Carrasco, R.M., Domínguez-Villar, D., Villa, J., 2013. Late Pleistocene
1080 glacial evolutionary stages in the Gredos Mountains (Iberian Central System).
1081 *Quat. Int.* 302, 88–100.
- 1082 Pèlachs, A., Julià, R., Pérez-Obiol, R., Burjachs, F., Expósito, I., Yll, R., Vizcaino, A.,
1083 Turu, V., Soriano, J.M., 2011. Dades paleoambientals del complex
1084 glaciolacustre de l'estany de Burg durant el Tardiglacial (Vall Ferrera, Pallars
1085 Sobirà). In: Turu, V. and Constante, A. (Eds.), *Simposio de Glaciarismo: El*
1086 *Cuaternario en España y áreas afines, Avances en 2011*. Fundació Marcel
1087 Chevalier- AEQUA. Andorra la Vella, pp. 40–50.
- 1088 Pellicer, X.M., Zarroca, M., Gibson, P., 2012. Time-lapse resistivity analysis of
1089 Quaternary sediments in the Midlands of Ireland. *J. Appl. Geophys.* 82, 46–58.
- 1090 Plata, J.L., Rubio, F.M., 2008. The use of MRS in the determination of hydraulic
1091 transmissivity: The case of alluvial aquifers. *J. Appl. Geophys.* 66, 128–139.
- 1092 Pol, C., Sánchez del Corral, A., Carballeira, J., 1989. Neotectónica en la cuenca del
1093 alto Tormes (Sistema Central, Ávila): Influencia en la morfología fluvial.
1094 *Geogaceta* 6, 90–94.
- 1095 Prasicek, G., Larsen, I.J., Montgomery, D.R., 2015. Tectonic control on the persistence
1096 of glacially sculpted topography. *Nat. Commun.* 6, 8028.
- 1097 Reynolds, J.M., 2011. *An Introduction to Applied and Environmental Geophysics*.
1098 Wiley-Blackwell, Chichester, UK.
- 1099 Rodríguez Fernández, L.R.; Oliveira, J.T. (Ed.), 2015. *Mapa Geológico de la Península*
1100 *Ibérica, Baleares y Canarias a escala 1:1.000.000*. Instituto Geológico y Minero
1101 de España. Madrid, Spain. <http://www.igme.es>

1102 Rubiales, J.M., García-Amorena, I., Génova, M., Gómez Manzaneque, F., Morla, C.,
1103 2007. The Holocene history of highland pine forests in a submediterranean
1104 mountain: the case of Gredos mountain range (Iberian Central range, Spain).
1105 Quat. Sci. Rev. 26, 1759–1770.

1106 Rubio, J.C., 1990. Geomorfología y Cuaternario de las sierras de la Nava y Béjar
1107 (Sistema Central Español). PhD Thesis, Complutense Univ., Madrid, Spain.

1108 Ruiz-Zapata, M.B., Carrasco, R.M., Gil-García, M.J., Pedraza, J., Razola, L.,
1109 Domínguez- Villar, D., Gallardo, J.L., 2011. Dinámica de la vegetación durante
1110 el Holoceno en la Sierra de Gredos (Sistema Central Español). Bol. R. Soc.
1111 Esp. Hist. Nat. 105, 109-123.

1112 Salazar-Rincón, A., Mata-Campo, P., Rico-Herrero, M.T., Valero-Garcés, B.L., Oliva-
1113 Urcia, B., Ibarra, P., Rubio, F.M., 2013. El paleolago de La Larri (Valle de
1114 Pineta, Pirineos): Significado en el contexto del último máximo glaciar en el
1115 Pirineo. Cuadernos de Investigación Geográfica 39, 97-116.

1116 Santanach, P., 1994. Las cuencas terciarias gallegas en la terminación occidental de
1117 los relieves pirenaicos. Cuad. Lab. Xeol. Laxe 19, 57-71.

1118 Santanach, P., Baltuille, J.M., Cabrera, L., Monge, C., Sáez, A., Vidal-Romaní, J.R.
1119 1988. Cuencas terciarias gallegas relacionadas con corredores de falla
1120 direccionales. II Congreso Geológico de España, IGME, Granada, Spain, pp.
1121 123-133.

1122 Santanach, P., Ferrús, B., Cabrera, L., Sáez, A., 2005. Origin of a restraining bend in
1123 an evolving strike-slip system: The Cenozoic As Pontes basin (NW Spain).
1124 Geol. Acta 3, 225–239.

1125 Sanz-Donaire, J.J., 1979. El Corredor de Béjar. Instituto de Geografía aplicada. CSIC,
1126 Madrid, Spain.

1127 Schrott, L., Hördt, A., Dikau, R. (Eds.), 2003. Geophysical applications in
1128 geomorphology. Zeitschr. f. Geomorphologie Supplementbände, 132, 190S.

- 1129 Sheehan J.R., Doll W.E., Mandell W.A., 2005. An evaluation of methods and available
1130 software for seismic refraction tomography analysis. *J. Environ. Eng.*
1131 *Geophysics*. 10, 21–34.
- 1132 Sheriff, E.R., Geldart, L.P., 1991. Exploración sísmológica. Volumen II. Procedimientos
1133 e interpretación de datos. Limusa, México.
- 1134 Shushakov, O.A., Legchenko, A.V., 1994. Groundwater proton magnetic resonance in
1135 the horizontally stratified media of different electrical conductivity. *Geol.*
1136 *Geophys.* 35, 130-136 (in Russian).
- 1137 Silva, P., Goy, J.L., Zazo, C., 1988. Evolución Geomorfológica de la confluencia de los
1138 ríos Jarama y Tajuña durante el cuaternario (Cuenca de Madrid, España).
1139 *Cuaternario y Geomorfología* 2, 125–133.
- 1140 Turu, V., 1999. Aplicación de diferentes técnicas geofísicas y geomecánicas para el
1141 diseño de una prospección hidrogeológica de la cubeta de Andorra, (Pirineo
1142 Oriental): implicaciones paleohidrogeológicas en el contexto glacial andorrano.
1143 In: *Actualidad de las técnicas geofísicas aplicadas en hidrogeología*. ITGE-
1144 IGME, Madrid, Spain, pp. 203-210.
- 1145 Turu, V., 2012. Surface NMR survey on Hansbreen Glacier, Hornsund, SW
1146 Spitsbergen. *Landform Analysis* 21, 57-74.
- 1147 Turu, V., Boulton G. S., Ros X., Peña-Monne J. L., Marti-Bono C., Bordonau J.,
1148 Serrano-Cañadas E., Sancho-Marcén, C., Constante-Orrios A., Pous J.,
1149 Gonzalez-Trueba J. J., Palomar J., Herrero-Simón, R., García-Ruiz, J. M.,
1150 2007. Structure des grands bassins glaciaires dans le nord de la Péninsule
1151 Ibérique: comparaison entre les vallées d'Andorre (Pyrénées Orientales), du
1152 Gállego (Pyrénées Centrales) et du Trueba (Chaîne Cantabrique). *Quaternaire*
1153 18, 309–325.
- 1154 Turu, V., Ventura, J., Ros, X., Pélachs, A., Vizcaino, A., Soriano, J.M., 2011.
1155 Geomorfologia glacial del tram final de la Noguera Pallaresa i riu Flamicell (Els
1156 Pallars). In: In: Turu, V., Constante-Orrios, A. (Eds.), *Simposio de glaciari-*

1157 El Cuaternario en España y áreas afines, avances en 2011. Fundació Marcel
1158 Chevalier-AEQUA, Andorra la Vella, pp. 37-43.

1159 Turu, V., Calvet, M., Bordonau, J., Gunnell, Y., Delmas, M., Vilaplana, J.M., Jalut, G.,
1160 2017. Did Pyrenean glaciers dance to the beat of global climatic events?
1161 Evidence from the Würmian sequence stratigraphy of an ice-dammed
1162 palaeolake depocentre in Andorra. Geol. Soc. London, Spec. Publ. 433, 111-
1163 136.

1164 Turu, V., Carrasco, R.M., Pedraza, J., Ros, X., Ruiz-Zapata, B., Soriano-López, J.M.,
1165 Mur-Cacaho, E., Pélachs-Mañosa, A., Muñoz-Martín, A., Sánchez, J.,
1166 Echeverría-Moreno, A., 2018. Late glacial and post-glacial deposits of the
1167 Navamuño peatbog (Iberian Central System): Chronology and
1168 paleoenvironmental implications. Quat. Int. 470, 82-95.

1169 Udías, A., López Arroyo, A., 2009. The Lisbon Earthquake of 1755 in Spanish
1170 Contemporary Authors. In Mendes-Victor, L., Oliveira, C.S., Azevedo, J.,
1171 Ribeiro, A. (Eds.), The 1755 Lisbon Earthquake: Revisited. Springer, Dordrecht,
1172 Netherlands, pp. 7-24.

1173 Vail, P.R., Colin, J.P., du Chene, R.J., Kuchly, J., Mediavilla, F., Trifilieff, V., 1987. La
1174 stratigraphie sequentielle et son application aux correlations
1175 chronostratigraphiques dans le Jurassique du bassin de Paris. B. Soc. Geol. Fr. 8,
1176 1301-1321.

1177 Vázquez, J.T., Vegas, R., Barranco, L.M., 1987. Rasgos morfológicos de la depresión
1178 del Burguillo (Sistema Central Español) y su relación con deformaciones
1179 recientes. Cuaternario y Geomorfología 1, 295–308.

1180 Vera, J.A., 1994. Estratigrafía, Principios y Métodos. Ed. Rueda, Madrid, Spain.

1181 Vilaplana, J.M., Casas, A., 1983. Las cubetas de sobreexcavación glacial de Bono y
1182 Barruera (Alta Ribagorça, Pirineo Central). Cuad. Lab. Xeol. de Laxe 6, 283-
1183 309.

- 1184 Villamor, P., Capote, R., Tsige, M., 1996. Actividad neotectónica de la Falla de
1185 Alentejo-Plasencia en Extremadura (Macio Hespérico). *Geogaceta* 20, 925–
1186 928.
- 1187 Villamor, P., Capote, R., Stirling, M.W., Tsige, M., Berryman, K.R., Martínez-Díaz, J.J.,
1188 Martín-González, F., 2012. Contribution of active faults in the intraplate area of
1189 Iberia to seismic hazard: The Alentejo-Plasencia Fault. *J. Iber. Geol.* 38, 85–
1190 111.
- 1191 Villaseca, C., 2003. Sobre el origen del batolito granítico del Sistema Central Español.
1192 *Bol. R. Soc. Esp. Hist. Nat.* 98, 23-39.
- 1193 Villaseca, C., Barbero, I., Herreros, V., 1999. A re-examination of the typology of
1194 peraluminous granite-types in intracontinental orogenic belts. *Trans. R. Soc.*
1195 *Edinb. Earth Sci.* 89, 113-119.
- 1196 Vouillamoz, J.M., Baltassat, J.M., Girard, J.F., Plata, J., Legchenko, A., 2007.
1197 Hydrogeological experience in the use of MRS. *Bol. Geol. y Min.* 118, 531–550.
- 1198 Walsh, D. O., 2008. Multi-channel surface NMR instrumentation and software for
1199 1D/2D groundwater investigations. *J. Appl. Geophys.* 66, 140-150.
- 1200 Watanabe, T., Matsuoka, T., Ashida, Y., 1999. Seismic traveltime tomography using
1201 Fresnel volume approach. *SEG Technical Program Expanded Abstracts 1999*,
1202 1402-1405.
- 1203 Waxman, M.H., Smits, L.J.M., 1968. Electrical conductivities in oil-bearing shaly sands.
1204 *SPE Journal* 8, 107–122.
- 1205 Weichmann, P.B., Lavelly, E.M., Ritzwoller, M.H., 2000. Theory of surface nuclear
1206 magnetic resonance with application to geophysical imaging problems. *Phys.*
1207 *Rev. E.* 62, 1290–1312.
- 1208 Yamakawa, Y., Kosugi, K., Masaoka, N., Sumida, J., Tani, M., Mizuyama, T., 2012.
1209 Combined geophysical methods for detecting soil thickness distribution on a
1210 weathered granitic hillslope. *Geomorphology* 145-146, 56–69.

- 1211 Yanites, B.J., Ehlers, T.A., 2012. Global climate and tectonic controls on the
1212 denudation of glaciated mountains. *Earth Planet. Sci. Lett.* 325-326, 63–75.
- 1213 Yaramanci, U., 2000. Surface Nuclear Magnetic Resonance (SNMR) - A new method
1214 for exploration of ground water and aquifer properties. *Ann. Di Geofis.* 43, 1159-
1215 1175.
- 1216 Zohdy, A.A.R., 1989. A new method for automatic interpretation of Schlumberger and
1217 Wenner sounding curves. *Geophysics* 54, 244–253.
- 1218

1219 **Figure captions**

1220

1221 Fig. 1. Geological location of the study area. Geological diagram based on the *Mapa*
1222 *geológico de la Península Ibérica, Baleares y Canarias*. Scale 1: 1.000.000 (Rodríguez
1223 Fernández and Oliveira, 2015).

1224

1225 Fig. 2. A) Stages of retreat in Cuerpo de Hombre paleo-glacier and chronologies ka BP
1226 (based on Carrasco et al., 2015b). 3D image of the Navamuño Depression and Cuerpo
1227 de Hombre paleoglacier using ArcScene 10.4 and PNOA-2014 orthophoto
1228 (<http://www.ign.es>). B) General view of the Navamuño Depression photographed from
1229 its SW boundary facing NE. C) Panoramic view of the Cuerpo de Hombre valley and
1230 Navamuño depression. Green arrow indicate glacier path. Letters indicate the
1231 morphostratigraphic formations (Carrasco et al., 2015b): PD peripheral deposits (B-
1232 boulders and M-moraine); PM principal moraine; ID internal deposits (M1 to M4,
1233 recessional moraines).

1234

1235 Fig. 3. A) Location of field work carried out in the Navamuño Depression (image: DTM5
1236 m, <http://www.ign.es>). B) Seismic array deployed in the depression distal zone. C)
1237 MRS1 data collection in the centre of the peat bog. D) Profile ERT9 transversal to the
1238 depression and drawn perpendicular to the Cuerpo de Hombre paleoglacier lateral
1239 moraine.

1240

1241 Fig. 4. Fracture network associated with Navamuño tectonic depression.

1242

1243 Fig. 5. Electrical resistivity curves from Vertical Electrical Sounding data. Main
1244 resistivity layers (G1 to G3). Layer G1 corresponds to the shallower geoelectrical layer.
1245 Resistivity from layer G2 is quite variable in resistivity and is interpreted as
1246 corresponding to alluvial fan and floodplain deposits. Layer G3 corresponds to older

1247 sedimentary deposits present in deeper positions in the Navamuño depression, but the
1248 G3 geoelectrical layer is also perched beneath the same deposits. Resistivity
1249 anomalies, as in VES 8 and VES 7, occur when electrodes sharply cross basement
1250 and sedimentary deposits. If this is not the case and a transition exists between granite
1251 and the sedimentary infill, then it is difficult to identify the depth of the basement (VES 4
1252 and VES 6).

1253

1254 Fig. 6. ERT tomography and geological interpretation including VES and MRS
1255 positions.

1256

1257 Fig. 7. Magnetic Resonance Sounding data and inversion results. Solid line-squares:
1258 groundwater signal. Circles: electromagnetic noise.

1259

1260 Fig. 8. Interpretation of the seismic profile using P-wave velocity and thickness of
1261 deducted seismic units. Seismic velocity is inversely related to the slope of the linear
1262 regression. Anomalies in PS1 and PS3 time-distance graphics are related with vertical
1263 jumps (erosive surfaces or sharp facies changes). All numbers that overlap geological
1264 materials are seismic velocities (in meters per second). NRZ = Non-Refraction Zone
1265 from an over-pressurized aquifer. Refractions coming from a denser terrain on PS1 (D)
1266 are interpreted as being related to the bedrock basement. On the opposite side of the
1267 profile (PS4), bedrock basement is located below the moraine at shallow depth.

1268

1269 Fig. 9. Isopach map of the Navamuño Basin infill obtained from interpolating the
1270 thicknesses calculated in the geophysical data. In the zones where the upper limit of
1271 the granitic basement was not reached, a minimum thickness has been assigned,
1272 equal to the penetration reached with each technique. The infill isopachs are
1273 superimposed on the LiDAR topography produced by the IGN. The interpolation has
1274 been carried out using kriging at grid resolution of 5 m with a linear variogram, based

1275 on all the data. The grid was then blanked outside the zone with zero thickness. To
1276 improve the isopach map, we have used the cartographic boundary of the basin infill,
1277 adding these data with zero thickness to the thickness values calculated using
1278 geophysical methods.

Table 1. Topographic parameters of the central point of the Magnetic Resonance Sounding (MRS) profiles.

	MRS 1	MRS 2
Latitude (DD)	40.321147	40.321109
Longitude (DD)	-5.778729	-5.778485
Elevation (m asl)	1505	1505
Loop type	Square	Square
Loop side	30 m	60 m
Depth	45 m	90 m
Geomorphology	Peat bog	Peat bog

DD: decimal degrees; m asl: metres above sea level

Table 2. Results of interpreting Vertical Electrical Soundings. Error of fit (RMS) between the real and apparent resistivity model varies from 3.5% - 10.8%. Individually, each layer presents thickness and resistivity equivalences regarding to the proposed value. Every equivalence ratio in thickness (Kh) and resistivity (Kro) is averaged ($\Sigma K/2$) when differences are small ($Kh-Kro < 1$), but for larger values ($Kh-Kro \geq 1$), as for VES 6 and VES 7, equivalences are shown separately (by thickness and resistivity). The third layer (H3, Rho_3) may present significant resistivity equivalences for VES 6. In VES 8 and VES 7 layer 4 is the most equivalent regarding resistivities (Kh-Kro ratios of 10 or higher). Nevertheless, equivalence thickness also exist in VES 7.

	VES 1	VES 2	VES 3	VES 4	VES 5	VES 6	VES 7	VES 8	VES 9
Lat. (DD)	40.317341	40.317188	40.317116	40.323233	40.321486	40.319769	40.318432	40.318500	40.321286
Long. (DD)	-5.778121	-5.780374	-5.776150	-5.776939	-5.778444	-5.779021	-5.779578	-5.779758	-5.778895
Elev. (m asl)	1518	1509	1600	1498	1505	1506	1505	1505	1503
AB disposition	ENE-WSW	E - W	NNW-SSE	NNW-SSE	NNW-SSE	WNW-ESE	NW-SE	NE-SW	N-S
AB/2 (m)	56	32	100	75	133	133	133	133	75
H1 (m)	0.9	1	1	0.6	0.6	1	1	1.3	0.9
Rho_1 (Ωm)	1274	9873	27179	1755	4800	1801	1618	1921	1159
$\Sigma K/2$	1.2	1.15	2.43	1.87	1.2	1.08	1.08	1.04	1.31
H2 (m)	9.4	4.4	6	6.2	3.4	5.1	15.9	20.8	2.8
Rho_2 (Ωm)	10905	14612	28607	14322	2040	2754	4798	5221	731
$\Sigma K/2$	1.05	1.15	1.11	1.04	1.02	1.45	1.34	1.02	1.28
H3 (m)	-	-	25.5	-	20.6	4.2	13.6	75.6	9.3
Rho_3 (Ωm)	540	810	6408	2100	282	1941	2397	565	2341
$\Sigma K/2$	1.25	1.02	1.03	1.01	1.03	1.98 / 8.1	3.87/1.73	1.17	1.31
H4 (m)	-	-	-	-	-	16.8	66.5	-	27.8
Rho_4 (Ωm)	-	-	1289	-	5340	3161	409	60665	352
$\Sigma K/2$	-	-	1.04	-	1.06	1.33	1.81	10	1.81
Rho_5 (Ωm)	-	-	-	-	-	1441	36486	-	42196
K	-	-	-	-	-	1.01	10	-	10
RMS (%)	5.6	5.6	3.87	5.6	10.6	3.4	4.5	3.5	3.6
Ke (%)	2	2	1	1.2	2	0.7	0.85	2	1.8

DD: decimal degrees; m asl: metres above sea level; AB/2: the maximum electrode aperture in half the space; H, thicknesses

Table 3. Summary of results of seismic refraction P waves.

Profile	Thickness (m)					Velocity m/s
	RS1	RS2	RS3	RS4	RS5	
Mostly sub-sonic	2.0-4.0	3.0-6.0	0.0-6.5	-	0.6-4.7	<500
G1-G2 (DS 3)	8.0	7.0-10.0	10.0	5.3-6.7	-	500-700
				-	-	700-900
G2 (DS 2)	>8.0	>10.0	-	-	3.6-6.0	1200-1500
Weathered granite			>10.0	-	>6.0	1500-1700
Granite	ND	ND	ND	>6.0	ND	>2000

ND, no detected; G1 and G2, Vertical Electrical Sounding resistivity units; DS 2 and DS 3, Depositional sequences

Figure 1_R1 (Color)
[Click here to download high resolution image](#)

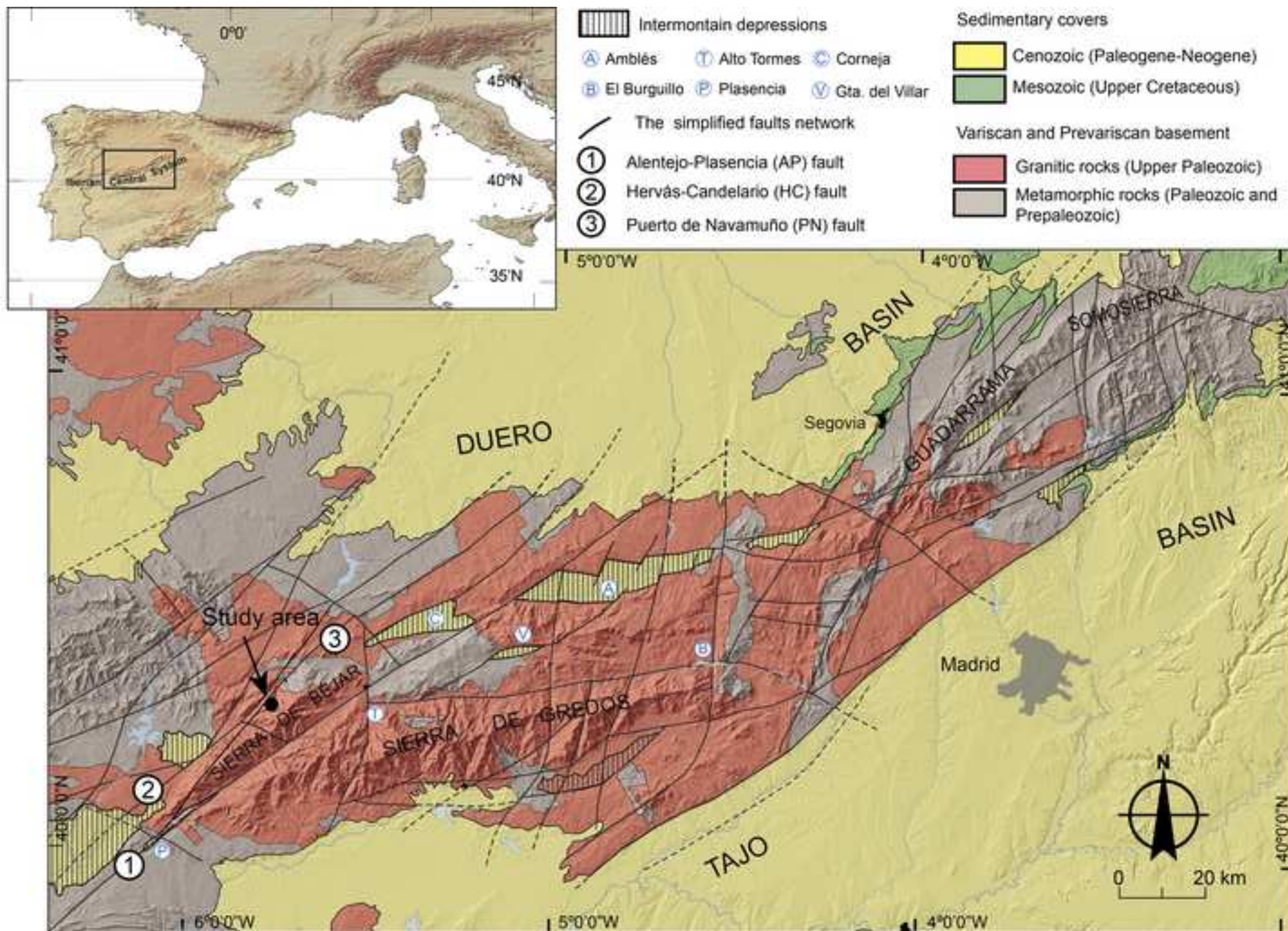


Figure 2_R1 (Color)
[Click here to download high resolution image](#)

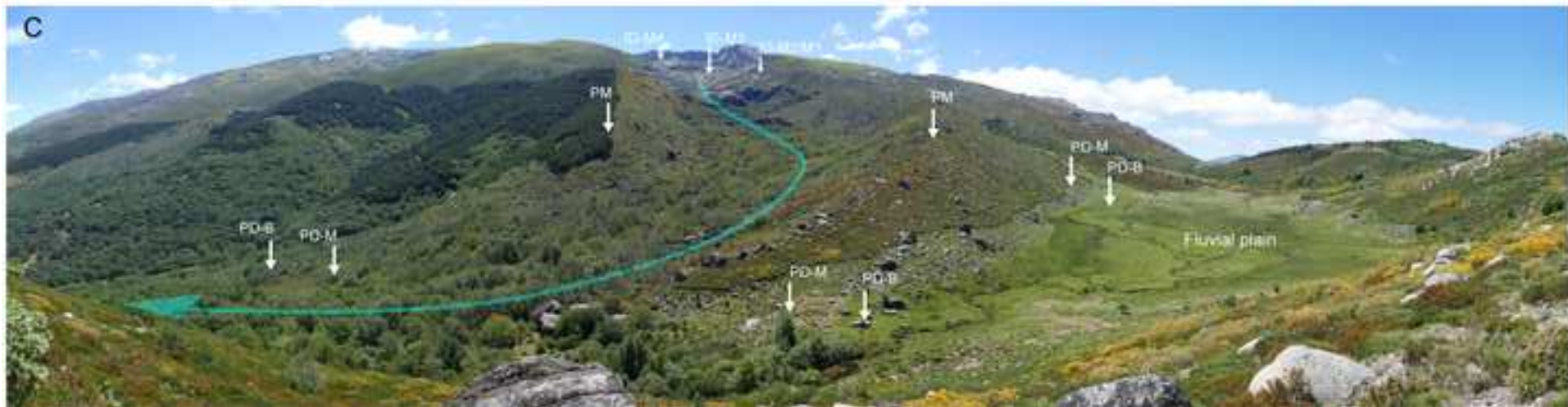
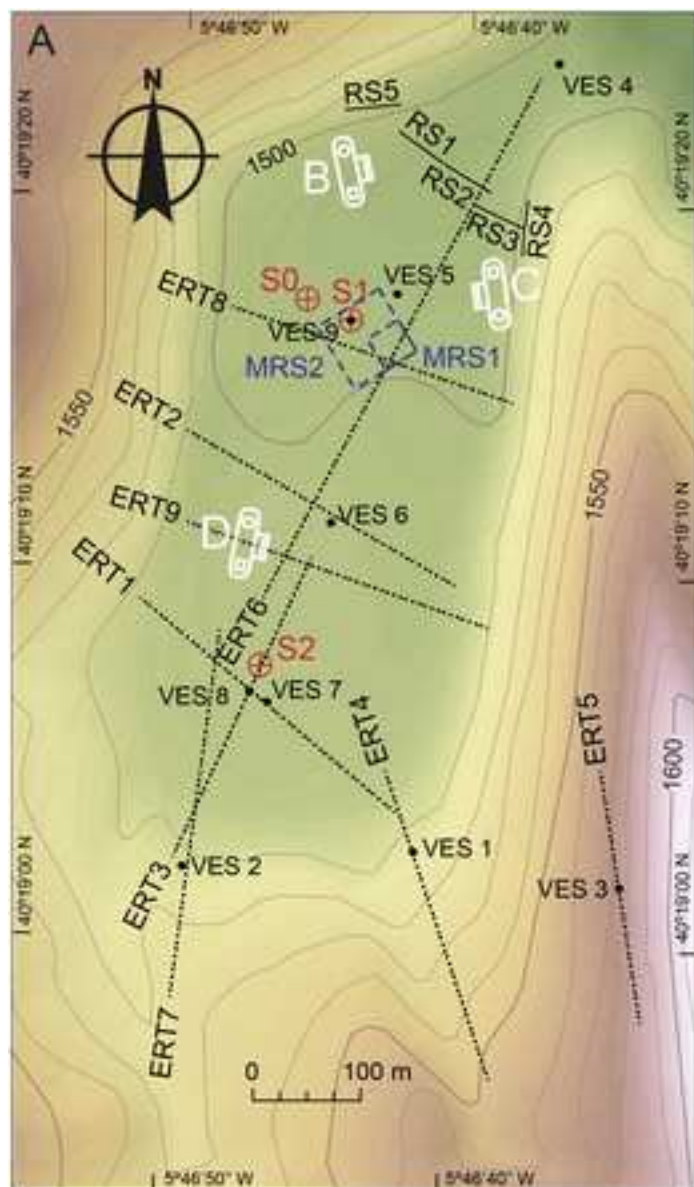


Figure 3_R1 (Color)
[Click here to download high resolution image](#)



- Vertical Electrical Soundings (VES 1 to 9)
- ⊕ Sounding (S0, S1, S2)
- Electrical Resistivity Tomography profiles (ERT 1 to ERT 9)
- Seismic profiles (RS 1 to RS 5)
- - - Magnetic Resonance Sounding (MRS 1 and MRS 2)

Figure 4_R1 (Color)
[Click here to download high resolution image](#)

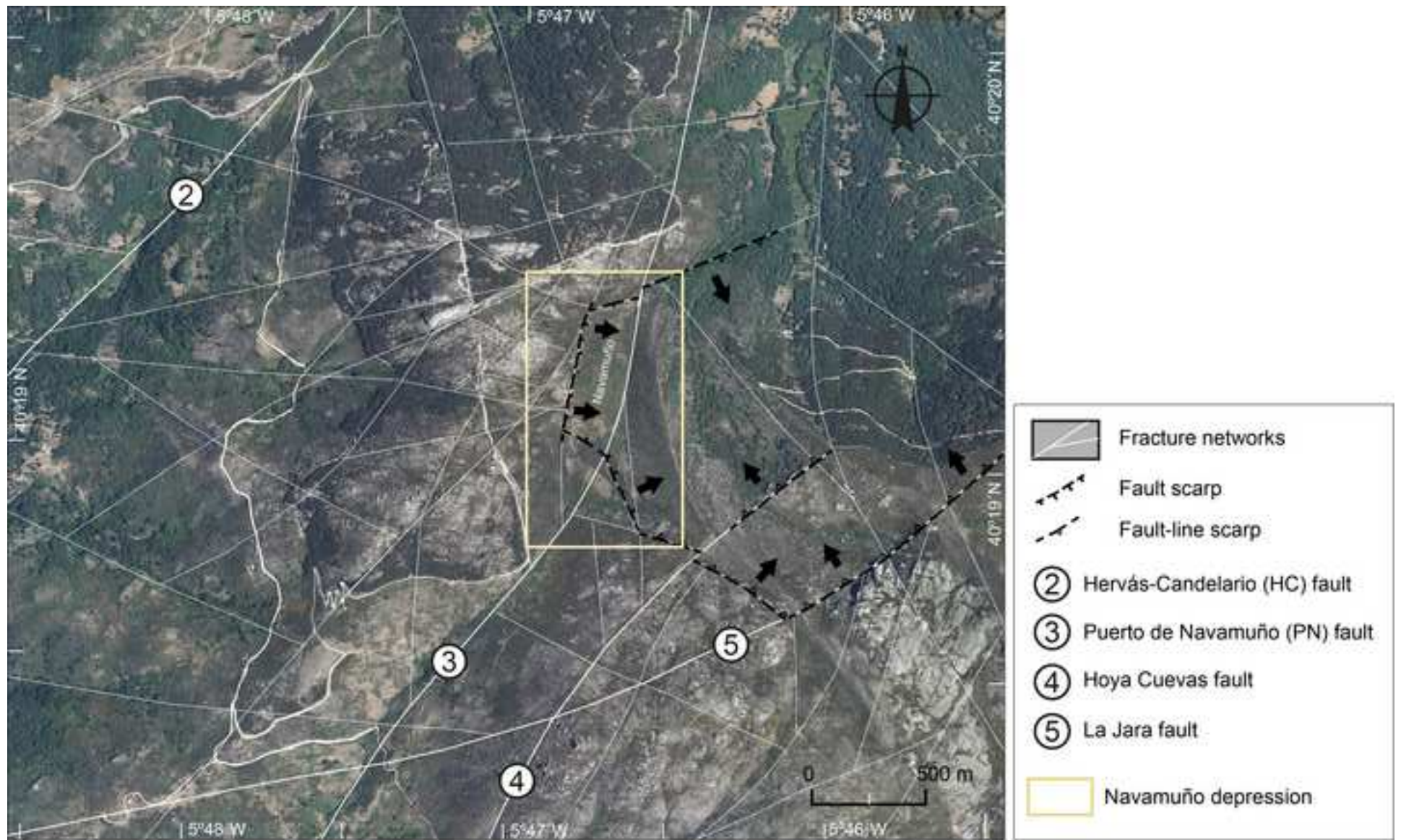


Figure 5_R1 (Color)
[Click here to download high resolution image](#)

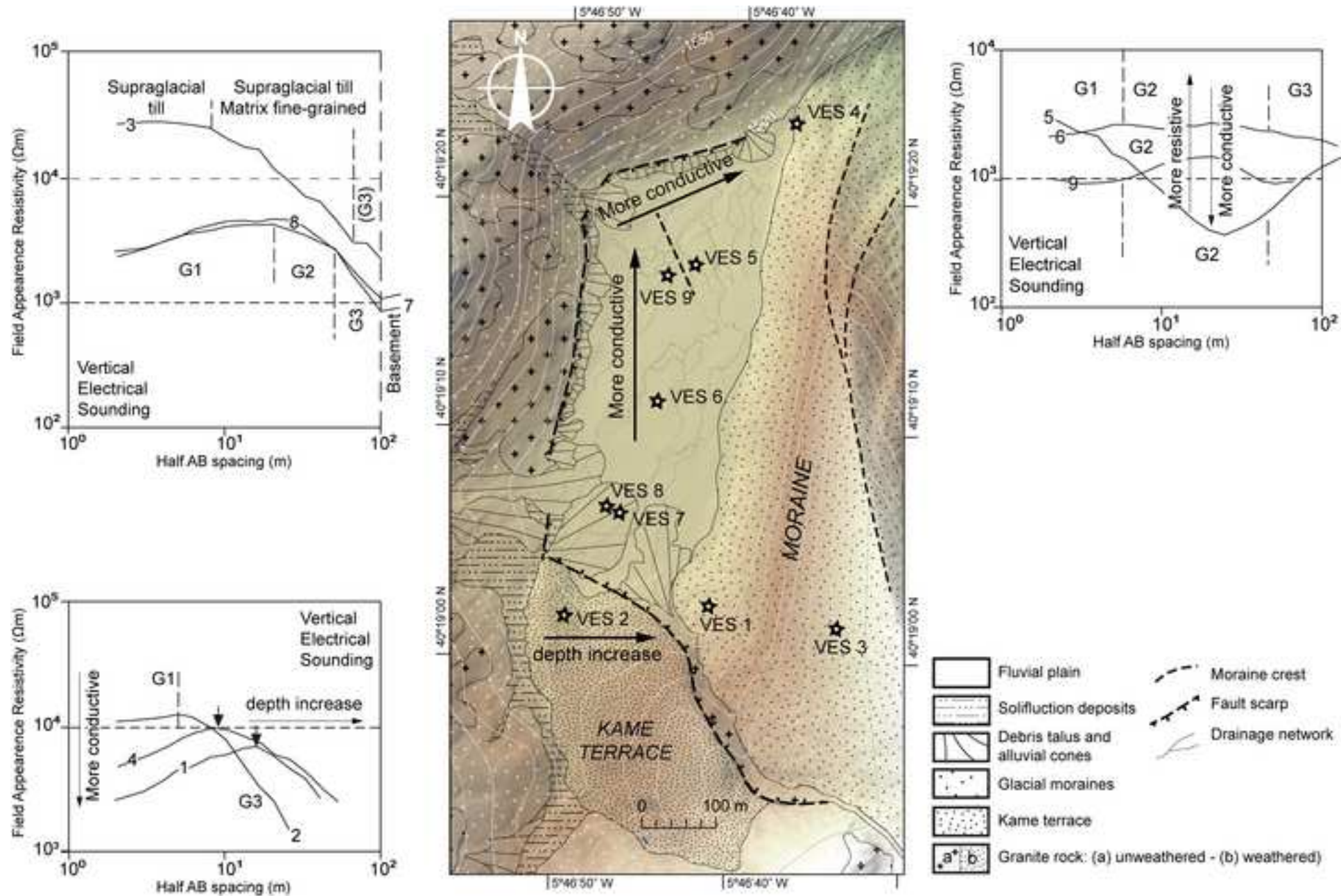


Figure 6
[Click here to download high resolution image](#)

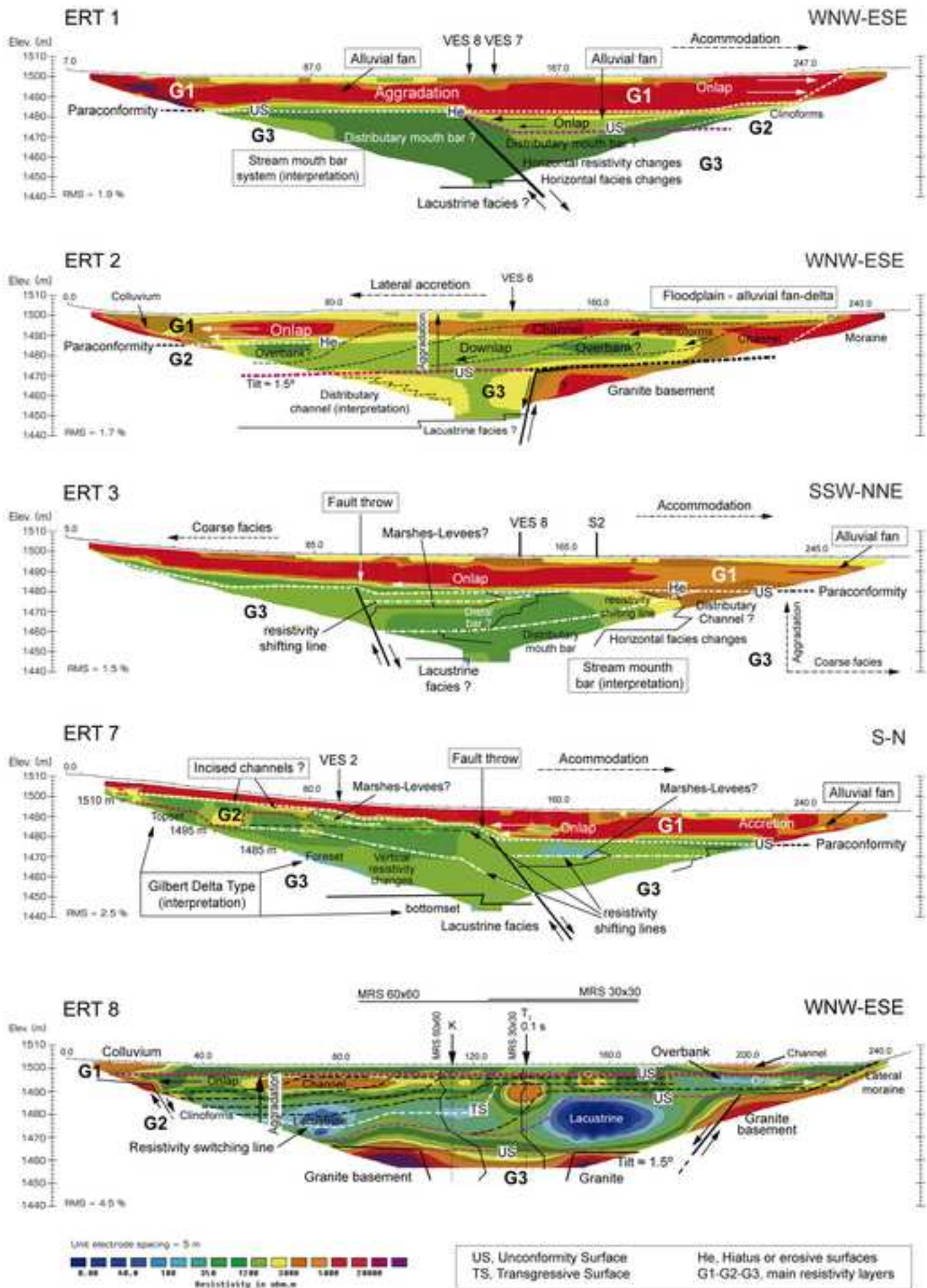


Figure 7
[Click here to download high resolution image](#)

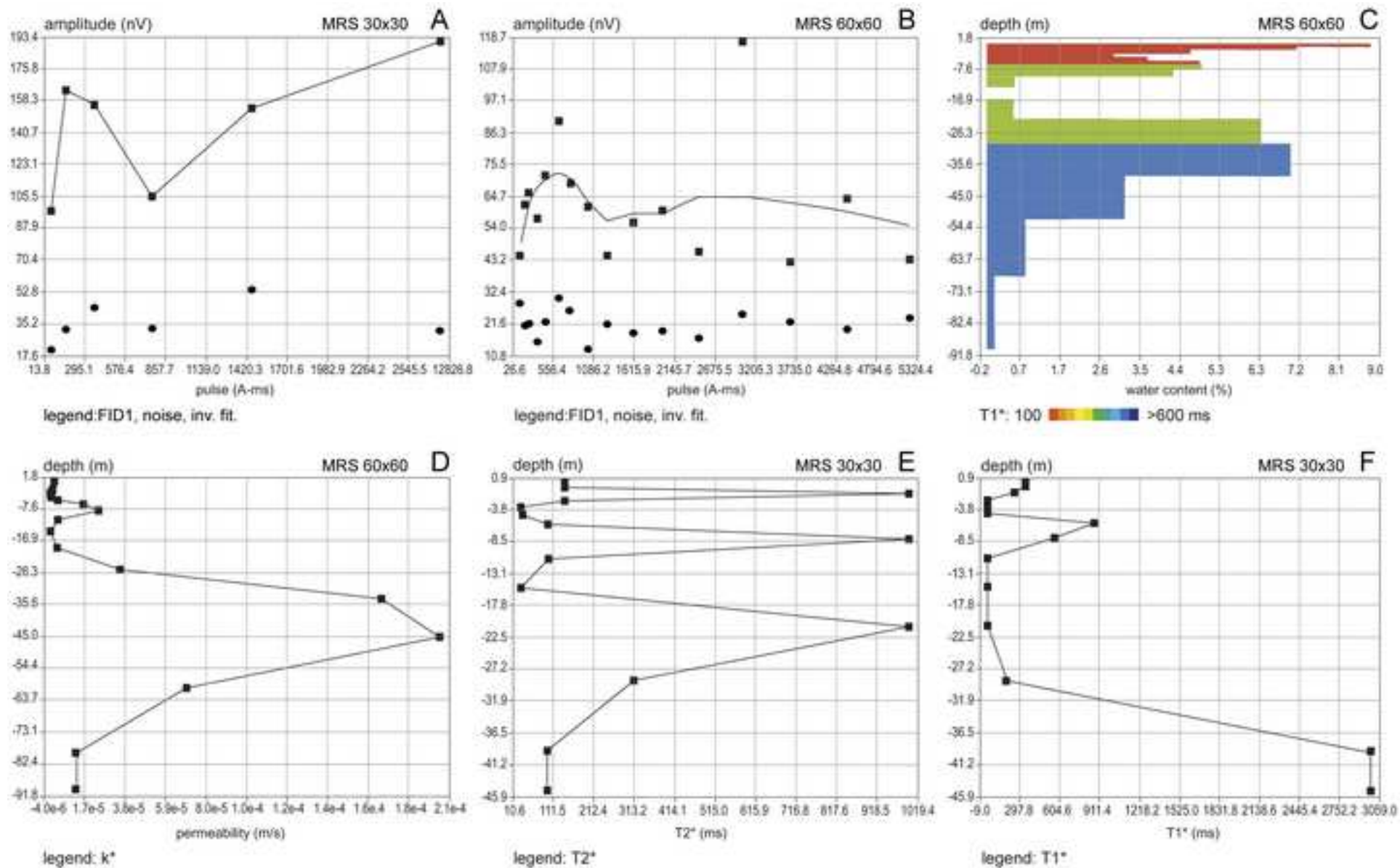


Figure 8_R1 (Color)
[Click here to download high resolution image](#)

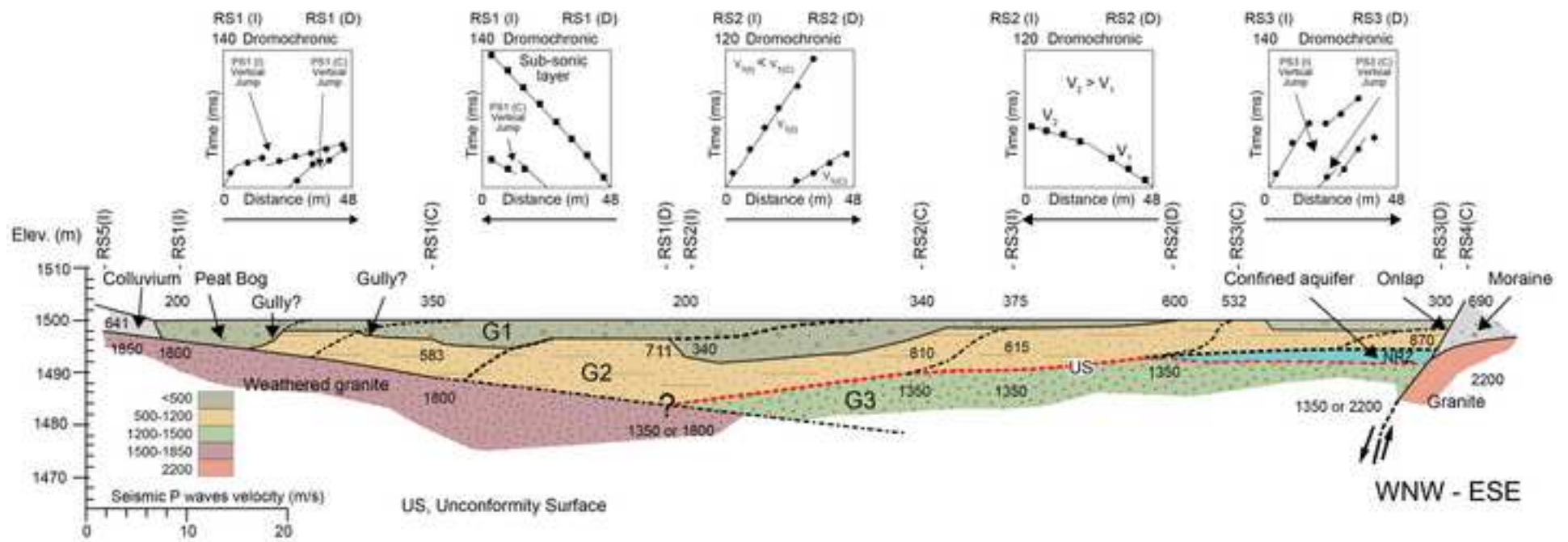
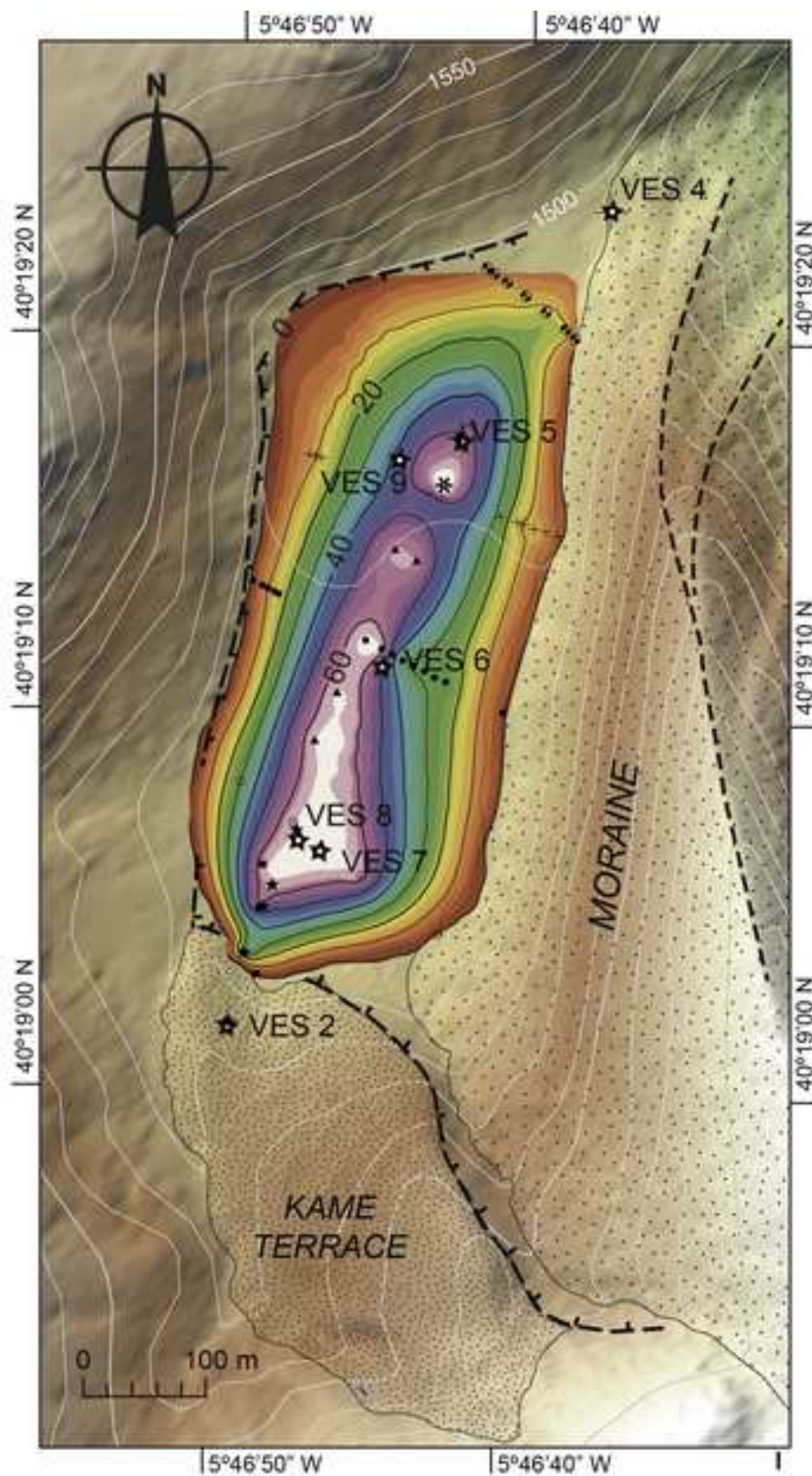


Figure 9_R1 (Color)

[Click here to download high resolution image](#)



--- Fault scarp and fault-line scarp
-.- Moraine crest



○ ETRS 1 ● ETRS 2 ★ ETRS 3 ▲ ETRS 6
■ ETRS 7 + ETRS 8 * MRS ⊙ RS

Figure 1_R1 (Greyscale)
[Click here to download high resolution image](#)

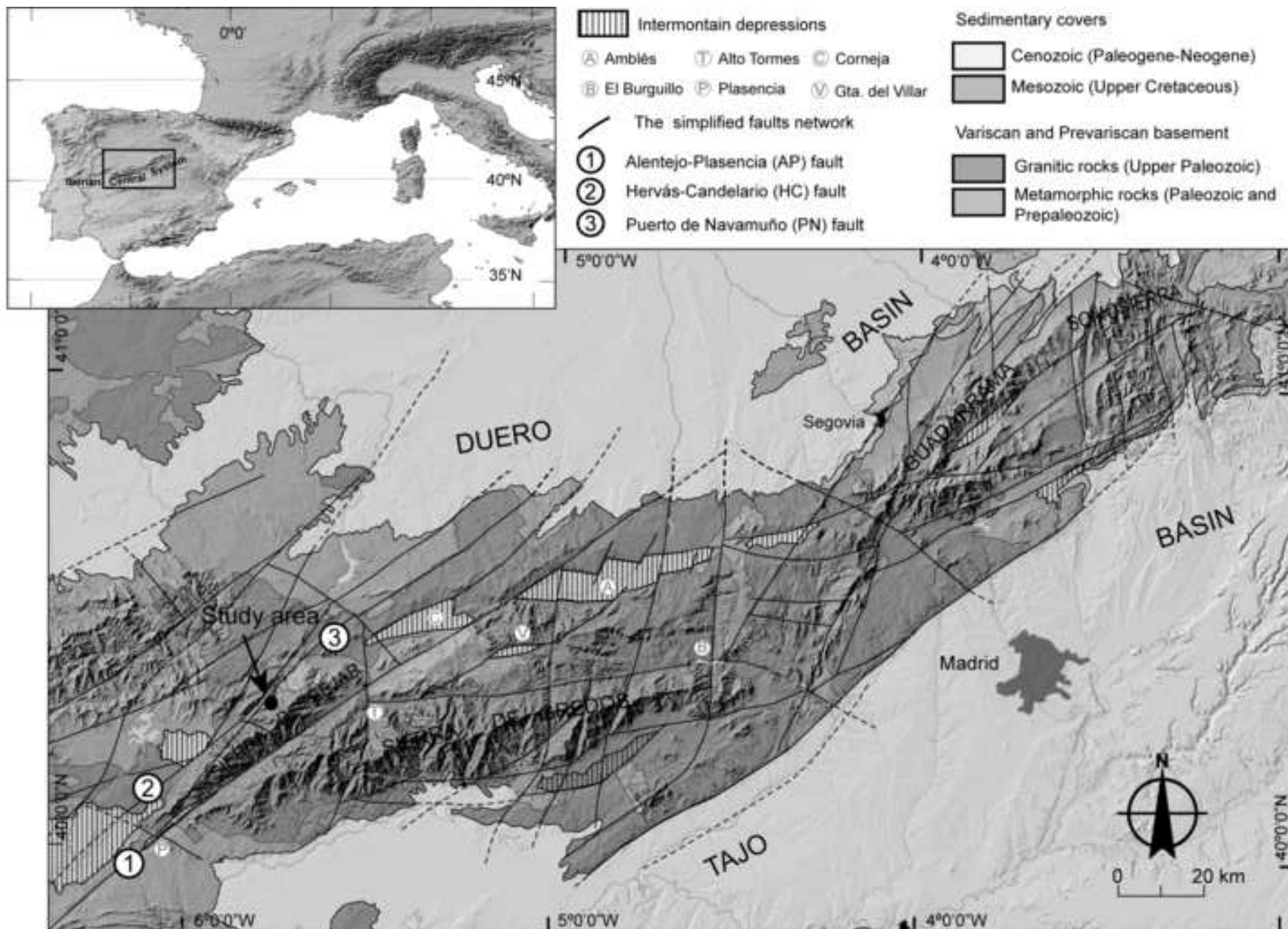


Figure 2_R1 (Greyscale)
[Click here to download high resolution image](#)

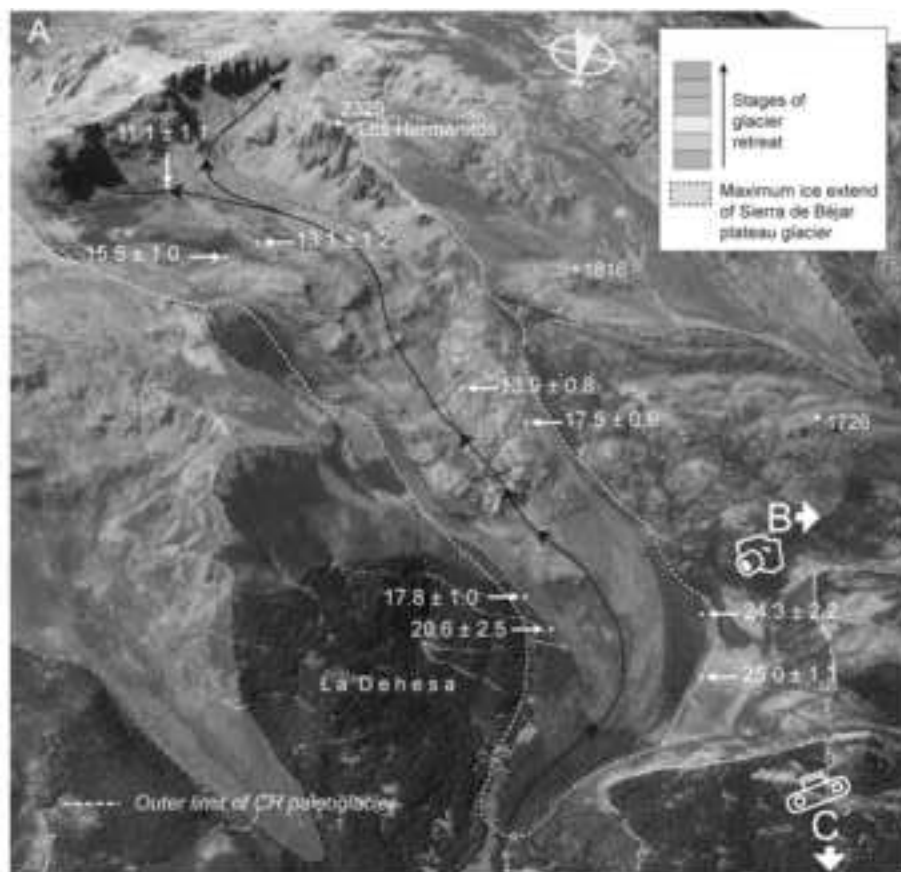
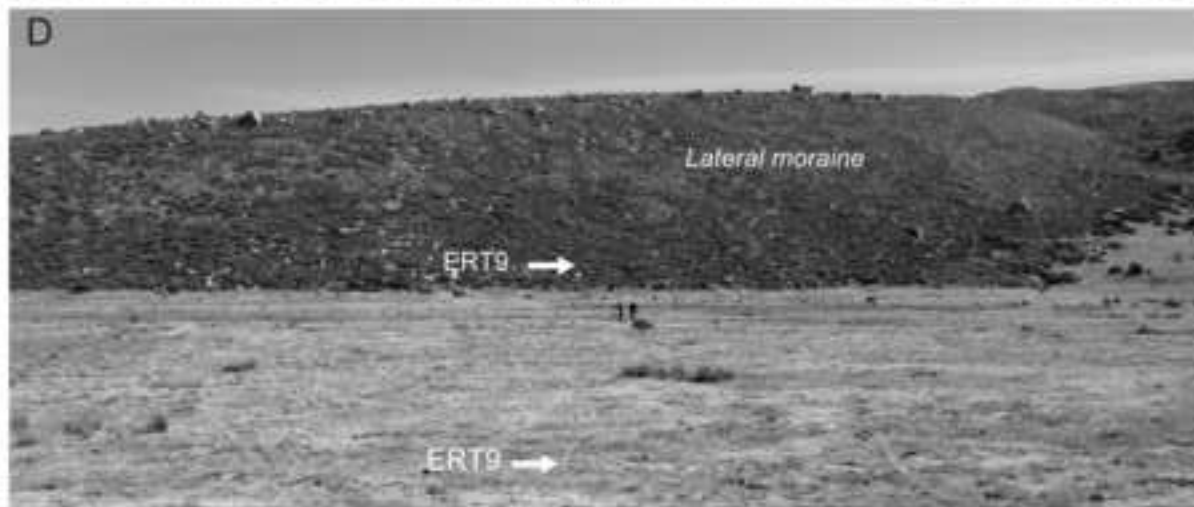
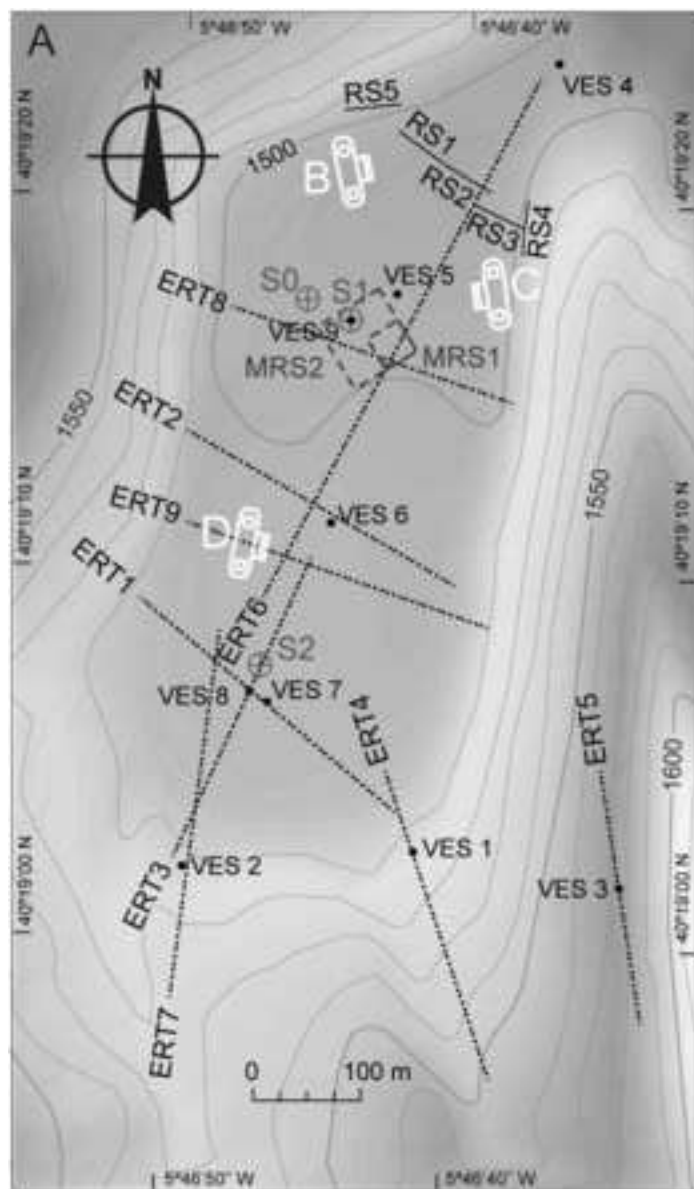


Figure 3_R1 (Greyscale)
[Click here to download high resolution image](#)



- Vertical Electrical Soundings (VES 1 to 9)
- ⊕ Sounding (S0, S1, S2)
- Electrical Resistivity Tomography profiles (ERT 1 to ERT 9)
- Seismic profiles (RS 1 to RS 5)
- - - Magnetic Resonance Sounding (MRS 1 and MRS 2)

Figure 4_R1 (Greyscale)
[Click here to download high resolution image](#)

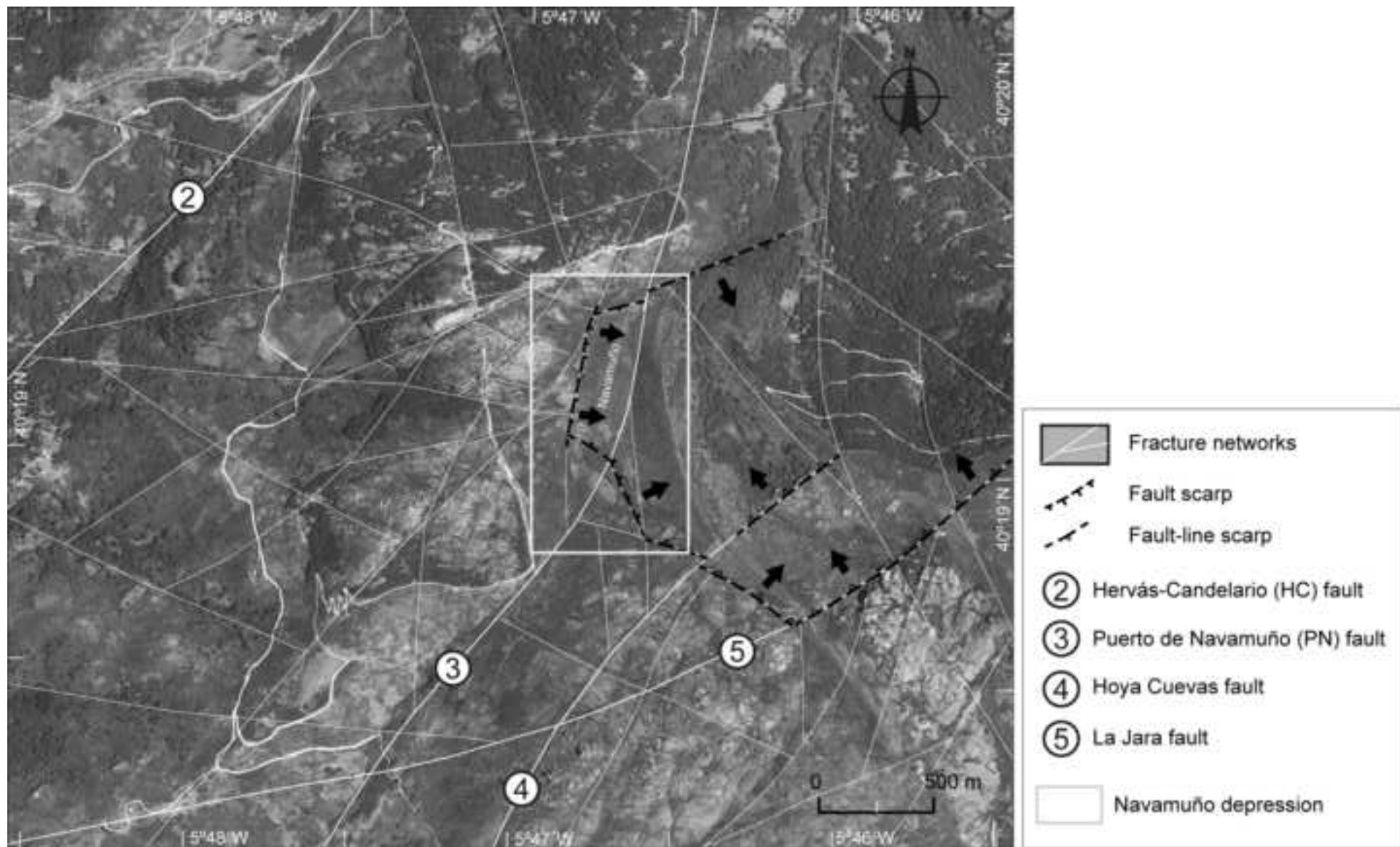


Figure 5_R1 (Greyscale)
[Click here to download high resolution image](#)

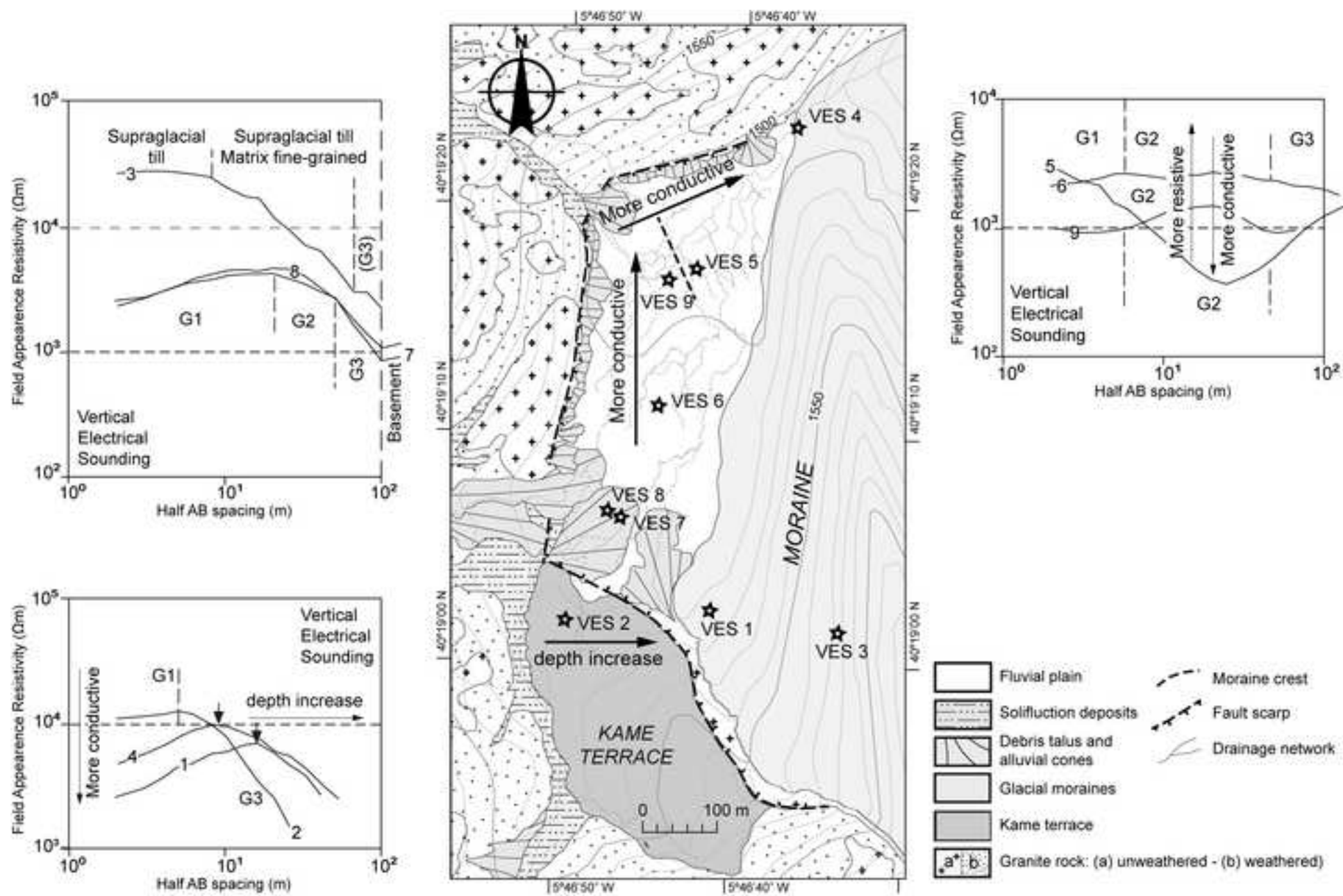


Figure 6 (Greyscale)
[Click here to download high resolution image](#)

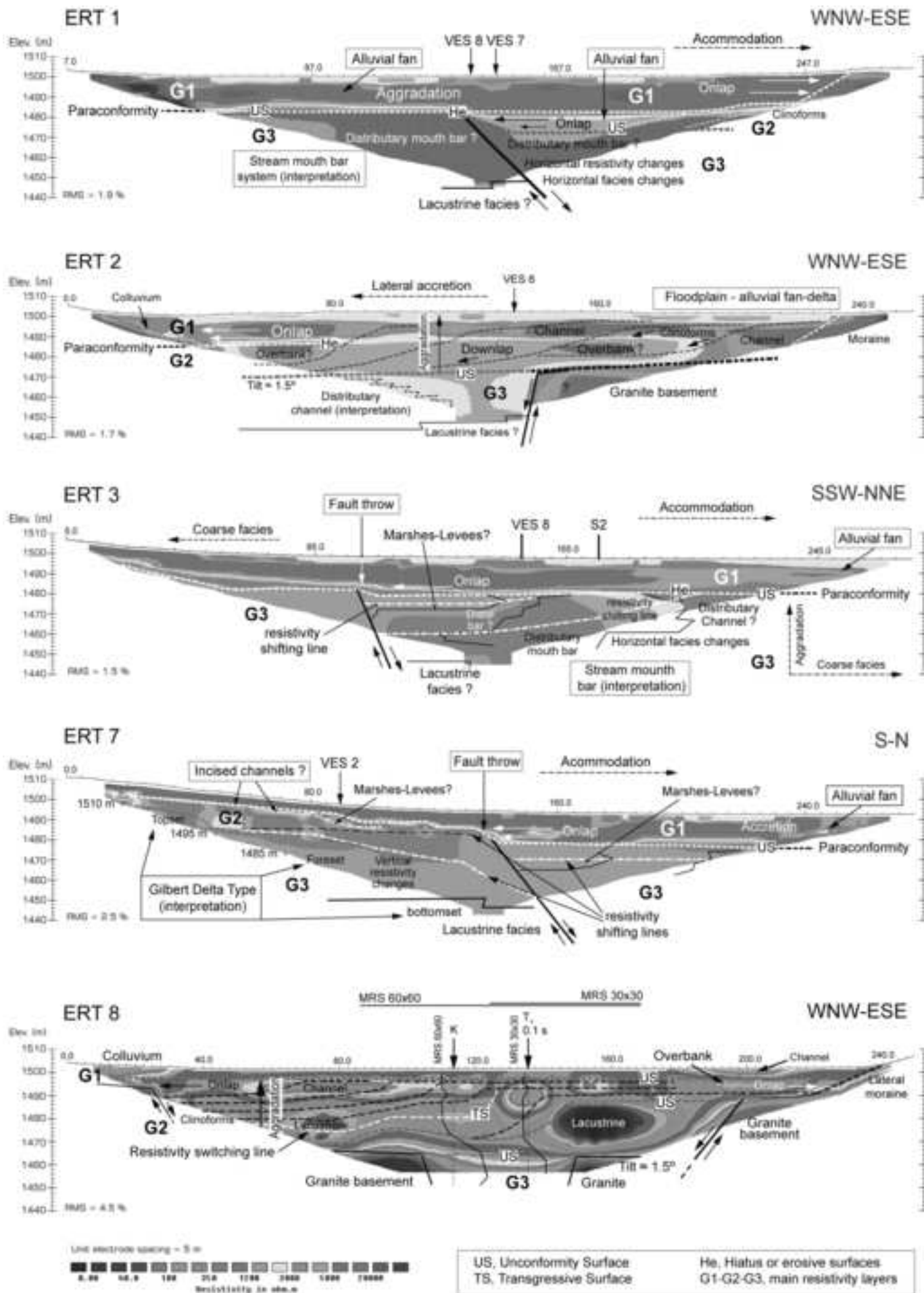


Figure 7 (Greyscale)
[Click here to download high resolution image](#)

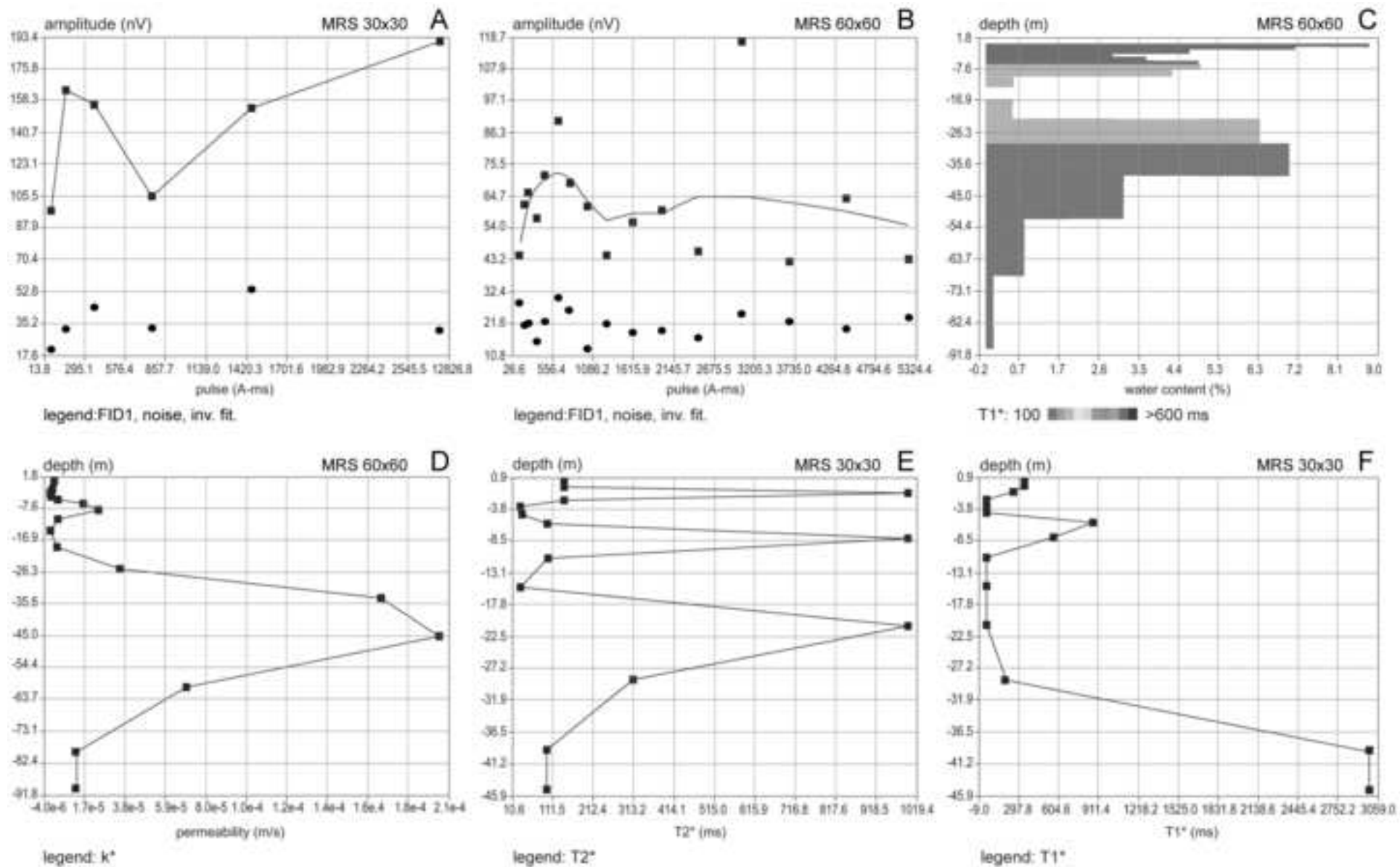


Figure 8_R1 (Greyscale)
[Click here to download high resolution image](#)

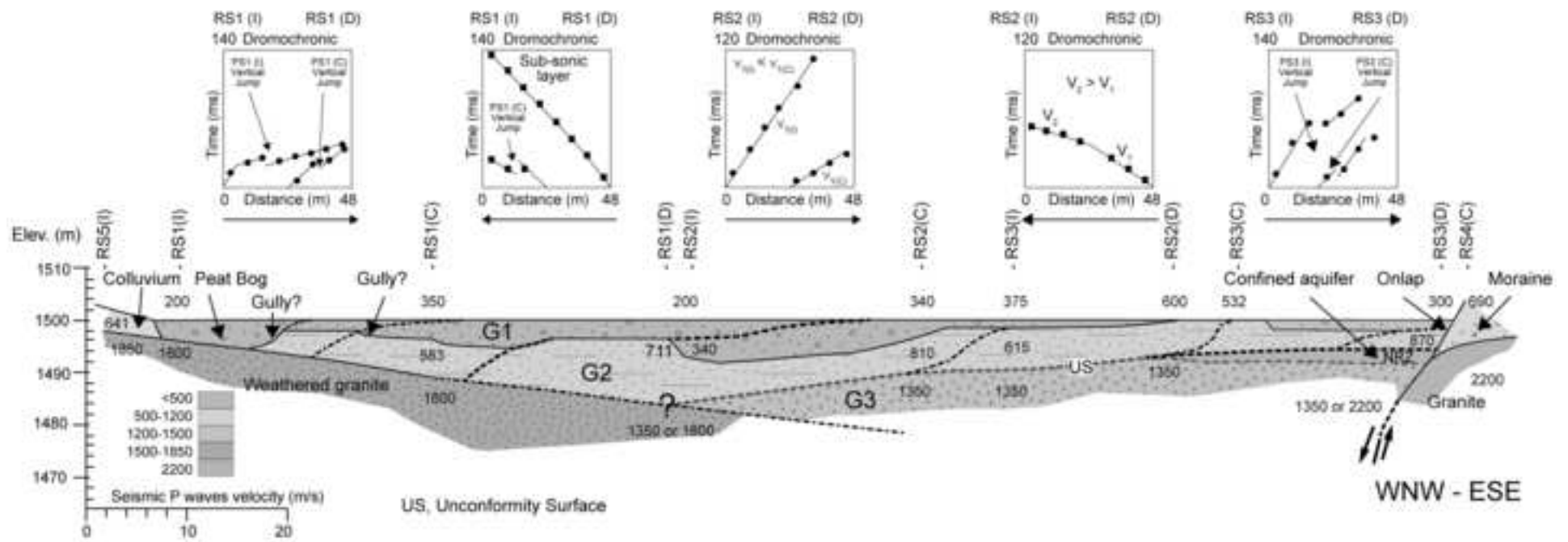
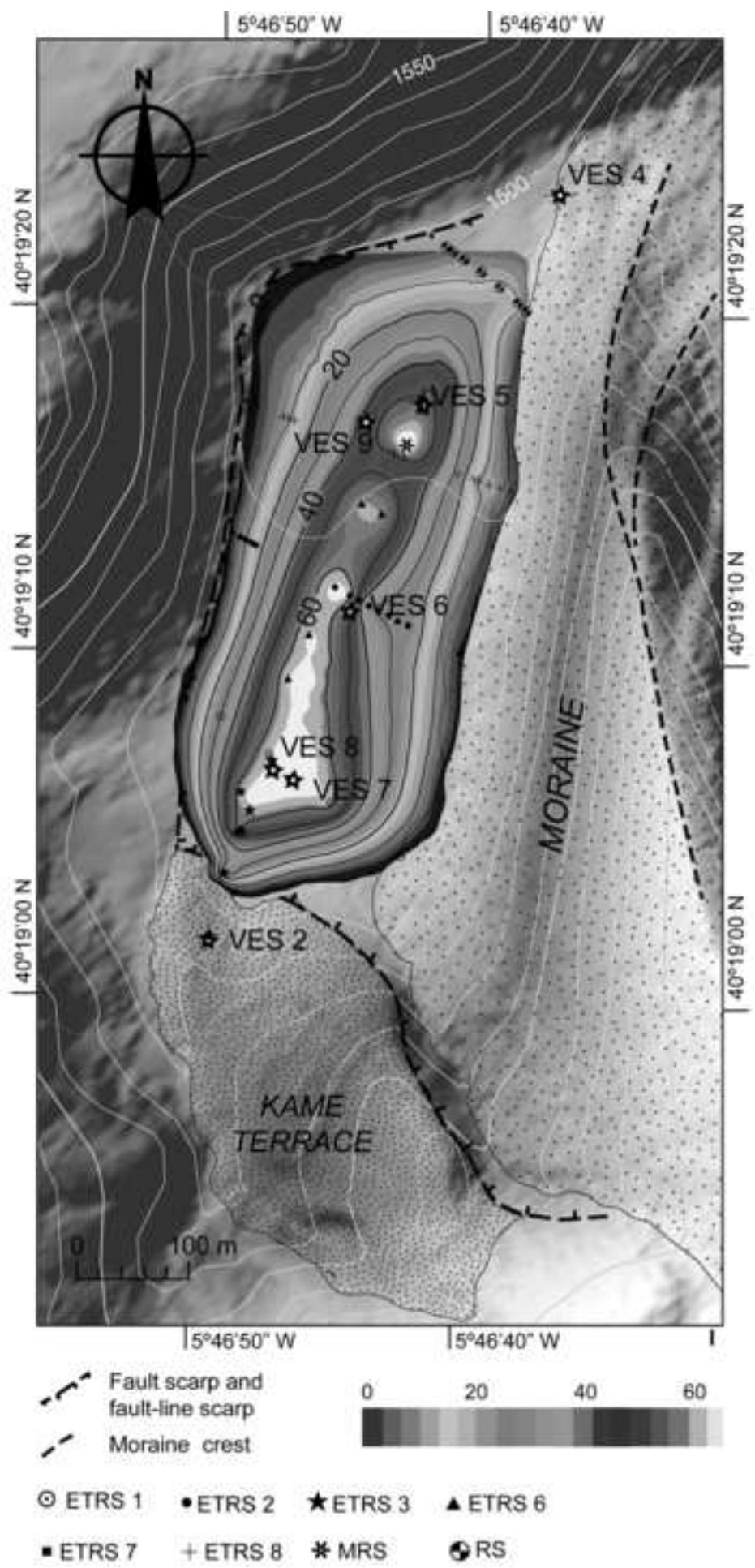


Figure 9_R1 (Greyscale)
[Click here to download high resolution image](#)



Supplementary material for online publication only

[Click here to download Supplementary material for online publication only: GEOMOR-6524R2_SupplementaryData.doc](#)